LIGHT SCATTERING IN COMPOUNDS WITH STRONG SPIN ORBIT COUPLING AND FOR SOLAR CELL APPLICATIONS

Von der Fakultät für Elektrotechnik, Informationstechnik, Physik
der Technischen Universität Carolo-Wilhelmina
zu Braunschweig
zur Erlangung des Grades eines
Doktors der Naturwissenschaften
(Dr.rer.nat.)
genehmigte
Dissertation

von Azat Sharafeev
aus Potsdam

1. Referent: Prof. Dr. Peter Lemmens
2. Referent: Prof. Dr. Meinhard Schilling
eingereicht am: 23.01.2017
Disputation am: 21.04.2017

Druckjahr: 2017

Vorveröffentlichungen der Dissertation

Teilergebnisse aus dieser Arbeit wurden mit Genehmigung der Fakultät für Elektrotechnik, Informationstechnik, Physik, vertreten durch den Betreuer der Arbeit, in folgenden Beiträgen vorab veröffentlicht:

- **A. Sharafeev**, R. Sankar, A. Glamazda, K.-Y. Choi, R. Bohle, P. Lemmens, F. Chou, *Doping effects on charge density instability in non-centrosymmetric* Pb_xTaSe_2, arXiv:1505.00748 (2015).

- **A. Sharafeev**, V. Gnezdilov, R. Sankar, F. Chou, P. Lemmens, *Optical phonon dynamics and electronic fluctuations in the Dirac semimetal* Cd_3As_2, arXiv:1701.04447 (2017).

- M. Abdelfatah, J. Ledig, A. El-Shaer, A. Wagner, **A. Sharafeev**, P. Lemmens, M. M. Mosaad, A. Waag, A. Bakin, *Fabrication and characterization of flexible solar cell from electrodeposited* Cu_2O *thin film on plastic substrate*, Solar Energy **122**, 1193-1198, (2015).

- M. Abdelfatah, J. Ledig, A. El-Shaer, A. Wagner, V. Marin-Borras, **A. Sharafeev**, P. Lemmens, M. M. Mosaad, A. Waag, A. Bakin, *Fabrication and characterization of low cost* $Cu_2O/ZnO:Al$ *solar cells for sustainable photovoltaics with earth abundant materials*, Solar Energy Materials and Solar Cells **145**, 454-461, (2016).

- M. Abdelfatah, J. Ledig, A. El-Shaer, **A. Sharafeev**, P. Lemmens, M. M. Mosaad, A. Waag, A. Bakin, *Effect of Potentiostatic and Galvanostatic Electrodeposition Modes on the Basic Parameters of Solar Cells Based on* Cu_2O *Thin Films*, ECS Journal of Solid State Science and Technology **5**(6), Q183-Q187 (2016).

Abstract

Strong spin-orbit coupling, symmetry and topology are the most frequently used terms which are present in the recent condensed matter research. Indeed, such ingredients make it possible to open the door into novel physics and to generate new classes of materials, such as topological insulators, Rashba materials, Weyl and Dirac semimetals. One of the examples of Dirac semimetals, Cd_3As_2, is discussed in this thesis. It has a distinctive for this type of materials electronic structure. Similar to graphene, it possesses a Dirac cone-shaped band diagram due to massless fermions, and also unusual transport properties, which would be valuable for future applications. Therefore, investigation of the crystal structure of Cd_3As_2 is essential because of its correlation with the electronic structure.

$PbTaSe_2$ is another prominent example of the family of topological materials. It is, in fact, a noncentrosymmetric superconductor and can be obtained by Pb intercalation into $TaSe_2$, which, in turn, undergoes a charge density wave phase at low temperatures. Thus, besides non-trivial electronic topologies, one can study here another fundamental question as competition between superconductivity and charge density waves. This compound is also considered to be a candidate for topological superconductors and, presumably, it might hold Majorana bound states in its vortices.

Last but not least, this thesis also covers applied aspects, such as investigation of contemporary solar energy devices using Raman scattering. As a matter of fact, current photovoltaic industry at-

tempts to achieve solar cell devices with the best balance between price, efficiency and environment-friendliness of materials. One of the most promising candidates is cuprous oxide - Cu_2O. It is non-poisonous, earth-abundant, chemically stable and has theoretical power conversion efficiency of ~ 20 %. Raman scattering spectroscopy allows to study the crystal structure of semiconductors and, in particular, copper-based solar cells to detect crystal imperfections and define their composition. It is a valuable tool to investigate solar cell devices since Raman spectroscopy is a fast and non-destructive technique.

Überblick

Starke Spin-Bahn-Kopplung, Symmetrie und Topologie sind die am häufigsten verwendeten Begriffe in der aktuellen Forschung der Kondensierten Materie. Solche Aspekte machen es möglich, eine Tür in neuartige Physik zu öffnen und neue Materialklassen wie topologische Isolatoren, Rashba-Materialien, Weyl- und Dirac-Halbmetalle herzustellen. Cd_3As_2 ist eines dieser Beispiele von Dirac-Halbmetallen. Es hat eine für diese Art von Materialien besondere elektronische Struktur. Ähnlich wie Graphen besitzt es zwei Dirac-Kegel aufgrund masseloser Fermionen und auch ungewöhnliche Transporteigenschaften, die für zukünftige Anwendungen wertvoll wären. Daher ist die Untersuchung der Kristallstruktur von Cd_3As_2 aufgrund ihrer Beziehung mit der elektronischen Struktur wichtig.

$PbTaSe_2$ ist ein weiteres prominentes Beispiel für eine Familie topologischer Materialien. Diese Verbindung ist in der Tat ein nicht-zentrosymmetrischer Supraleiter und kann durch Pb-Interkalation in $TaSe_2$ erzeugt werden, das seinerseits eine Ladungsdichtewellenphase bei niedrigen Temperaturen besitzt. Neben nicht-trivialen elektronischen Topologien kann man hier die grundsätzliche Frage zur Konkurrenz zwischen Ladungsdichtewelle und Supraleitfähigkeit untersuchen. Diese Verbindung wird auch als ein Kandidat für topologische Supraleiter angesehen, und vermutlich könnte es gebundene Majorana Zustände in ihren FluÃ§linien geben.

Schliesslich geht es bei dieser Arbeit auch um angewandte Aspekte wie die Untersuchung moderner Solarzellen mit Raman-

Streuung. Tatsächlich versucht die derzeitige Photovoltaik-Industrie, Solarzellenmodule mit dem besten Mix aus Preis, Effizienz und Umweltfreundlichkeit von Materialien zu erreichen. Einer der vielversprechendsten Kandidaten ist Kupferoxid - Cu_2O. Es ist nicht giftig, erdreich, chemisch stabil und hat eine maximale theoretische Leistungsumwandlungseffizienz von ~ 20 %. Die Raman-Spektroskopie erlaubt, die Untersuchung der Kristallstruktur von Halbleitern und insbesondere von kupferbasierten Solarzellen, um Unvollkommenheiten und Fremdphasen zu detektieren und deren Zusammensetzung zu definieren. Es ist ein wertvolles Hilfsmittel, um Solarzellen zu untersuchen, da die Raman-Spektroskopie eine schnelle und zerstörungsfreie Technik ist.

Acknowledgements

This thesis would not be possible without help and support of many people. Every single person listed here has contributed into this work and for that I am very grateful.

First of all, I would like to thank *Prof. Peter Lemmens*, for his continuous support, helpful advices, excellent guidance and patience through the whole PhD life. It was an exciting adventure, thanks a lot for such an opportunity to work together with you in the Institute for Condensed Matter.

I express my gratitude to our collaborators *Dr. Vladimir Gnezdilov* and *Prof. Yurii Pashkevich*, for the fruitful discussions about physics, for the guidance into Raman Sprectroscopy and for being supportive during my PhD time. I thank *Prof. Kwang-Yong Choi* for his inspiring discussions about every aspect of the research and life. I am grateful to *Dr. Raman Sankar* and *Prof. Fang-Cheng Chou* for their complicated but fascinating samples, *Dr. Mahmoud Saad* and *Prof. Andrey Bakin* for their brown, efficient and earth-abundant solar cell devices. I express my gratitude to *Prof. Samir Kumar Pal*, because during his visits we always had nice talks and good mood.

I would like to thank my colleagues: *Dr. Alexander Glamazda* for the time being here and helping out with the challenges I would not be able to solve on my own, for interesting evening small talks. *Dr. Hongdan Yan* for helping to survive the first days at the work. *Bo Liu* for his friendship, being always positive and his numerous advices. *Silvia Müllner* for being so friendly not only to me but to all of us, for helping with German language, for sharing her experience and jokes like "Do you know stevia?". *Savutjan Sidik* for

his positiveness at any time.

I am very grateful to *Katharina Schnettler*, for making our life very easy, especially the first days of my PhD, for caring of every detail in bureaucratic things, to *Axel Paschke* for his job as helping us out with the paperwork and his tips how to spend good time in Harz, to *Bodo Lobbenmeier, Lutz Nagatz, Thilo Lampe, Lisa Hoffmann, Andreas Dudler, Arno Ellermann, Günter Wesemann* for their help with the lectures and technical support of our laboratory, to *Manuela Bosse* and *Gudrun Zeising* for maintaining the workflow of the institute. Also I thank *Dr. Dirk Menzel, Prof. Jochen Litterst, Prof. Stefan Süllow* for their comments during seminars in our institute. I am glad to acknowledge *Elaheh Sadrollahi* for sharing our experiences of the PhD life in Braunschweig.

I am grateful to my friends for their support, encouragement and friendship: *Sergey* and *Natalya*, *Andreas* and *Nastya*, *Darya* und *Tobias*. I can continue the list of acknowledgements further, but I am afraid there would not be enough space, because a lot of people were involved into this thesis and I thank them all.

This work was supported by B-IGSM of the TU Braunschweig, DFG and GIF. I would like to thank organisers of International Graduate School of Metrology, especially *Prof. Meinhard Schilling* and *Judith Krakowski*, for all events, workshops, field trips and lectures that you have organised, we loved them very much!

In the end, I would love to thank *my parents*, for their tremendous support throughout my whole life, I am very proud to have such family. I want to express my deepest gratitude to *my parents-in-law* and my beloved wife *Ellina*, thank you for being with me all the time, for your inspiration and infinite support since the day we met each other.

Contents

Abstract **3**

Überblick **5**

1 Introduction **15**

2 Basics of Raman Scattering **18**
- 2.1 Theoretical Considerations 19
- 2.2 Experimental Setup 27

3 Light Scattering in Compounds with Strong SOC **31**
- 3.1 The 2D Layered Pb_xTaSe_2 Superconductor 31
  - 3.1.1 Crystal Structure 33
  - 3.1.2 Electronic and Magnetic Properties 33
  - 3.1.3 Experimental Details 46
  - 3.1.4 Properties of the Phonon Spectrum 48
  - 3.1.5 Comparison with $TaSe_2$ 49
  - 3.1.6 Temperature-induced Effects in Pb_xTaSe_2 . . 52
  - 3.1.7 Resonance Effects 55
  - 3.1.8 Discussion 60
  - 3.1.9 Conclusion 63
- 3.2 The 3D Dirac Semimetal Cd_3As_2 65
  - 3.2.1 Crystal Structure 66
  - 3.2.2 Electronic and Magnetic Properties 67
  - 3.2.3 Experimental Details 71
  - 3.2.4 Properties of the Phonon Spectrum 74

3.2.5 Resonance Effects 76
3.2.6 Temperature-induced Effects 79
3.2.7 Discussion 79
3.2.8 Conclusion 84

4 Light Scattering in Solar Energy Materials 85
4.1 Cu_2O Solar Cells: Fabrication and Characterisation 85
4.1.1 Experimental Details 86
4.1.2 Properties of the Phonon Spectrum 87
4.1.3 Properties of the Solar Cell Device 90
4.1.4 Conclusion 100
4.2 Flexible Cu_2O Thin Film Solar Cells on Plastic Substrate 102
4.2.1 Properties of the Solar Cell Device 103
4.2.2 Conclusion 108

5 Summary 109

List of Figures

2.1 Sketch of a light scattering process 20
2.2 Sketch of the first-order phonon scattering process . 24
2.3 Basic scheme of the Raman scattering setup 27

3.1 Sketches of the crystal structure of $TaSe_2$ and $PbTaSe_2$ 34
3.2 Temperature dependence of $PbTaSe_2$ 36
3.3 Calculated band structures of $PbTaSe_2$ with and without SOC 37
3.4 Bulk band structure of $PbTaSe_2$ 39
3.5 Electronic structure of $PbTaSe_2$ zoomed in at H and K with and without SOC 40
3.6 ARPES spectra of $PbTaSe_2$ and DFT Fermi surface contour of (001) 42
3.7 Fermi surface contour of $PbTaSe_2$ and $TaSe_2$ and ARPES spectra taken along $\overline{M}$-$\overline{K}$-$\overline{M}$ for $PbTaSe_2$ and $TaSe_2$ 43
3.8 DFT project bulk bands and surface bands of Pb- and Se-terminated (001) surfaces along $\overline{\Gamma}$-$\overline{K}$-$\overline{M}$ and $\overline{K}$-$\overline{X}$ 45
3.9 Microscope pictures of uncleaved $PbTaSe_2$ and $TaSe_2$ 47
3.10 Polarized Raman spectra (xx) of Pb_xTaSe_2 (x= 0, 0.25, 0.33, 0.5, 0.75, and 1) and the analysis of frequency, FWHM and intensity 50
3.11 Comparison of phonon frequency vs. the number of layers in exfoliated $TaSe_2$ and phonon frequency vs. Pb concentration in Pb_xTaSe_2 51

3.12 Polarized Raman spectra of $TaSe_2$, $Pb_{1/3}TaSe_2$ and $PbTaSe_2$ with different temperatures 53
3.13 Temperature dependence of the frequency, the linewidth and intensity of $TaSe_2$ phonons 54
3.14 Temperature dependence of the frequency, the linewidth and intensity of $PbTaSe_2$ for E′ (Pb-Pb) mode and E′ mode 56
3.15 Temperature dependence of the frequency, the linewidth and intensity of $PbTaSe_2$ for A′ mode and the background signal 57
3.16 Raman spectra of $PbTaSe_2$ with different incident laser excitations 58
3.17 Polarization dependence of Raman spectra of $PbTaSe_2$ in (xx) and (xy) polarizations 59
3.18 Evolution of the crystal structure of Cd_3As_2 with lowering the temperature 68
3.19 The 3D BZ and the projected (001) surface of Cd_3As_2 69
3.20 Experimental data of band dispersion from ARPES measurements with photons polarized along G-M direction 70
3.21 The temperature dependence of longitudinal resistivity of Cd_3As_2. The Hall resistance at different temperatures. The magnetic field dependence of the longitudinal resistivity at different temperatures 72
3.22 Optical conductivity of Cd_3As_2 at various temperatures 73
3.23 Unpolarized Raman spectrum of Cd_3As_2 at room temperature 76
3.24 Low temperature Raman spectra of Cd_3As_2 at T = 9.5 K 77
3.25 Raman spectra of Cd_3As_2 with different incident laser excitations 78
3.26 Raman spectra of Cd_3As_2 with different temperatures in (xx) polarization and at λ= 647 nm 80

3.27 Temperature development of the phonon frequencies and linewidths for 46.5 cm^{-1} mode and 48.5 cm^{-1} mode 81
3.28 Temperature development of the phonon frequencies and linewidths for 67 cm^{-1} mode and 73 cm^{-1} mode 82

4.1 Polarized Raman spectra (xx) of Cu_2O thin films before AZO layer sputtering 88
4.2 Polarized Raman spectra (xx) of AZO/Cu_2O solar cells 89
4.3 SE image (side view) of AZO/Cu_2O solar cell and its schematic diagram 90
4.4 AZO/Cu_2O solar cell current-voltage characteristics 92
4.5 Open circuit voltage (V_{oc}) and short circuit current density (J_{sc}) of AZO/Cu_2O solar cells 93
4.6 Fill factor (FF) and efficiency (η) of AZO/Cu_2O solar cells 95
4.7 External quantum efficiency (EQE) of the AZO/Cu_2O solar cell 97
4.8 Capacitance-voltage characteristics of the AZO/Cu_2O solar cell 99
4.9 Polarized Raman spectra (xx) of AZO/ZnO/Cu_2O solar cell on a plastic substrate 103
4.10 Photo image of the solar cell, SEM top and side view, schematic view of AZO/ZnO/Cu_2O solar cell on a plastic substrate 104
4.11 The schematic energy band diagram of AZO/ZnO/Cu_2O solar cell 105
4.12 Capacitance-frequency characteristics of AZO/ZnO/Cu_2O solar cell 106
4.13 Capacitance-voltage characteristics of the AZO/ZnO/Cu_2O solar cell 107

List of Tables

3.1 Structural parameters and Raman tensors of $TaSe_2$ and $PbTaSe_2$ 33
3.2 Table of the phonon modes of Cd_3As_2. 75

Chapter 1

Introduction

Systems with strong spin-orbit coupling play an important role in recent solid state physics research. The starting point was the discovery of topological insulators, which are insulators in the bulk but have special states on the surface with Dirac-like linear energy dispersion.

Plenty of new materials are continuously discovered and prepared where spin-orbit coupling leads to novel properties, such as topological insulators (TI), Rashba materials, Dirac and Weyl semimetals. In these materials, spin-orbit coupling leads to a reversal of electric states with respect to crystalline electric fields. Symmetry properties of these states lead to transport anomalies, e.g. a reduced backscattering. In addition, the surface band diagram has a shape of the so-called Dirac cone, where the massless particles are present instead of massive ones, which is similar to graphene.

In contrast to 2D TIs, also the three-dimensional topological Dirac semimetals (TDS) have been recently discovered and they may be considered as a 3D analogue of the graphene. Moreover, they are similar to TIs with respect to topological non-triviality of their electronic states. Dirac semimetals could be possibly driven into other phases, such as Weyl semimetal, by changing the crystal structure, e.g. breaking the inversion symmetry. A Weyl semimetal has topologically protected surface states with Fermi arcs on it. Therefore, it is crucial to determine the "right" structure of TDS. Cd_3As_2 is one of the examples of TDS which was in particular studied in this thesis. Such compounds have beneficial properties for the applications because of its high charge carrier mobility and stability at ambient conditions. With Raman spectroscopy one can clear up such issues as the presence or absence of inversion symmetry in the crystal structure and search for excitations related to topological effects and strong spin-orbit coupling.

Another example of the family of topological materials is $PbTaSe_2$. In fact, it is a superconductor with T_c = 3.8 K, which has an exotic band structure with a Dirac cone and Rashba-type spin splitting of the bands. Moreover, recently it was found that $PbTaSe_2$ contains one-dimensional topological nodal-lines in k space, which are in contrast to the Weyl semimetals, where the bulk Fermi surface has zero dimension. The Raman scattering measurements were done not only on Pb_xTaSe_2, where x is the concentration of Pb up to x = 1, but also on parent compound - $TaSe_2$. Thereby, the crossover from charge density wave (CDW) phase at T_{CDW} = 90 K to superconductivity at T_c = 3.8 K could be studied.

Another issue of this thesis is the investigation of solar energy materials. The current aims of scientists in this field are to make robust solar cells which would need less resources, i.e. cost-effective preparation and processing, which are simple, not poisonous and have high enough efficiencies. As a matter of fact, there are several candidates to meet the demands of the present photovoltaic market. However, in this thesis we would like to emphasize the solar cells based on cuprous oxide - Cu_2O. In fact, there are big enough amounts of copper existing in the Earth and also copper oxides are chemically stable and non-poisonous (except for Cu^{1+}) materials. In addition, solar cells based on Cu_2O have theoretical maximal power conversion efficiency around 20 %. Nevertheless, during the preparation of the Cu_2O another undesirable component - cupric oxide CuO may appear and which will change the properties of the final solar cell. Therefore, it is essential to gain pure Cu_2O for application reasons. Raman scattering technique is a reliable, fast and non-destructive method to investigate semiconductors as well as their crystal structure and composition, which in turn helps to distinguish the remnants of the unwanted components, that might appear during the preparation process. In this thesis also such aspects as the selection of the substrate (glass or even flexible plastic), preferable preparation method and the basic characteristics of the solar cell devices are discussed.

Chapter 2

Basics of Raman Scattering

Raman scattering spectroscopy is an experimental method to probe all kinds of matter: solids, liquids and gases. It is a light scattering technique, where a small fraction of light, which is inelastically scattered from a sample, is analysed by frequency. The first prediction of the Raman effect was done by Smekal in 1923 [1] in terms of periodically modulated polarizability and the corresponding quantum mechanical explanation of the effect was given by Kramers and Heisenberg in 1925 [2]. Two independent groups in 1928 proved this effect experimentally for different materials, one is indian group of C.V. Raman, which detected inelastic light scattering in organic liquids and a second one in Soviet Union by G. Landsberg and L. Mandelstam in quartz crystals. Two years later C.V. Raman was awarded a Nobel prize for the discovery of this effect. In 1960, after invention of the laser, Raman spectroscopy became an extremely useful tool for material investigation, since the Raman effect itself is a quite rare event, only one out of million of photons is scattered inelastically and it also needs a source of photons with small linewidth. In addition, the inelastic scattering technique allows to analyse non-destructively the composition, the lattice vibrations of compounds with little to no sample preparation. With Raman spectroscopy one can investigate not only crystal lattices and lattice dynamics, but also one can probe electronic and magnetic excitations, which makes Raman spectroscopy a versatile and powerful technique for material studies.

2.1 Theoretical Considerations

The following outline of the theory of Raman scattering process is based on the review articles by P. Lemmens and K.-Y. Choi [3].

Raman scattering process is a two-photon process, where an incident photon with frequency ω_i, polarization $\vec{e_i}$ and momentum $\vec{k_i}$ hits the matter and induces the polarization $\vec{P}(\omega, \vec{r})$. Afterwards, a new photonic state with frequency ω_s, polarization $\vec{e_s}$ and momentum $\vec{k_s}$ is scattered as demonstrated in Fig. 2.1. The intensity of such dipole-like radiation is proportional to $I \propto (w_s)^4$. The crystal momentum and energy conservation during the scattering process experience the general conservation laws of momentum and energy:

$$\hbar q = \hbar k_i - \hbar k_s \tag{2.1}$$

$$\hbar \Omega = \hbar \omega_i - \hbar \omega_s, \tag{2.2}$$

where $\hbar q$ and $\hbar \Omega$ are the momentum and energy difference between scattered and incident photons, respectively. $\hbar \Omega$ is the energy shift of the scattered photon and it is also known as a "Raman shift". If there is no energy difference or its amount is negligibly small, then the Rayleigh scattering is taking place, i.e. there is no energy transfer and the scattering is elastic. If the Raman shift $\hbar \Omega < 0$, then such scattering is called Stokes scattering and if $\hbar \Omega > 0$ then it would be Anti-Stokes scattering, which happens more seldom in comparison to Stokes scattering. Moreover, it is possible to use Stokes/Anti-Stokes ratio to investigate heating effects [4].

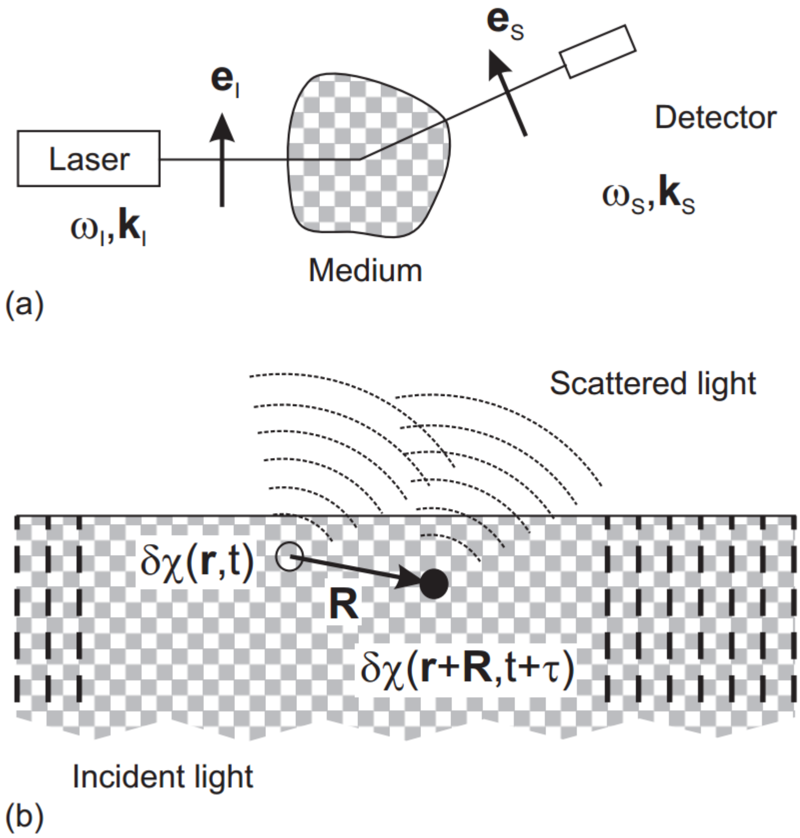

Figure 2.1: (a) Standard sketch of the light scattering process. (b) Interference of secondary waves from different points inside the incident beam [3].

The propagation of the light in matter will lead to the polarization:

$$\vec{P}_{\omega} = \epsilon_0 \chi(\omega) \vec{E}, \tag{2.3}$$

where $\chi(\omega)$ is the specific characteristic of the material, i.e. the electronic susceptibility tensor. χ remains constant in space and time in a homogeneous material. The modulation of χ in time and space by thermal and quantum fluctuations leads to scattering processes inside real matter. The correlation function of the fluctuations yields the spectral density of states:

$$\rho(q,\omega) \sim \int < \delta\chi^*(q,t)\delta\chi(q,0) > e^{i\omega t} dt, \tag{2.4}$$

where $\vec{q} = \vec{k}_i - \vec{k}_s$ and $\omega = \omega_i - \omega_s$, which are actually the wave vector and wave number shifts with respect to the conservation in the scattering process.

Internal degrees of freedom, such as phonons, or density fluctuations contribute to the fluctuation spectrum $\chi(\omega)$ in solids. The latter has a feeble scattering continuum which rapidly declines in intensity as function of Raman shift. The former fluctuations generate peaks in $\rho(\omega)$ at the frequencies according to the energy of excitations. Normally, the Raman shifts of phonons in solids range from 50 to 1000 cm^{-1}, whereas molecular vibrations might range up to 3500 cm^{-1}. A typical unit in Raman scattering spectroscopy is a *wave number*, [1 cm^{-1}], which is in fact the difference of the inverse of the corresponding wavelength λ in [cm]. The Raman shift can be converted in other units used in solid state physics as following: 1 [cm^{-1}] $\approx$ 1.44 [K] $\approx$ 1/8 [meV] $\approx$ 33 [GHz].

An additional contribution to Raman scattering is quasi-elastic scattering, which is normally characterized by a broad mode at 0 cm^{-1} position with a Gaussian line shape or Lorentzian line shape. The former originates from spin diffusion [5], whereas the latter one arises from energy density fluctuations [6]. Quasi-elastic scattering may be observed in materials with structural transition above T_s. In this case it occurs due to phonon density fluctuations, while below T_s new soft phonons are formed. Quasi-elastic scattering can also be observed in magnetic materials above the ordering temperature. Prerequisite for it is that the light has to be polarized along the magnetic exchange paths. The integrated intensity corresponds to the magnetic part of the specific heat C_m:

$$I(\omega) \sim C_m T^2 \frac{D_T k^2}{\omega^2 + (D_T q^2)^2} \tag{2.5}$$

where D_T is the thermal diffusion constant.

The probability of inelastic scattering P_{if} in a crystal can be written with respect to Fermi's golden rule of the second order perturbation theory as [7]:

$$P_{if} = \frac{2\pi}{\hbar} \rho_{dos}(\omega_S) |H(\vec{k}_I, i : \vec{k}_S, f)|^2 \delta(\hbar\omega_I + E_i - \hbar\omega_S - E_f), \tag{2.6}$$

where E_i is the energy of the initial state of the system and E_f the same for the final state. $\rho_{dos}(\omega_S)$ denotes the density of states of photons which obtained by $\rho(\omega_S) d\omega_s d\Omega = (1/2\pi c)^3 \omega_S^2 d\omega_S d\Omega / \hbar$, where $d\Omega$ is a solid angle. The interaction between the light and the crystal structure is described by Hamiltonian, $H(\vec{k}_I, i : \vec{k}_S, f)$, which has to be defined. The effective Hamiltonian can be determined in terms of the polarizations and considering the fact that the size of atoms is much smaller than the wavelength of the incident and scattered light:

$$H(\vec{k}_I, i : \vec{k}_S, f) = \sum_{r,\alpha,\beta} E_I^\alpha \chi(r)^{\alpha\beta} E_S^\beta, \tag{2.7}$$

where α and β are the Cartesian coordinates. The electric field is denoted in terms of the photon creation (destruction) operator, $b^\dagger(k)$ $(b(k))$:

$$\vec{E}_I = i\sqrt{2\pi\hbar\omega_I} E_I \vec{e}_I [b(\vec{k}_I) - b^\dagger(-\vec{k}_I)], \tag{2.8}$$

where $\vec{e_I}$ stands for the polarization vector of photon. Finally, the overall Raman scattering intensity can be written as:

$$I_R \sim \omega_I \omega_S^3 \int \ll \chi(\vec{k_I}\vec{k_S};t)\chi^\dagger(\vec{k_I}\vec{k_S};0) \gg e^{i\omega t} dt \tag{2.9}$$

The brackets $\ll \cdots \gg$ mean a thermodynamic average. It is worth to note that the Raman scattering includes a pair of correlation functions of the fluctuating polarization. The dipole matrix elements $< f|\vec{M}_\beta|i >$ along with the moments $\vec{M}_\alpha = er_\alpha$ give the explicit form of the susceptibility between the initial and final states with $\omega_{fi} = [E_f - E_i]/\hbar$:

$$\chi_{\alpha\beta}(\omega) = 2\sum_{i,f}\int < i|\vec{M}_\alpha|f >< f|\vec{M}_\beta|i > \times[\frac{1}{\omega_{fi}-\omega} + \frac{1}{\omega_{fi}+\omega}]\frac{d^3k}{(2\pi)^3}, \tag{2.10}$$

where number 2 stands for the spin.

The Raman spectra of solids are normally governed by phonon modes. An optical phonon $\nu(= 1, ..., 3N_c)$, where N_c the number of ions per unit cell, comprised of atomic displacements with the eigenvector Q_ν. They can be treated as a very slow ionic displacement in an adiabatic approximation which in turn will lead to a *static* potential within the unit cell $\delta U_\nu(r)$. The energy of the initial state will be altered by $\delta E_{i,\nu} =< i|\delta U_\nu(r)|i >$ due to the slowly varying potential, as well as the band wave function as $\delta|i >= \Sigma_{f\neq i}\frac{<i|\delta U_\nu(r)|i>}{E_f - E_i}|f >$. As a result, the susceptibility tensor in Eq. 2.10 will be expressed as:

$$\delta\chi_\nu^{\alpha\beta} = \sum_{a=1}^{N_c} Q_{a,\nu}\frac{\partial\chi^{\alpha\beta}(\omega)}{\partial Q_a}. \tag{2.11}$$

Consequently, the scattering intensity at the phonon frequency Ω_ν will be written as:

$$\rho(\omega) = \frac{1}{\pi} I_R \frac{\gamma_\nu}{(\omega - \Omega_\nu)^2 + \gamma_\nu^2}. \tag{2.12}$$

Here I_R is intensity from Eq. 2.9 and γ_ν is the phonon linewidth. If we put Eq. 2.10 into 2.11 we notice that the integrated intensity of phonons is defined by two contributions. The first one corresponds to the polarization of band wave functions and the change in the interionic distances $\partial < f|\vec{M}_\alpha|i > /\partial Q_a$. Another contribution is from the dependence of the band energy on the ion configuration, $\partial \omega_{fi}/\partial Q_a$. Since there is a big difference between the photon energy ($\hbar\omega_i \approx$1.5 - 2.5 eV) and phonon energy (less than 100 meV), the one-phonon Raman scattering process is not due to the direct light-phonon interaction, but it rather originates from the third order time-dependent perturbation theory [3]. The basic scheme of the process represents the Feynman diagram in Fig. 2.2.

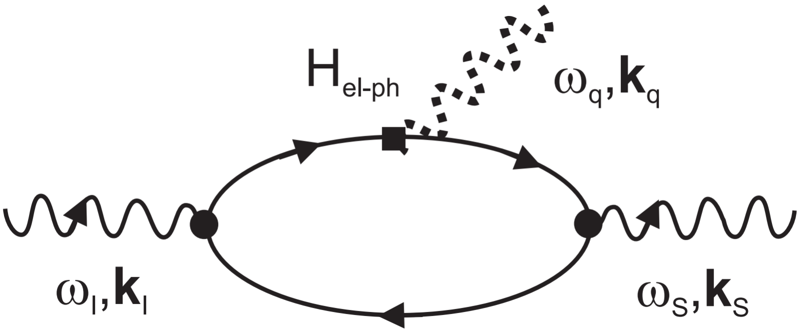

Figure 2.2: Sketch of the first-order phonon scattering process [3].

There are three virtual electronic transitions which take place in the Raman scattering process:

1) A virtual electron-hole pair state is excited by incident photon through the electron-radiation coupling.

2) A transition of the electron (Stokes process) or hole (anti-Stokes process) to another state occurs due to the electron-phonon interaction.

3) The transition to the electronic ground state is caused by

recombination of the electron-hole pair emitting the scattered photon.

The corresponding Hamiltonian of the phonon excitation will be written as:

$$H_R = -\frac{e}{mc}\vec{p}\cdot\vec{A} + \sum_{ijk} g_{ij}(k)(b^{\dagger} + b)c^{\dagger}_{ik}c_{jk}. \tag{2.13}$$

Here, $g_{ij}(k)$ is the electron-phonon coupling between the i and j band, $b^{\dagger}(b)$ and $c^{\dagger}_{ik}(c_{ik})$ are the phonon and electron creation (destruction) operators, respectively. The (1) and (3) steps are involved in the first term of the Eq. 2.13 and it denotes a scattering process via an intermediate state yielding an interband transition. The second term in the Eq. 2.13 is a linear contribution with respect to the electron-phonon interaction.

The phonon modes in the compounds, depending on their crystal structure, i.e. the presence of the inversion center, can be either Raman or infrared active. However, some vibrations might be infrared active as well as Raman active. In order to define the Raman active modes and the corresponding selection rules one has to employ the group theory. It consists of the following steps: (i) the site symmetry of each atom of the unit cell has to be determined, then (ii) the irreducible representations with the certain number of allowed phonons have to be derived and, finally, (iii) the Raman-allowed modes will be obtained by subtraction of the infrared-active, silent and acoustic modes from the irreducible representation. Crystallographic data bases, as Bilbao [8], consist of useful information for the steps described above. The assignment and calculation of phonon modes can be done by shell lattice models and a comparison with the compounds with the similar crystal structure.

The so-called Porto notation is employed very often to give a description of the used scattering geometry in Raman spectroscopy experiments. It has normally the following form: *a(bc)d*, where the letters denote the Cartesian coordinates x, y and z. The Porto notation gives an information about both the directions of incident and scattered light (*a* and *d*, respectively) and directions of the polarizations (*b* and *c*). For example, the Porto notation for the measurement in Fig. 3.10 is *z(xx)z*.

The Raman phonon modes are assigned with regard to their dimensionality, for instance, A_{1g} and B_{1g} (one-dim.), E_{2g} (two-dim.) or T_{1g} and F_{1g} (three-dim.). The letters A and B stand for the positive or negative value of χ with respect to rotation about the principal axis. The indices *g* and *u* denote *gerade* and *ungerade* with respect to the inversion center, while the numbers 2 and 3 stand for a symmetry with respect to other rotations or reflections. As an example, the irreducible representation of the Raman-active modes will look as following:

$$\Gamma = A_{1g} + 2E_g + B_{2g}, \tag{2.14}$$

where one would expect altogether 4 phonon modes. The corresponding Raman tensors for such configuration are shown below:

$$A_{1g} = \begin{pmatrix} a & 0 & 0 \\ 0 & a & 0 \\ 0 & 0 & b \end{pmatrix}, \quad B_{2g} = \begin{pmatrix} 0 & d & 0 \\ d & 0 & 0 \\ 0 & 0 & 0 \end{pmatrix}, \quad E_g = \begin{pmatrix} 0 & 0 & e \\ 0 & 0 & f \\ e & f & 0 \end{pmatrix}.$$

As it seen from the matrix representations, the A_{1g} mode will be observed in the Raman spectra only if the incident and scattered light are parallel to each other and to one of the crystallographic axis of the investigated crystal, whereas B_{2g} mode is allowed only at crossed ($\vec{e}_i \perp \vec{e}_s$) polarization configuration.

2.2 Experimental Setup

The sketch of the Raman scattering setup is depicted in Fig. 2.3. It may be divided into several logical parts, which are (i) the light source and corresponding optical elements it goes through, (ii) the attached sample in the cryogenic environment and (iii) the spectrometer part together with detector. In this work two different Raman setups were used, which differ in a sense that one is optimized for cutting off the quasi-elastic light together with high resolution, whereas another setup utilizes the microscope for investigation of small samples.

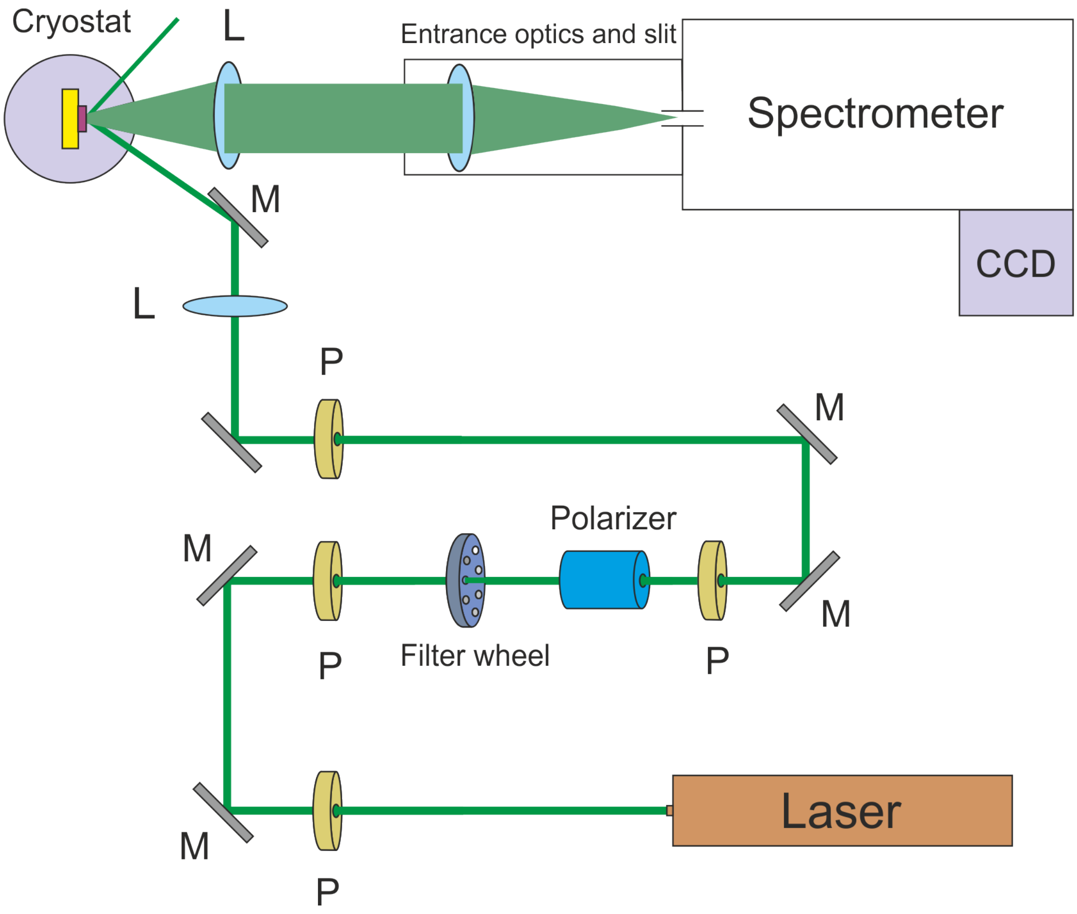

Figure 2.3: Basic scheme of the Raman scattering setup with quasi-backscattering geometry.

Light sources

For the measurements in the framework of this thesis two lasers were used: a nobel gas Ar-Kr ion laser (Innova 70 Spectrum) with chosen laser lines at λ = 476 nm, 488 nm, 514.5 nm, 532 nm, 568 nm and 647 nm with the power of P_{max} = 10 mW and a frequency-doubled Nd:YAG laser (Coherent) with λ = 532.1 nm and power P_{max} = 20 mW. Although the noble gas ion laser needs a cooling system and consumes big amount of electrical energy, it is convenient and important to use for resonant Raman scattering measurements. The plasma filter is used to reject secondary lines (plasma lines) from the desired frequency line.

Optical elements

After filtering out, the light propagates along the optical table and hits different metal-coated mirrors (M), which in turn steer the light in a desired direction. The last mirror in front of the cryostat defines the angle of incident light on the compound of interest. Since the angle is not 180 degrees, such scheme is called "quasi"-backscattering. Such geometry permits to get rid of needless quasi-elastic light. However, the Raman setup with a microscope utilizes true back-scattering geometry and has x50 magnification objective with a laser spot of about ~ few microns. In the case of the triple monochromator, the laser spot is around ~ 100 microns. The pinholes (P) are also available, which can adjust the power and the size of the laser spot. In order to reduce the heating effects during the light scattering experiments, the laser power for setup with triple monochromator was set to ~ 5 mW, whereas for the setup with microscope the power was set to ~ 3 mW.

To choose the appropriate polarization, the polarisers lambda/2 (for linear polarization) and lambda/4 (for circular polarization) wave plates were employed.

Cryostat

Raman scattering experiments at low temperatures were done in a closed cycle cryostat (Oxford Cryomech PT405). Such system has a constant helium flow and helps to cover a temperature range from ~9 K up to the room temperature. The samples are contained in the vacuum chamber of the cryostat under a pressure of about $\sim 10^{-6}$ mbar. The cryostat is mounted on the optical table and can be moved in all directions (x, y and z) for the sake of experiments, e.g. focusing and changing the position of the sample and etc.

Sample preparation

Raman scattering experiments require clean surfaces of the samples for better quality of the spectra. To make sure that the surface does not contain dirt, fat and other unnecessary products which might appear on the surface during crystal growth processes, the appropriate preparation of the sample for the measurements is needed. Depending on the sample it can be done in different ways. If the surface of the bulk sample is flat and shiny, it is sometimes sufficient just (i) to wipe it off with a cotton swab soaked in acetone. However, if it is not enough and also the surface is rather rough, it may be necessary (ii) to polish the surface thoroughly with a diamond paste. One has to do it consequently, step by step. Normally it is done by polishing the surface with a diamond paste with the large grain sizes first and by ending it with the smallest possible grain size, e.g. 1 micron grains. After such procedure, a flat and shiny surface can be acquired. To remove the residue, such as crumbles of the sample, diamond paste and other remaining parts after polishing, it is essential to wash it in the ultrasonic bath in isopropanol and then in acetone for several minutes. In case of the two dimensional sample, i.e. layered material, it is especially important to have a clean and fresh surface, because it might degrade very fast if the sample is kept at ambient conditions. In order to have a suitable surface, it is appropriate (iii) to cleave the sample by removing the upper layer with a razor blade or even with a scotch tape.

To mount the sample on the cold finger of a cryostat either double scotch tape or silver paste (glue) are used. The latter makes better thermal conduction from the sample holder to the sample itself.

Spectrometer and Detector

The inelastically scattered light from the sample is gathered by a collecting lens (L), i.e. standard camera objective lens. Afterwards, the scattered signal is focused on the entrance slit of the spectrometer (Dilor XY 500). The width of the entrance slit affects also the resolution of the spectra, as well as other factors, such as the laser wavelength and the spectral range. The analyser (either lambda/2 or lambda/4 wave plates) allows to get the desired polarization. Inside the spectrometer, the light travels through monochromator stages, will be dispersed on holographic gratings and eventually will hit the liquid nitrogen-cooled CCD detector (charge-coupled device made by Horiba Jobin-Yvon). Such detector makes possible to detect single photons and to measure a broad frequency band. In order to increase the signal-to-noise ratio, several accumulations are taken and, in addition, the software removes the spikes, which are the result of cosmic muons falling on the detector.

Chapter 3

Light Scattering in Compounds with Strong Spin Orbit Coupling

3.1 The 2D Layered Pb_xTaSe_2 Superconductor

In searching for novel electronic materials two dimensional (2D), single-layered systems and their electronic states have recently been in the focus of interest. Examples are graphene-like materials based on a single atom species, but also compounds, like layered chalcogenides. While a structural rigidity and intrinsic large mobility are necessary preconditions for any application, other properties are also highly relevant. These are the possibilities to dope charge carriers and a large and non-linear electronic response, which could be due to electronic or electron-lattice coupling. Recently, also the importance of spin-orbit interaction and the control of disorder have been highlighted [9]. Layered chalcogenides show several interesting features which make them promising materials. There exist atomically thin layers with a defined number of lattice constants. Furthermore, doping may be achieved by intercalation. There exist charge density wave instabilities with interesting transport anomalies and comparably high transition temperatures, as well as superconductivity [10]. Upon an intercalation of Pb between the TaSe$_2$ layers, CDW is suppressed and a superconducting transition is increased to T$_c$ = 3.79 K in PbTaSe$_2$ [11]. PbTaSe$_2$ consists of alternating stacking of hexagonal TaSe$_2$ and Pb layers (see Fig. 3.1) and constitutes a moderately coupled, type-II BCS superconductor. Noticeably, the introduction of Pb to the TaSe$_2$ layers induces distinct structural and electronic changes. PbTaSe$_2$ lacks a center of inversion. The broken inversion symmetry, together with strong spin-orbit coupling (SOC) linked to the heavy Pb atom lifts the spin degeneracy of electronic bands and the superconducting states, are given by an admixture of spin-singlet and triplet. The Rashba spin splitting amounts to an order of 0.8 eV, which is comparable to that of the giant Rashba semiconductor BiTeI [12].

Electronic structure calculations reveal that in PbTaSe$_2$ the single-layer Pb sublattice generates a Dirac point at the K point of the Brillouin zone. Moreover, it interfaces with the TaSe$_2$ layers to create a superconducting superlattice and 3D massive Dirac fermions [11]. This suggests that PbTaSe$_2$ represents an exceptional system incorporating noncentrosymmetric superconductivity and nontrivial electronic topologies in a single material.

Of great importance is thus to elucidate the role of the Pb layers in determining structural and electronic properties of Pb$_x$TaSe$_2$. Raman spectroscopy is an experimental tool of choice as it is extremely sensitive to local lattice distortions or electronic modulations. In this chapter, we report on detailed Raman scattering measurements of the doped dichalcogenides Pb$_x$TaSe$_2$ with focus on tracing structural and electronic properties as a function of Pb concentration. The key observation is the appearance of new broad peaks in the low frequency regime, which are not part of symmetry-allowed Raman modes. As a possible origin, we discuss the formation of a PbSe phase in the interface between the Pb and TaSe$_2$.

3.1.1 Crystal Structure

In Fig. 3.1, the crystal structures of $TaSe_2$ and $PbTaSe_2$ are depicted. $TaSe_2$ has a layered structure of hexagons that consist of covalently bonded Ta and Se atoms. A plane of Ta atoms is sandwiched between two planes of Se atoms in a trigonal prismatic arrangement. In the high temperature phase, 2H-$TaSe_2$ has a crystal structure of hexagonal (space group $P6_3/mmc$) symmetry. For the $P6_3/mmc$ space group the irreducible representation of Raman active modes is given by $\Gamma = A_{1g} + 2E_{2g} + E_{1g}$. We note that E_{1g} modes are not allowed in the measured in-plane polarizations [13]. The crystal structure of Pb_xTaSe_2 is not yet determined. Rather, for $x = 1$, three possibilities have been proposed as listed in Table 3.1. Trigonal crystal structure D_3h (space group $P\bar{6}m2$) is the most probable, which yields $\Gamma = A' + 3E' + E''$ Raman active modes. The A′, E′ and E″ are correlated to A_{1g}, E_{2g} and E_{1g} modes of $TaSe_2$, respectively. The Pb doping leads to only one additional mode with E′ symmetry.

Table 3.1: Structural parameters and Raman tensors of $TaSe_2$ and $PbTaSe_2$ at room temperature.

Compound	Space group	c axis (Å)	Ta-Se dist. (Å)	Se-Se dist. (Å)	Raman tensors	Ref.
$TaSe_2$	$P6_3/mmc$	12.7	2.597	3.353	$A_{1g} + 2E_{2g} + E_{1g}$	[14]
$PbTaSe_2$	$P\bar{6}m2$	9.35	2.665	3.553	$A' + 3E' + E''$	[15]
	P6	9.35	2.665	3.553	$A'+3(1E') +1E''+3(2E')+2E''$	[16]
	P6/mmm	9.35	2.665	3.553	$A_{1g} + E_{2g} + E_{1g}$	[16]

3.1.2 Electronic and Magnetic Properties

Normally, a bulk three-dimensional metal has the low energy excitations on a two-dimensional Fermi surface in k space. However, there are some exceptions, in particular topological semimetals,

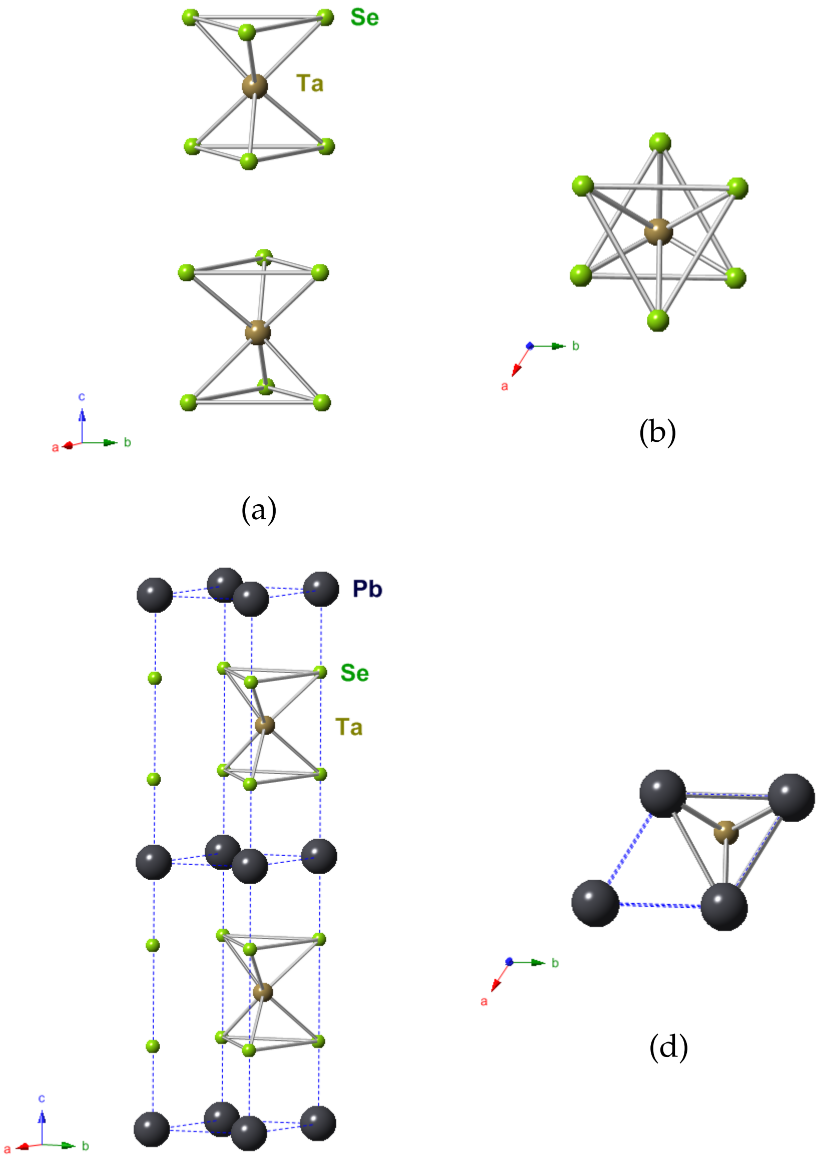

(a)

(b)

(c)

(d)

Figure 3.1: Sketches of the crystal structure of a) $TaSe_2$ (hexagonal symmetry), b) a view along the c axis and c) $PbTaSe_2$ (trigonal D_3h symmetry), and d) a view along the c axis, respectively.

which have one-dimensional Fermi lines or even zero-dimensional Fermi-Weyl points. The latter appear at a special location in k space, i.e. where the conduction band and valence band touch. In so-called Weyl semimetals, the degeneracy points are protected against any perturbation that keeps translation symmetry, while nodal lines are topologically protected by extra symmetries such as mirror reflection. The latter corresponds to $PbTaSe_2$, which has a peculiar band diagram together with 3D Dirac cones. Its electronic structure will be discussed in detail below in this chapter.

Systems with a lack of inversion symmetry display asymmetric spin-orbit coupling (SOC) in superconducting compounds, that leads to a parity-mixed superconducting state and the lifting of the spin degeneracy [17]. Thus, the symmetry of Cooper pairs will be nontrivially affected by the strength of the SOC, which is influenced by crystal structure as well as its elements [18]. Materials with strong SOC, as topological insulators (TI), have attracted a lot of attention of researchers in condensed matter physics [19]. Moreover, the massless Dirac electrons, which present on the surfaces of TIs and in some monoatomic hexagonal lattices, as graphene, are also found in the three-dimensional Dirac semimetals, like $Pb_{1-x}Sn_xSe$, Na_3Bi and Cd_3As_2 ([20], [21], [22]). The following paragraphs will describe the properties of the noncentrosymmetric hexagonal superconductor $PbTaSe_2$ with T_c = 3.8 K and a gapped Dirac cone at K point in its electronic band structure.

Magnetic susceptibility, transport and specific heat measurement results clearly indicate that single crystal $PbTaSe_2$ is superconducting with a transition temperature of T_c = 3.8 K [23]. The temperature dependent transport measurements of $PbTaSe_2$ are shown in Fig. 3.2, they indicate the clear appearance of the superconductivity below 3.8 K. The normal-state resistivity exhibits a metallic-like dependence ($d\rho/dT > 0$) with the residual resistivity ratio RRR ≈ 6 [24].

Electronic structure calculations of $PbTaSe_2$ are made in the framework of density functional theory (DFT) and shown in Fig.

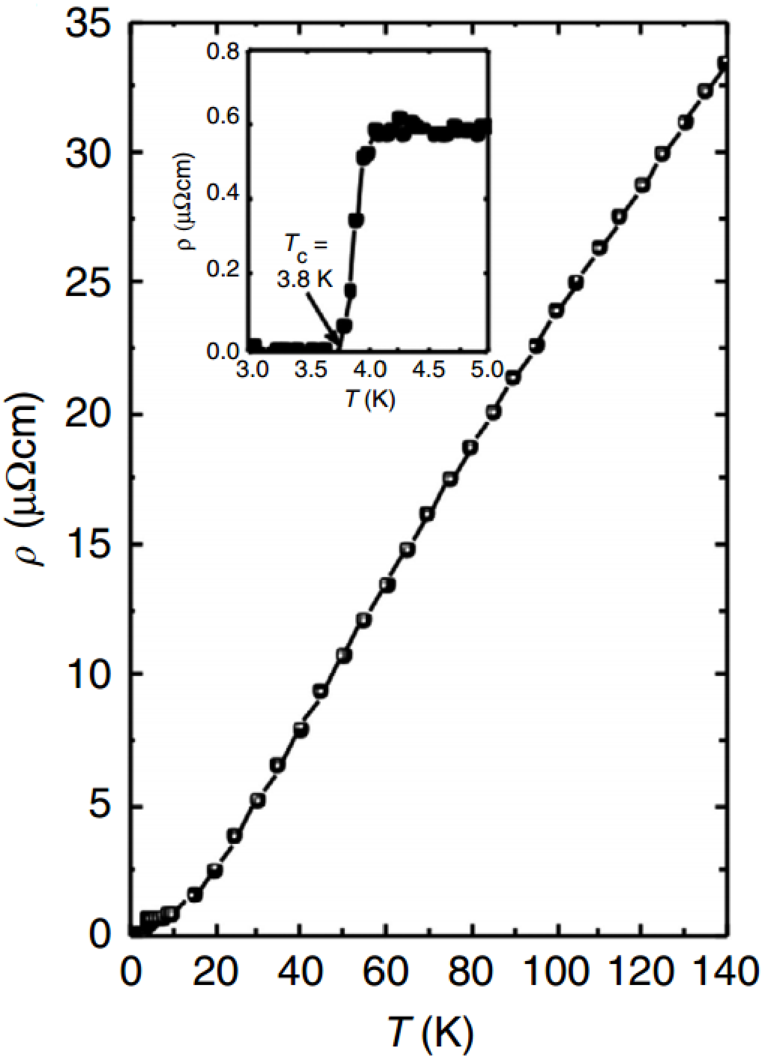

Figure 3.2: Temperature dependence $\rho(T)$ of PbTaSe$_2$ showing the superconducting transition at 3.8 K [23].

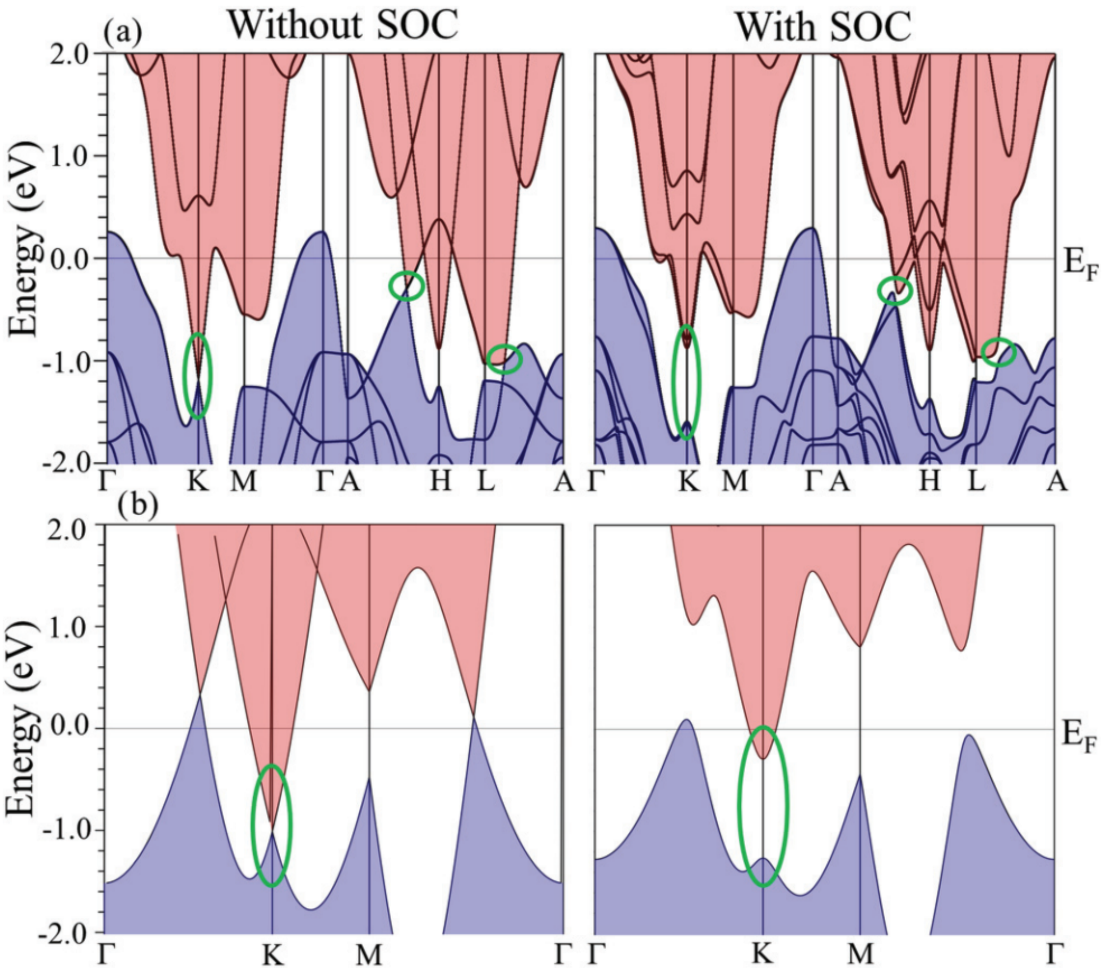

Figure 3.3: a) Calculated band structures of $PbTaSe_2$ with and without spin-orbit coupling (SOC). Green ovals highlight Dirac cone at *K* and band crossings along *A*-*H* and *A*-*L*, which are gapped when SOC is applied. b) Band structure of the two-dimensional Pb sublattice only in $PbTaSe_2$, where green ovals show the Dirac cone, which is gapped by SOC at *K* [24]).

3.3. They demonstrate a graphene-like Dirac cone at the *K* point of the Brillouin zone, which is gapped by strong SOC [24]. Here, the Dirac cone is gapped by around 0.8 eV, whereas in graphene it is gapped by just a few mK. Given that, $PbTaSe_2$ is considered to be topologically nontrivial. Moreover, the calculations reveal a couple of band crossings along *A-H* and *A-L*, which are absent along *Γ-K* and *Γ-M* (showing that the coupling in the *z* direction is essential) and they get gapped with the presence of the SOC. Around the *H* point of the $PbTaSe_2$ Brillouin zone one can easily observe large spin splitting which takes place due to the mixture of the inversion symmetry and strong SOC. Such spin splitting has a comparable value (tenths of eVs) as in the giant Rashba-type semiconductor BiTeI [12]. Also, in Fig. 3.3a, spin splitting takes place at the *M* and *L* points of electronic structure close to the continuous gap. Moreover, such large spin splitting gives a probability to the existence of the unconventional pairing mechanism in $PbTaSe_2$. Thus, it may lead to a nontrivial superconducting gap - another feasible way of supporting Majorana fermions at a cleaved surface of $PbTaSe_2$ [24].

The electronic structure of the pure Pb sublattice is shown in Fig. 3.3b. According to the calculations, it is assumed that the Dirac cone, demonstrated in the band diagram at the *K* point, is exclusively because of the Pb sublattice. Consequently, the metallic Pb sublattice becomes nearly fully gapped in the presence of SOC. Given that, one can make an assumption that some of the $PbTaSe_2$ charge carriers are, in fact, massive 3D Dirac electrons [24].

Recently, the research group of Z. Hasan [23] has stated that $PbTaSe_2$ also contains so-called topological nodal-line states. In comparison with Weyl semimetals, whose bulk Fermi surface is zero-dimensional, nodal-line semimetals have an one-dimensional curve-like band touching in *k* space, instead of point-like band touching. According to these predictions, such compound expands the family of topological materials, as topological insulators, Weyl and Dirac semimetals, and give a chance to study a new topological nodal physics. In order to fulfil the requirements of 1D band touching of valence and conduction bands to be topologically protected, one would require additional symmetries, like translation as well as mirror reflection. More details will follow in the next paragraphs.

Let us focus on other parts of the electronic band structure (obtained by method of generalized gradient approximation), which are shown in Fig. 3.4 [23].

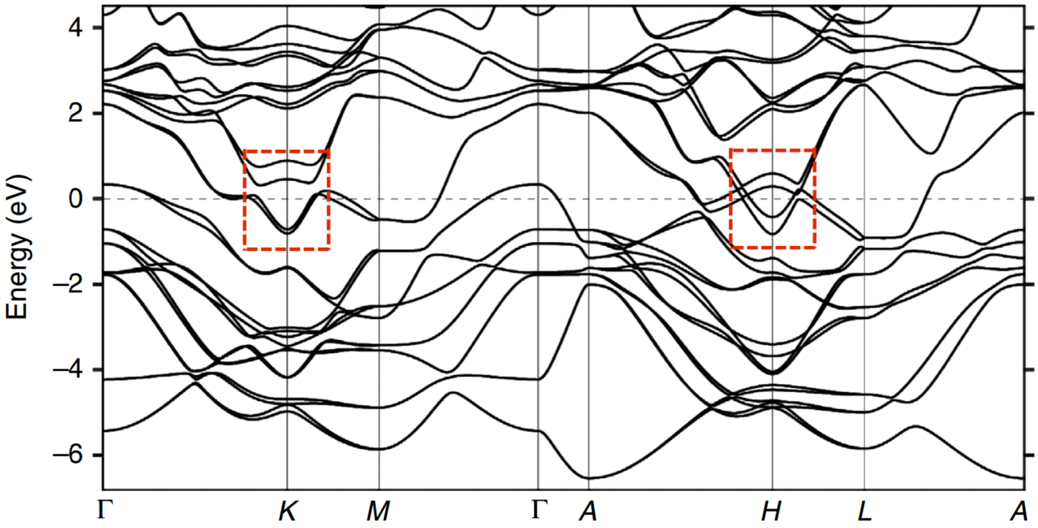

Figure 3.4: Bulk band structure of $PbTaSe_2$ [23].

Here, one can immediately see a couple of the distinct features nearby the Fermi level. First of all, it is a large hole pocket at the Γ point, whose states are mostly derived from the Ta $5d_{3z^2-r^2}$ orbitals, which are pointed out of the Ta atomic plane, taking the Ta plane as the x-y plane [23]. The next large contribution to the density of states close to the Fermi level comes from the four crossing bands around the H point and highlighted by the red dashed box in Fig. 3.4. These are two hole-like valence bands, which emerge from Ta - $5d_{xy}/d_{x^2-y^2}$ orbitals and two electron-like conduction bands from Pb - $6p_x/p_y$ orbitals. It is worth to notice that all orbitals are also invariant under the mirror operation R_z [23].

A closer look at the bands at H point with and without SOC is shown in Fig. 3.5. It can be seen that before inclusion of SOC, the

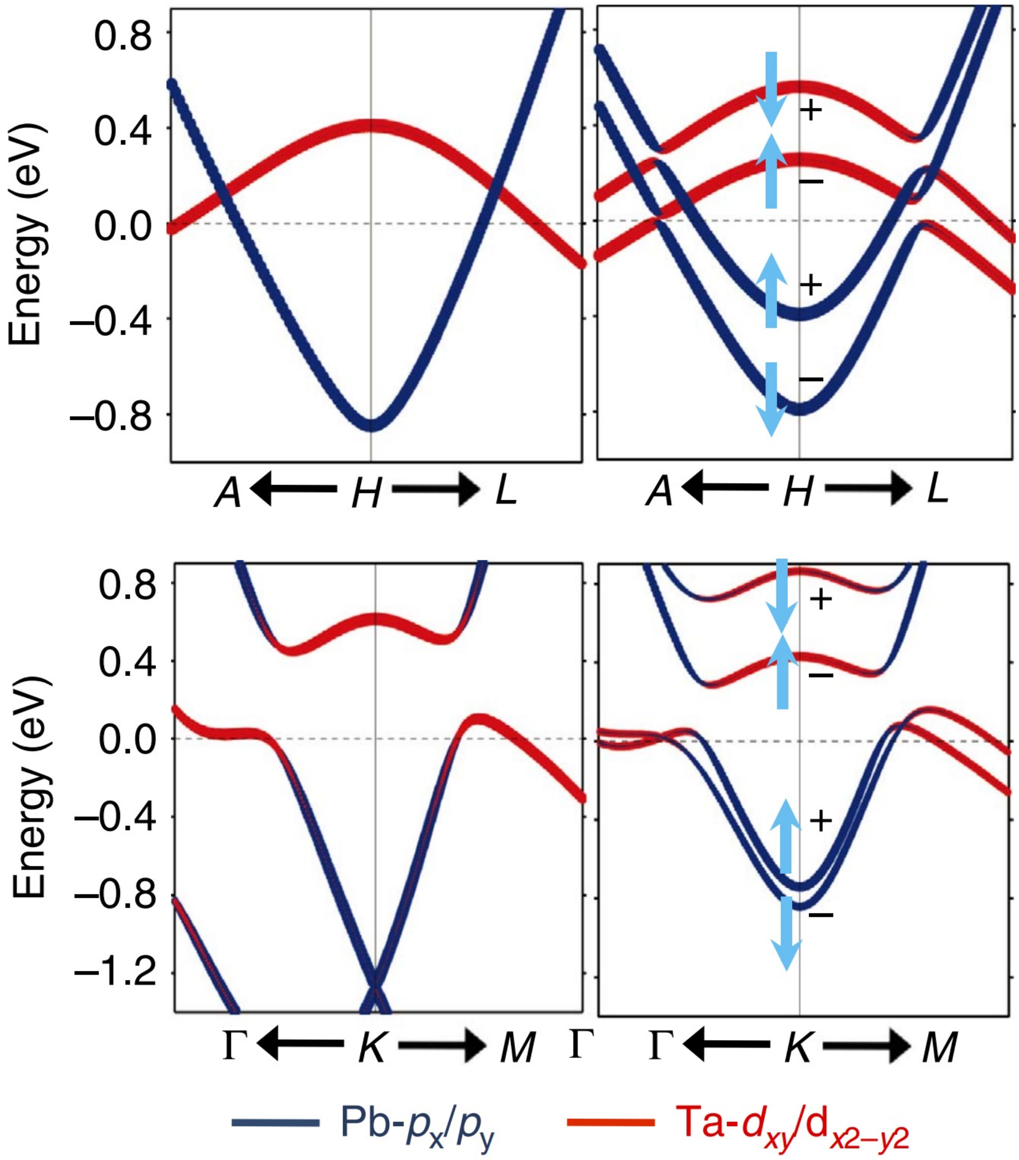

Figure 3.5: (upper panel) Electronic structure of PbTaSe$_2$ zoomed in at H with and without SOC. Red and blue colours correspond to orbital components as it states in the caption. The up and down arrows point out spin up and spin down along the z axis, respectively. (lower panel) The same as upper panel but for the band structure around K [23].

valence and conduction bands are spin-degenerate. These bands become non-degenerate if we induce SOC, i.e. each of them will have spin-up and spin-down alignments as well as have different mirror reflection eigenvalues, which are displayed in Fig. 3.5 as arrows and "+" and "-" signs, respectively. In this case, due to symmetry protection the crossing of bands with opposite mirror reflection eigenvalues stay gapless and they constitute a couple of nodal rings. In addition, a third nodal ring appears on the k_z=0 plane due to SOC inclusion [23].

Fig. 3.6a and 3.6b show an ARPES band structure measurement of $PbTaSe_2$ and its numerical calculations, respectively [23]. The calculations were made for the Pb-terminated (001) surface, where surface bands and bulk bands are indicated with white lines. The DFT band structure calculations nearly coincide with the real ARPES measurements, for instance, a surface band SS_1 has high intensity and goes through Fermi level between $\overline{\Gamma}$ and $\overline{K}$ high symmetry points. This surface band corresponds to the Pb-terminated (001) surface and it is associated with Dirac surface mode originating from a continuous bulk band gap opened by SOC (although $PbTaSe_2$ is considered to be a metal) [24]. Around $\overline{M}$ there are two bands, which are tails of the two Ta-5*d* bands. They, in turn, cross the two Pb-6*p* bands and create the so-called nodal rings close to $\overline{K}$ point. In the proximity of $\overline{K}$ we observe three concave bands with binding energies of 0.21, 0.75 and 0.80 eV. The band in the middle corresponds to the surface band and is indicated as SS_2, as shown in Fig. 3.6b. The upper and the lower bands are electron-like bands originated from Pb-6*p* orbitals.

The ARPES spectra taken at (001) Fermi surface with the 64 eV energy of incident photons and theoretical calculations are displayed in Fig. 3.6c and d, respectively. There are three distinct features: various circles around $\overline{K}$ point, a pocket with a hexagonal shape at the $\overline{\Gamma}$ point with smeared intensity inside and a dog-bone like contour around $\overline{M}$ point. The calculated data and the measurements seem to be consistent. Moreover, the intensity inside

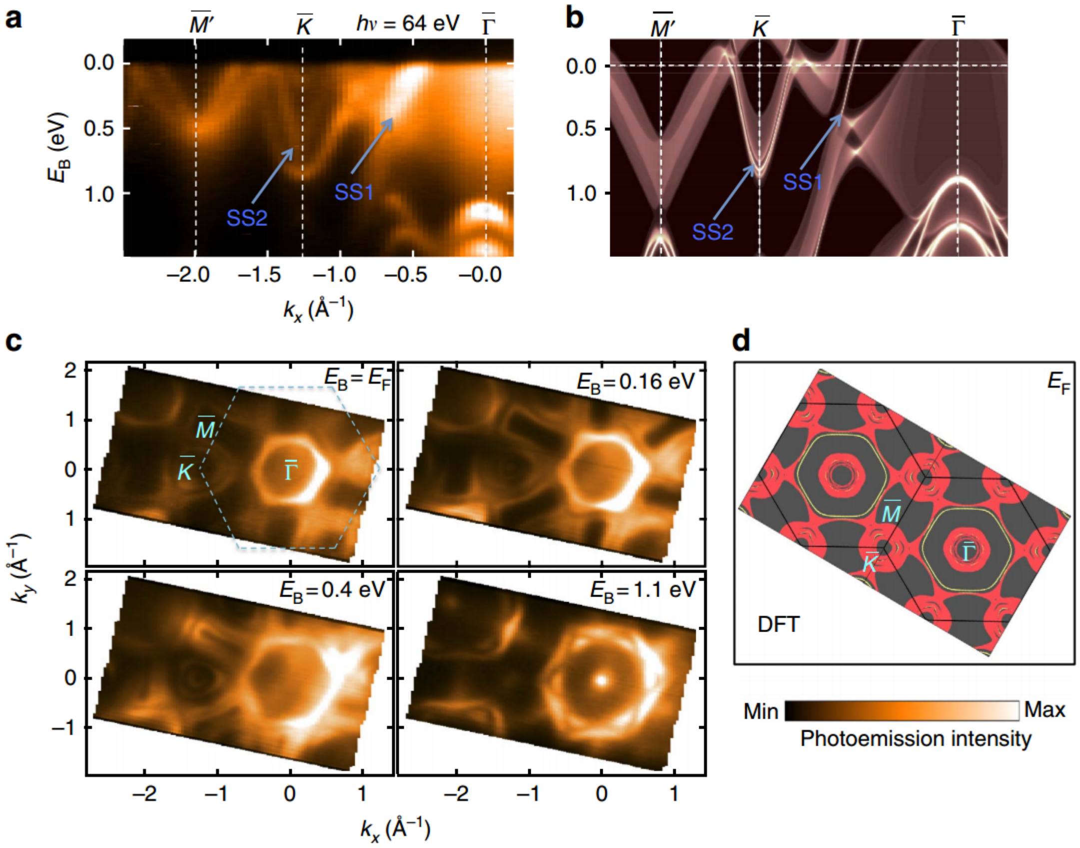

Figure 3.6: (a) ARPES spectra of PbTaSe$_2$ taken along $\overline{M}$ - $\overline{K}$ - $\overline{\Gamma}$ with 64 eV energy of photons. (b) DFT-projected surface bands and bulk bands of Pb-terminated (001) surface. (c) ARPES isoenergy contours obtained with 64 eV energy of photons. (d) DFT Fermi surface contour of PbTaSe$_2$ (001) surface. The surface states on (001) surface with Pb termination are highlighted by yellow lines [23].

the hexagon at $\overline{\Gamma}$ point is the bulk hole pocket at $\overline{\Gamma}$, whereas the hexagon itself is the surface band. The circles observed in the vicinity of $\overline{K}$ point are derived from the one branch of the Ta valence band and the dog-bone like contour around $\overline{M}$ point are from the other branch of the Ta valence band. With increasing of the binding energy, the Ta pockets shrink whereas Pb pockets enlarge outwards, which is in a good agreement with the characteristics of the hole-like Ta bands and electron-like Pb bands.

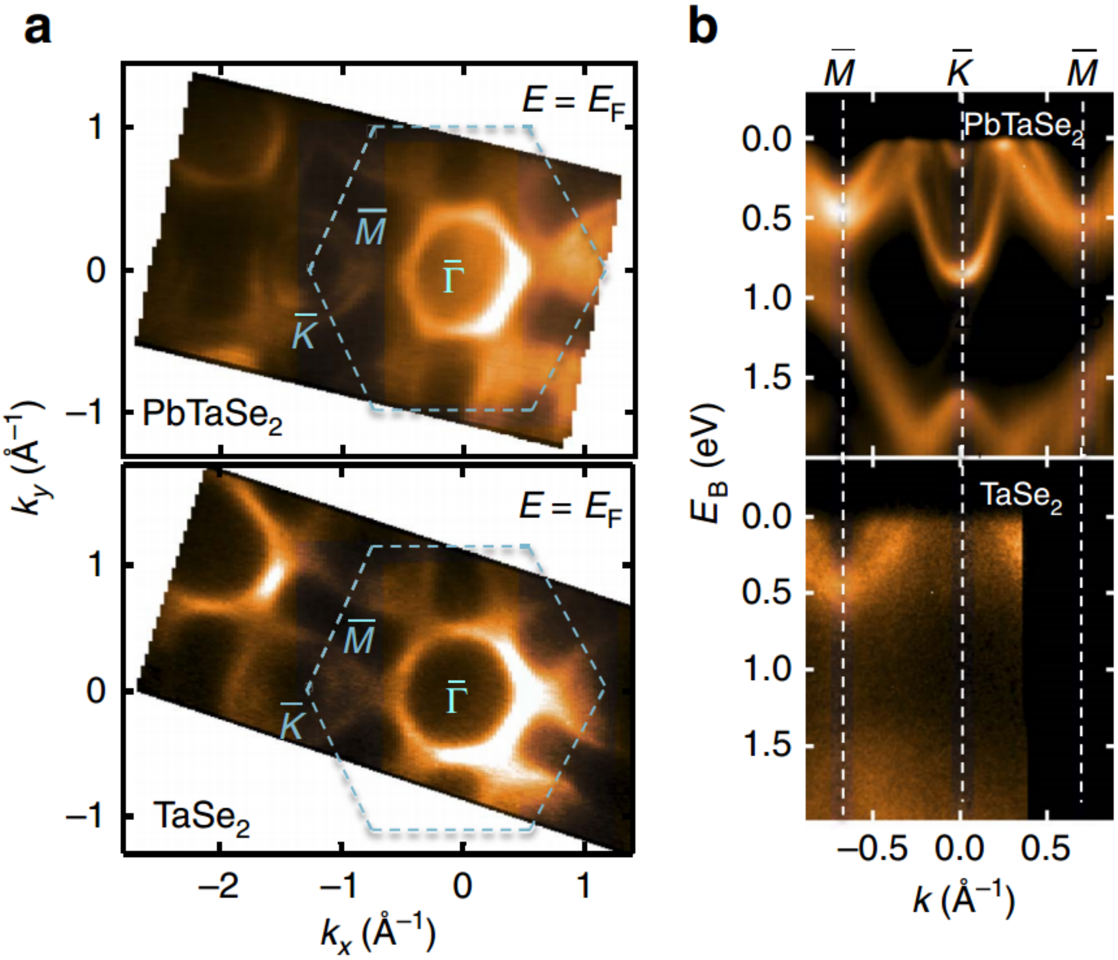

Figure 3.7: (a) Fermi surface contour of $PbTaSe_2$ and $TaSe_2$. (b) ARPES spectra taken along $\overline{M}$-$\overline{K}$-$\overline{M}$ for $PbTaSe_2$ (upper) and $TaSe_2$ (lower) [23].

$PbTaSe_2$ is obtained by Pb intercalation into $TaSe_2$, therefore its electronic structure can be tracked down from this process. To compare the electronic structures of $PbTaSe_2$ and its parental compound $TaSe_2$, the Fermi surface and band diagram along $\overline{M}$-$\overline{K}$-$\overline{M}$ are shown in Fig. 3.7a and 3.7b, respectively. The Fermi surface of $TaSe_2$ consists of one circle-shaped contour around $\overline{K}$ point and dog bone-shaped contour centred at $\overline{M}$ point. They correspond to Ta valence bands and are in a good agreement with previous investigations [25]. The contribution of Pb atoms to the Fermi surface is evidenced by the ring-shaped contours centred at $\overline{K}$ point. It can be easily seen along $\overline{M}$-$\overline{K}$-$\overline{M}$ in Fig. 3.7b, where $PbTaSe_2$ has electron-like bands at $\overline{K}$, while $TaSe_2$ does not have them.

The theoretical calculations and experimental ARPES data point out the electron-like Pb-6p bands at $\overline{K}$, which unavoidably cross the hole-like Ta-5d bands with a similar energy, forming the nodal rings.

The calculation of the band structure for Pb- and Se-terminated surfaces is shown in Fig. 3.8, where the projected bulk band on every cut from $\overline{K}$ point has three nodal points at 0.05, 0.15 and 0.03 eV above the Fermi level [23]. The first two points (NL1 and NL2) are located on the $k_z=\pi$ plane, whereas the latter one (NL3) is located on the $k_z=0$ plane. The corresponding nodal points are present at any arbitrary direction including $\overline{K}$, for instance along $\overline{K}$-$\overline{X}$ direction, the band diagram of which is shown in Fig. 3.8b and 3.8d.

For both Pb- and Se- terminated surfaces the isoenergy contour close to NL1 and NL2 nodal rings are plotted in fig 3.8e and f, respectively. As a matter of fact, surface states and gapless nodal points are located at every in-plane angle around $\overline{K}$ point. In addition, the nodal rings are protected against a gap opening by the crystalline symmetry. Indeed, if one shifts Pb atom above or below its original position (breaking the reflection symmetry) the

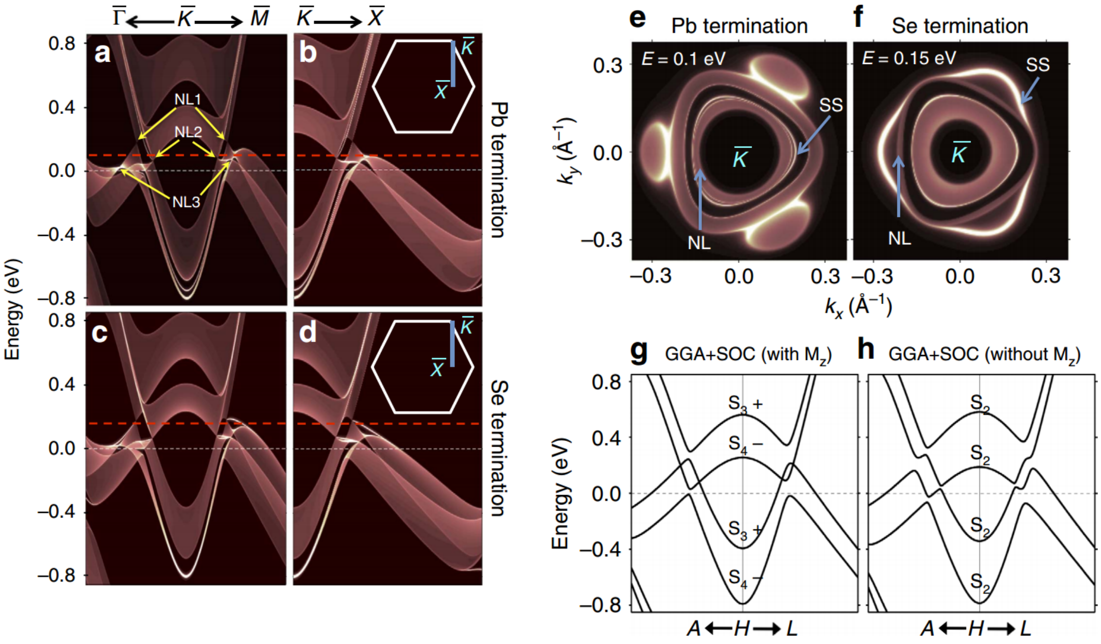

Figure 3.8: (a,b) DFT project bulk bands and surface bands (bright white lines) of Pb-terminated (001) surface along $\overline{\Gamma}$-$\overline{K}$-$\overline{M}$ and $\overline{K}$-$\overline{X}$, respectively. (c,d) Same as a,b but of Se-terminated (001) surface. (e,f) The isoenergy contour with the surface states (SS) and nodal-line states (NL). The energy is 0.1 and 0.15 eV above E_f for Pb- and Se- termination, respectively, as depicted by the red dashed lines in a-d. (g,h) Bulk band structure of $PbTaSe_2$ with and without the reflection symmetry, respectively. In h, the Pb atom is moved in the vertical direction [23].

gap will appear at each crossing point of the branches as depicted in Fig. 3.8h.

Considering the properties of the electronic structure of PbTaSe$_2$, topological nodal-line semimetals became a distinguished type of topological materials beyond topological insulators and Weyl semimetals. For instance, to control the novel properties of Weyl materials, the nodal-line states have an extra degree of freedom, i.e. the finite size of the nodal line. Moreover, due to high density of states at the Fermi level, the interaction-induced instabilities, which have been widely discussed for Weyl semimetals, will more probably appear in nodal-line states. In addition, a novel physics might emerge from the coexistence of the superconductivity and the topological nodal-line states in PbTaSe$_2$.

3.1.3 Experimental Details

Single crystals of TaSe$_2$ and Pb$_x$TaSe$_2$ (Fig.3.9a and 3.9b, respectively) were grown by chemical vapour transport method [16]. Raman scattering measurements were performed on single crystals of different composition from pure TaSe$_2$ to Pb$_x$TaSe$_2$ with $x = 0.25$, 0.33, 0.5, 0.75, and 1.0 in quasi-backscattering geometry. Light scattering polarizations are given by parallel (xx) and cross (xy) polarization within the crystallographic ab plane. Freshly cleaved sample surfaces were prepared at ambient pressure using scotch tape. Cleaved-off pieces and their opposite faces are quickly cooled down in vacuum to reduce surface deterioration. Temperature was varied between 8 K and 300 K using a closed-cycle cryostat.

As an incident Laser excitation a $\lambda = 532$ nm solid state laser and an Ar-Kr-ion multiline gas laser ($\lambda = 476$ nm, 488 nm, 514.5 nm, 568 nm, and 647 nm) were used. The laser power was set to P = 5 mW with a spot diameter of approximately 100 μm to avoid heating effects and deterioration of the samples which were mounted on a sample holder in vacuum. Six different laser lines allowed to probe effects of resonance Raman scattering.

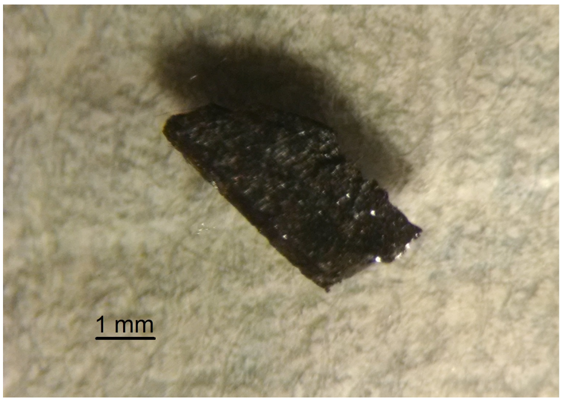

(a) $TaSe_2$

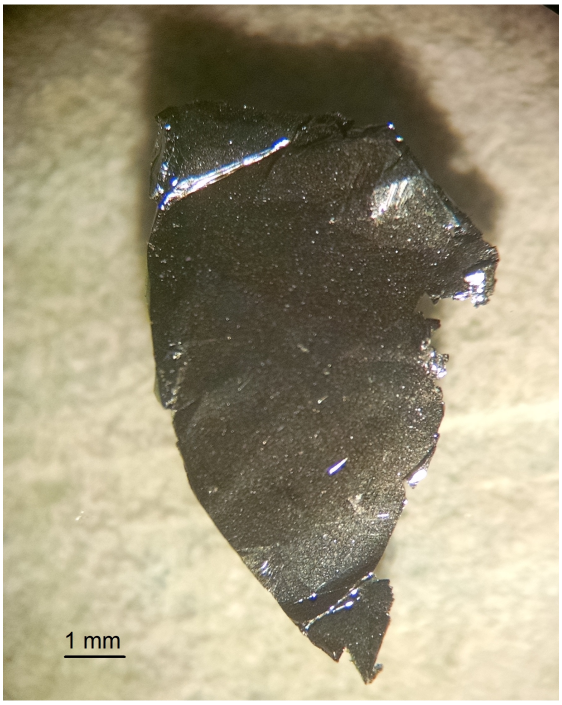

(b) $PbTaSe_2$

Figure 3.9: Microscope pictures of uncleaved a) $TaSe_2$ and b) $PbTaSe_2$.

Experiments at room temperature were performed using a micro-Raman setup (Horiba Labram) with λ = 532 nm. This enabled us to assign the symmetry of phonons (A_{1g} (A') and E_{2g} (E') modes) expected for backscattering geometry. The symbols in brackets correspond to Pb$_x$TaSe$_2$. The Raman spectra at low temperatures were collected using a triple Raman spectrometer (Dilor-XY-500) with an attached liquid-nitrogen-cooled CCD (Horiba Jobin-Yvon, Spectrum One CCD-3000V).

3.1.4 Properties of the Phonon Spectrum

Figure 3.10 shows Raman data of Pb$_x$TaSe$_2$ as a function of x. These spectra were collected by the micro-Raman setup. Therefore, their frequency range is limited by a filter that cuts off wavenumbers below 130 cm^{-1}. This means that the suppression of the low-frequency response is due to an instrument artefact by a notch filter. For $x = 0$, we observe two peaks at 236 and 209 cm^{-1} at T = 300 K. Our results are in excellent accordance with data from literature [26]. As depicted in the inset of figure 2, the 209 cm^{-1} mode corresponds to the E^1_{2g} mode involving in-plane stretching motions of the Ta and Se atoms. The 236 cm^{-1} mode is assigned to the out-of-plane vibrations of the Se atoms. We could not detect the anticipated E^2_{2g} mode known as a rigid layer mode due to its very low energy of around 23 cm^{-1} [27].

Upon introducing Pb atoms, a new peak appears at 267 cm^{-1} in addition to the two Raman modes E^1_{2g} (E′) and A$_{1g}$ (A′) as denoted by the asterisk in the left panel of Fig. 3.10. The extra mode is tentatively assigned to a 2LO phonon observed in the PbSe nanocrystals [28, 29]. The observed phonons are consistent with the factor group prediction for the P$\bar{6}$m2 space group. Increasing the Pb concentration, the phonon modes, pertaining to TaSe$_2$ sublattice, become narrower and are substantially suppressed. The Raman spectra are fitted to a sum of Lorentzian profiles in order to quantify the evolution of the phonon modes as a function of the Pb content.

The phonon resulting parameters are plotted in the right panel of Fig. 3.10.

With increasing x, the in-plane 209 cm^{-1} mode undergoes a large hardening by 19 cm^{-1}, suggesting a strong impact of the Pb doping on in-plane electronic properties. A close inspection reveals a step-like variation of the frequency with x. This may be related to different Pb ordered phases at low, intermediate and high Pb concentrations. Similar effects have been observed in $\mathrm{Na}_x\mathrm{CoO}_2$ with Na ordering [30, 31]. In addition, the drastic suppression of the scattering intensity and a line narrowing occur in the doping range of $x = 0.33$. This is ascribed to screening effects of phonons by electrons in the TaSe_2 layer, which become more itinerant through the formation of the Pb layer. This suggests that above $x = 0.33$ the interlayer interaction between the PbTaSe_2 layers destabilizes the CDW, which promotes a more metallic behaviour in the TaSe_2 plane.

3.1.5 Comparison with TaSe_2

To analyse further the influence of the Pb layer on the electronic properties, the x dependence of the frequencies of the E^1_{2g} and A_{1g} modes is compared with their frequencies as a function of the number of layers corresponding to the thickness of exfoliated crystals in Fig. 3.11 [26]. Overall, the A_{1g} mode varies little with x and thickness. The observed phonon shift is of an order of 1 cm^{-1}. This is contrasted by the E^1_{2g} mode, which hardens by 19 cm^{-1} with increasing x for $\mathrm{Pb}_x\mathrm{TaSe}_2$ and by 5 cm^{-1} with increasing number of layers in the exfoliated crystals [26]. Here we stress that Pb doping exerts a much stronger impact on the electric properties than the thickness variation. Obviously, this is linked to the interfacial effect between the graphene-like Pb and the superconducting TaSe_2 layers, which is absent for the exfoliated sample TaSe_2.

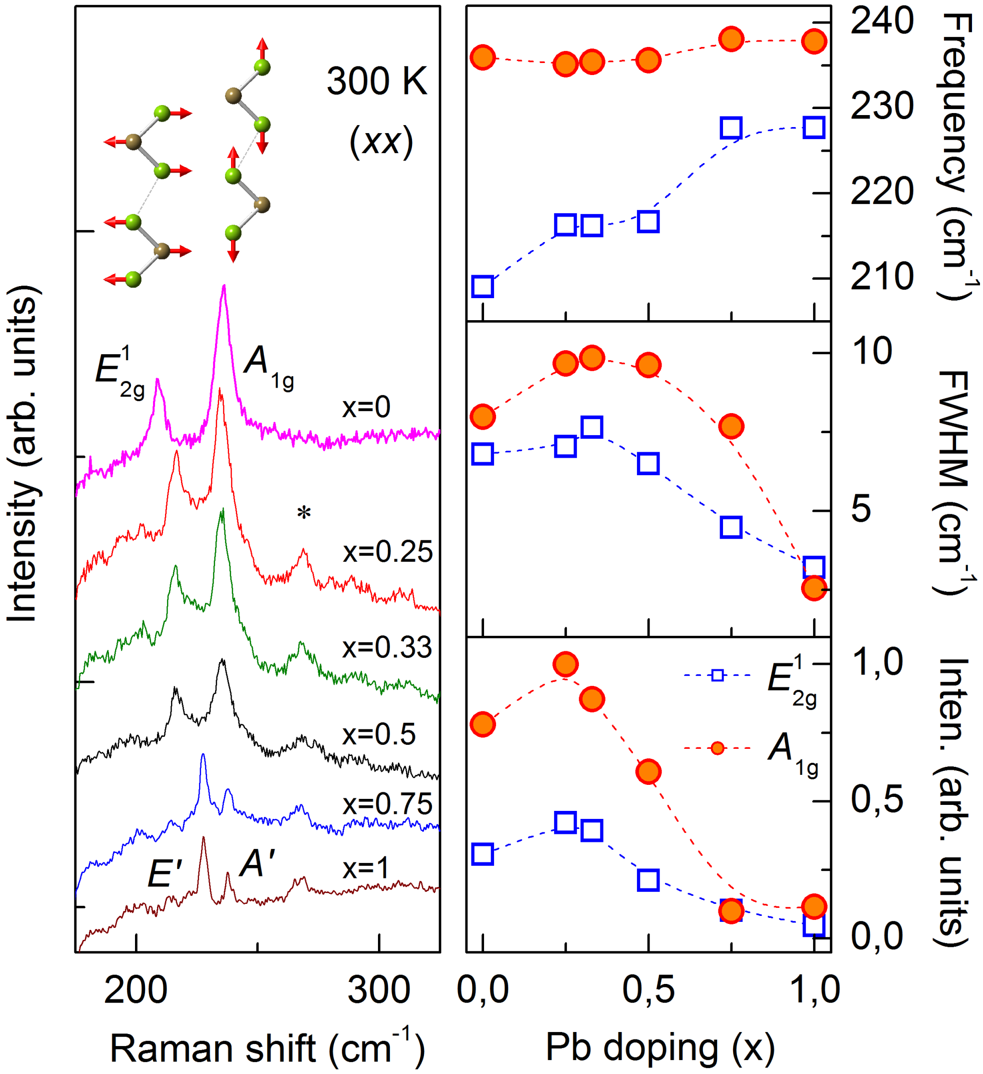

Figure 3.10: (Left panel) Polarized Raman spectra (xx) of Pb$_x$TaSe$_2$ (x= 0, 0.25, 0.33, 0.5, 0.75, and 1) measured at room temperature using λ = 532 nm. Spectra are shifted vertically for clarity. The insets depict the eigenvectors of the 228 and 238 cm^{-1} modes. The relative amplitude of the vibrations is given by the arrows. The green balls stand for the Se atoms, the olive ones for Ta atoms. The asterisk denotes a new phonon at 267 cm^{-1}, which appears upon doping Pb. (Right panel) The frequencies, full widths at half maximum, and integrated intensities of the phonons at 228 and 238 cm^{-1} as a function of Pb doping.

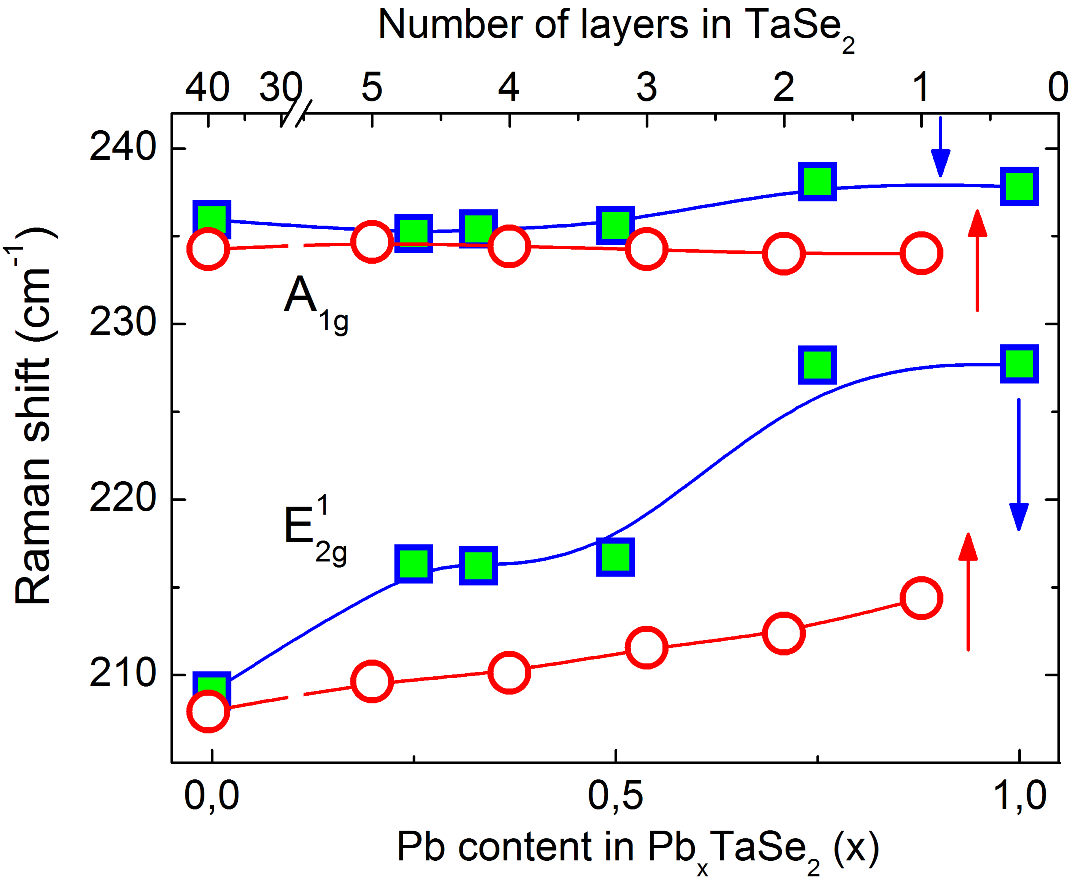

Figure 3.11: Comparison of phonon frequency vs. the number of layers (open circles and top axis, respectively) in exfoliated $TaSe_2$ [26] and phonon frequency vs. Pb concentration (filled squares and bottom axis, respectively) in bulk single crystals of Pb_xTaSe_2.

3.1.6 Temperature-induced Effects in Pb$_x$TaSe$_2$

We now turn to the temperature dependence of Raman spectra of Pb$_x$TaSe$_2$ (x = 0, 0.33, and 1), shown in Fig. 3.12. For temperatures T > T$_{ICDW}$ = 123 K, TaSe$_2$ exhibits a broad maximum at around ~ 140 cm^{-1} in addition to the two phonon modes discussed above. The former has been attributed to two-phonon Raman scattering amplified by anharmonicity in systems with a Kohn anomaly [27, 32]. In the temperature range between T$_{ICDW}$ and T$_{CCDW}$ the two-phonon scattering evolves to a quasielastic response. Below T$_{CCDW}$ = 90 K a number of sharp, well-defined Raman modes at 46, 63 and 81 cm^{-1} appear. They are linked to the CDW 3a × 3a × c superlattice [27, 32]. As to Pb$_x$TaSe$_2$ (x = 0.33 and 1), the broad maxima at 40, 80, and 135 cm^{-1} are present in the whole measured temperature range while the background is being suppressed with decreasing temperature (see Fig. 3.12b and 3.12c). Their assignment will be given below.

In Fig. 3.13, we summarize the temperature dependence of the frequency, the linewidth and intensity for TaSe$_2$. Both E^1_{2g} and A$_{1g}$ modes show a distinct change through T$_{CCDW}$ and T$_{ICDW}$. In particular, the linewidth appreciably decreases and the intensity increases steeply upon cooling through T$_{CCDW}$. This is due to the partial depletion of electronic states at the Fermi surface, which leads to a weakening of charge screening effects [**?**].

Next, we will discuss the temperature dependence of the phonon modes and the background scattering for PbTaSe$_2$, which is summarized in Fig. 3.14 and 3.15. The phonon frequency hardens by 3 - 5 cm^{-1} with lowering temperature. This is explained by anharmonicities in the lattice potential energy as commonly observed, e.g. in MoS$_2$ and graphene [33]. This is comparable to the change in frequency, $\Delta\omega$ = 4.5 cm^{-1}, of TaSe$_2$. The FWHM of the in-plane E′ and A′ mode of PbTaSe$_2$ is smaller than the respective mode of TaSe$_2$. The change of the FWHM over a temperature range of T = 8 - 300 K amounts to $\Delta\Gamma \approx$ 1 - 2 cm^{-1} for PbTaSe$_2$ and $\Delta\Gamma \approx$ 5.7 cm^{-1} for TaSe$_2$. No discernible anomaly can be found in the

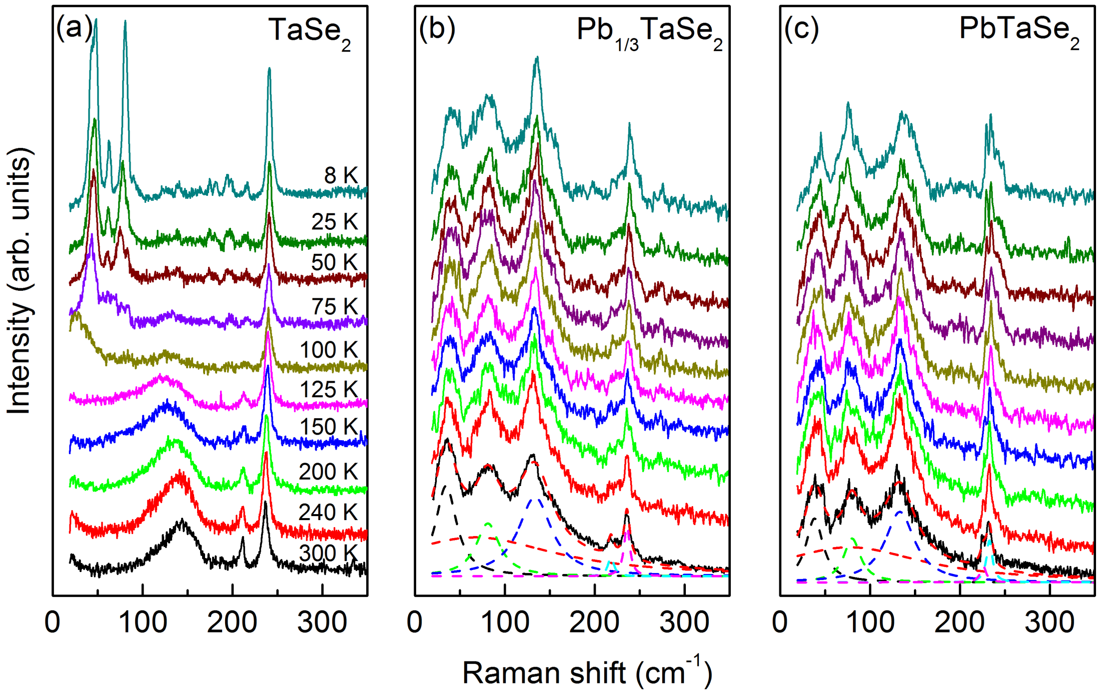

Figure 3.12: Polarized Raman spectra of $TaSe_2$ (a), $Pb_{1/3}TaSe_2$ (b) and $PbTaSe_2$ (c) in (xx) polarization with different temperatures from 300 K to 8 K. The Raman spectra are offset for clarity. The dashed lines represent a fit of phonon modes together with a background.

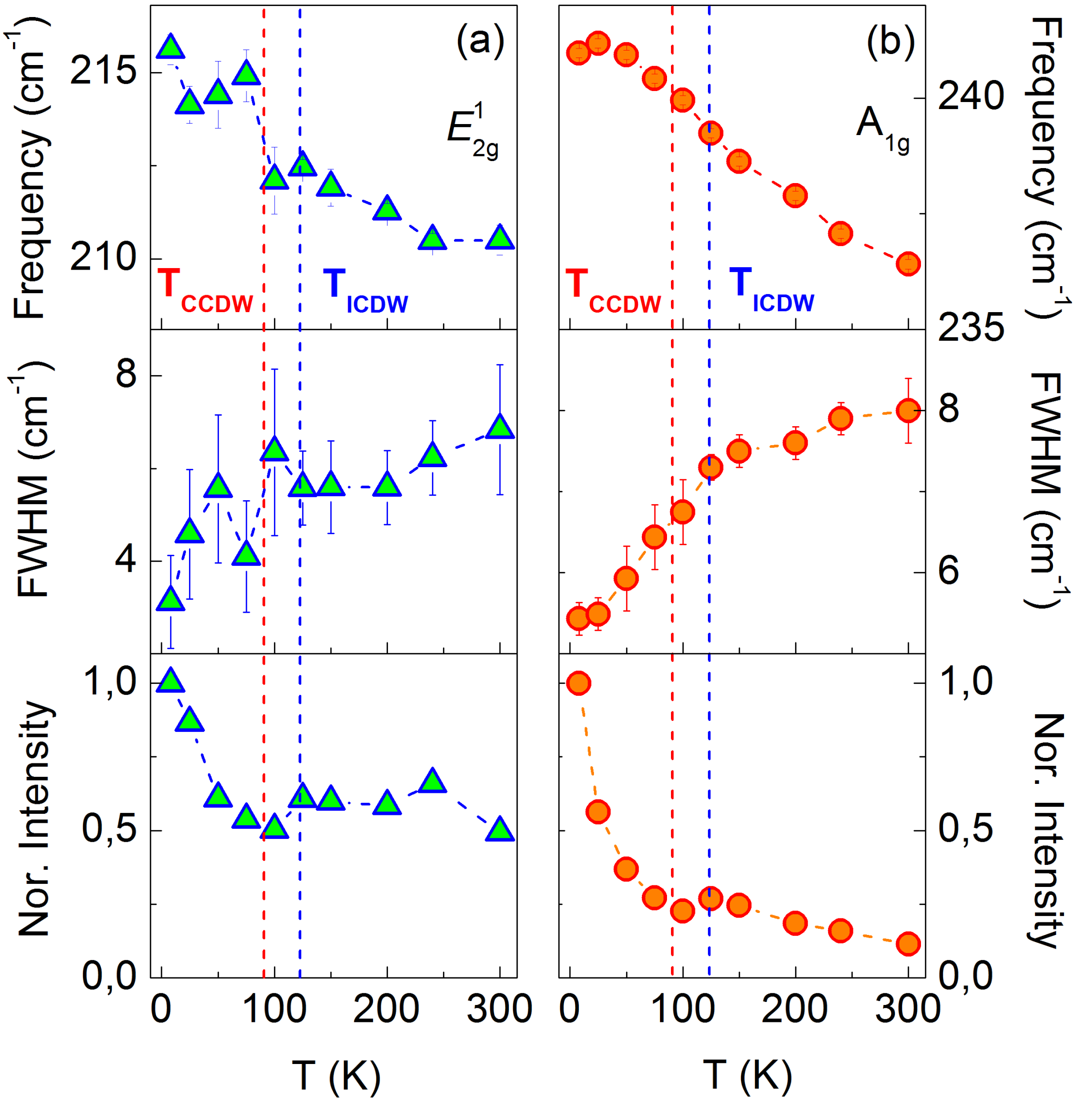

Figure 3.13: Temperature dependence of the frequency, the linewidth and intensity of TaSe$_2$ phonons for (a) E^1_{2g} and (b) A$_{1g}$ intrinsic modes, respectively. The dashed lines denote the incommensurate CDW and commensurate phase transition temperatures T$_{ICDW}$ = 123 K and T$_{CCDW}$ = 90 K, respectively. The phonon intensities were corrected by the Bose factor.

temperature dependence of the FWHM. In contrast, the E′ (Pb - Pb) mode exhibits a large width and a step-like decrease of the FWHM between 100 and 150 K (see Fig. 3.14a). At the respective temperature, the integrated intensity increases steeply. The same trend is visible for the E′ and A′ mode as well. Furthermore, we would like to draw attention to the temperature dependence of the background scattering. As evident from figure 3.15b, the background signal decreases substantially for temperatures below 150 K. Most probably, the background response originates from light scattering of electrons by Pb defects.

Combining the above findings, it seems that the charge dynamics of the hybrid Pb and $TaSe_2$ layers is different from that of the pure $TaSe_2$ layers. Topologically protected materials show coherent surface states at low temperatures whereas incoherent dynamics becomes dominant due to thermally excited phonons at high temperatures [34]. In our case, phonons mediate the Pb and $TaSe_2$ layers, thereby changing the charge dynamics upon heating. This may explain the appearance of the background scattering by Pb defects and phonons at high temperatures and the phonon anomalies of the E′ (Pb-Pb) mode.

3.1.7 Resonance Effects

We performed resonance Raman scattering measurements with six different laser wavelengths on $PbTaSe_2$. Respective data and analysis of the intensity are shown in Fig. 3.16a and 3.16b. A resonance effect of the Raman intensity is expected if the incident photon energy matches the energy of respective electronic transitions. In $PbTaSe_2$ the phonon modes indeed show a strong resonance effect in intensity with a maximum at 568 nm (2.18 eV). A sharp minimum is observed at 647 nm (1.92 eV). The largest magnitude of the resonance effect has the E′ (Pb - Pb mode) line, for instance $I_{568}/I_{532} \approx 5$, whereas for the A′ mode and for the * modes this intensity ratio is $I_{568}/I_{532} \approx 3.3$. Lone-pair *p* electron states of Pb with their

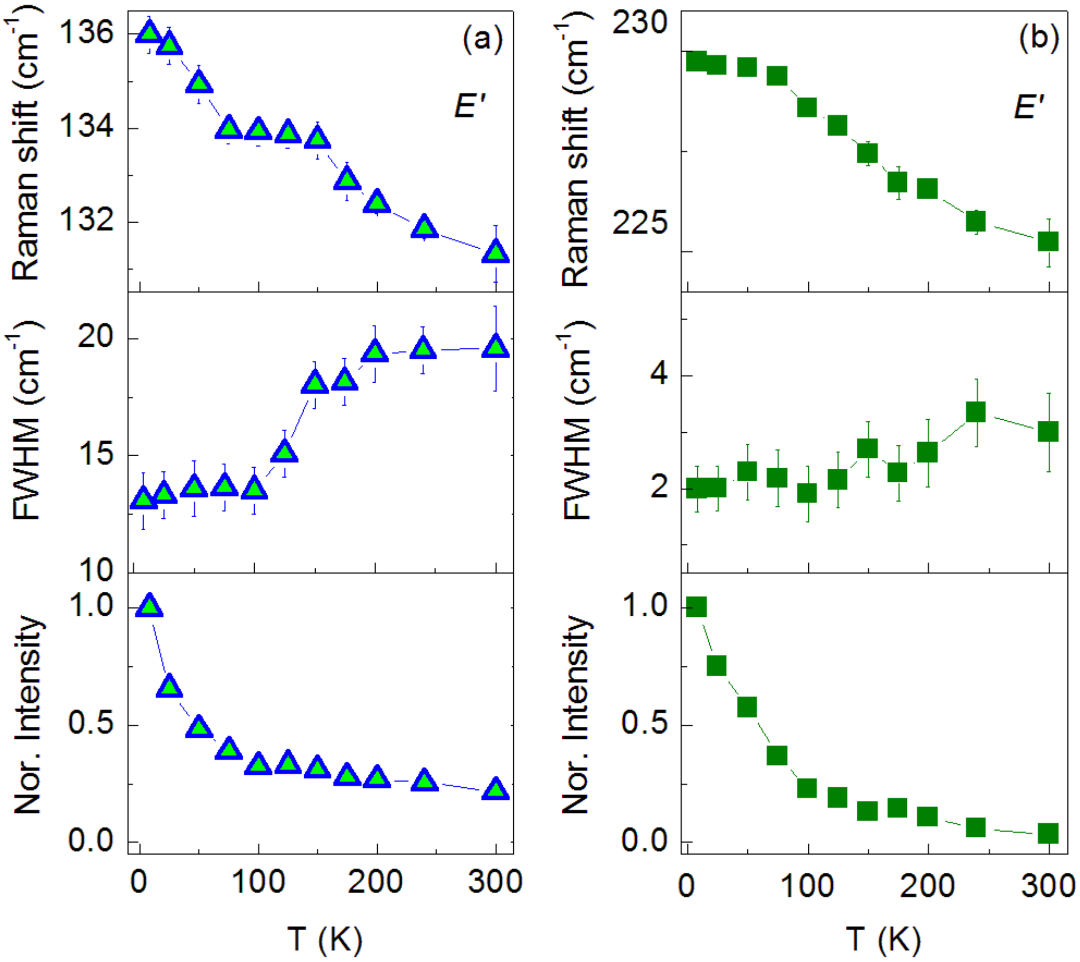

Figure 3.14: Temperature dependence of the frequency, the linewidth and intensity of $PbTaSe_2$ for (a) E′ (Pb-Pb) mode at 136 cm^{-1} and (b) E′ mode at 230 cm^{-1}, respectively. The phonon intensities were corrected by the Bose factor.

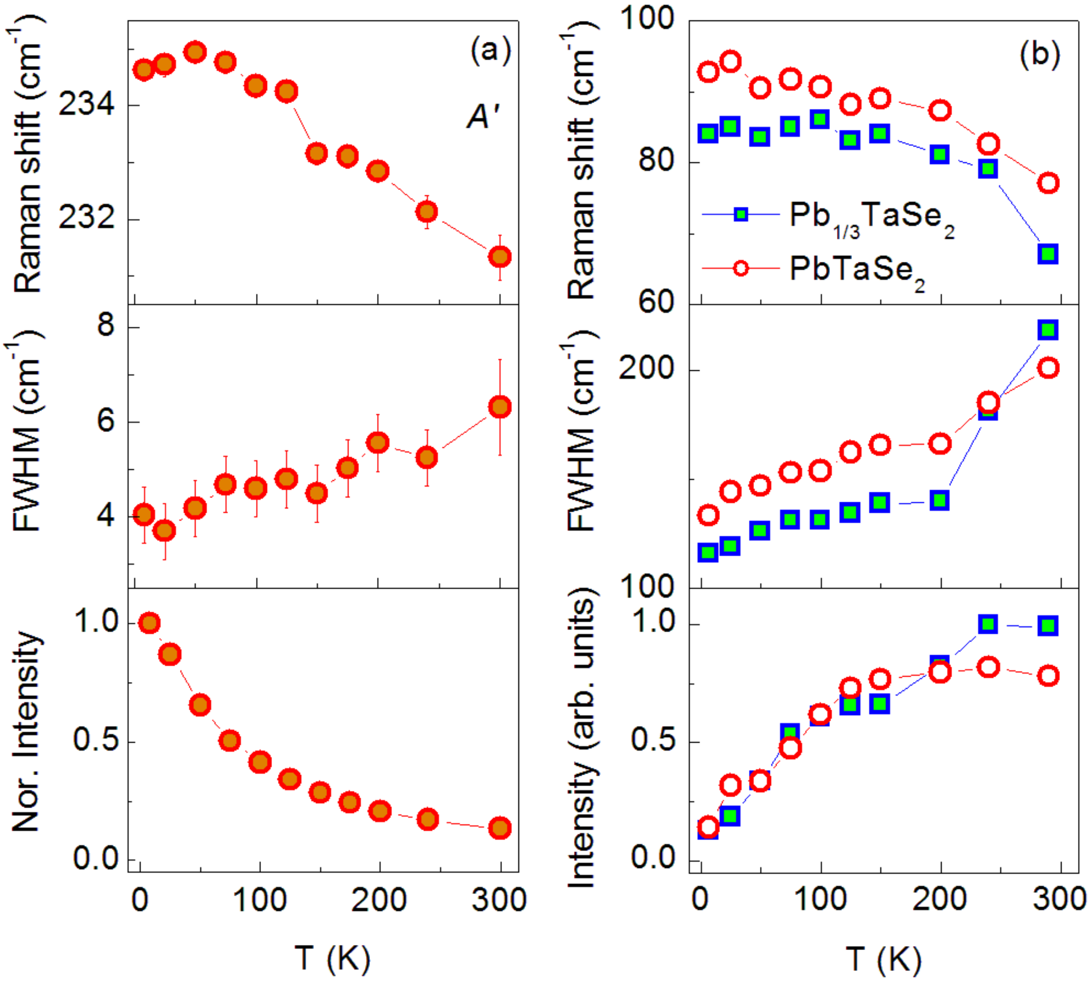

Figure 3.15: Temperature dependence of the frequency, the linewidth and intensity of $PbTaSe_2$ for (a) A′ mode and (b) the background signal. The phonon intensities were corrected by the Bose factor but the background intensity consists of raw data.

high polarizability are a possible reason for this enhancement.

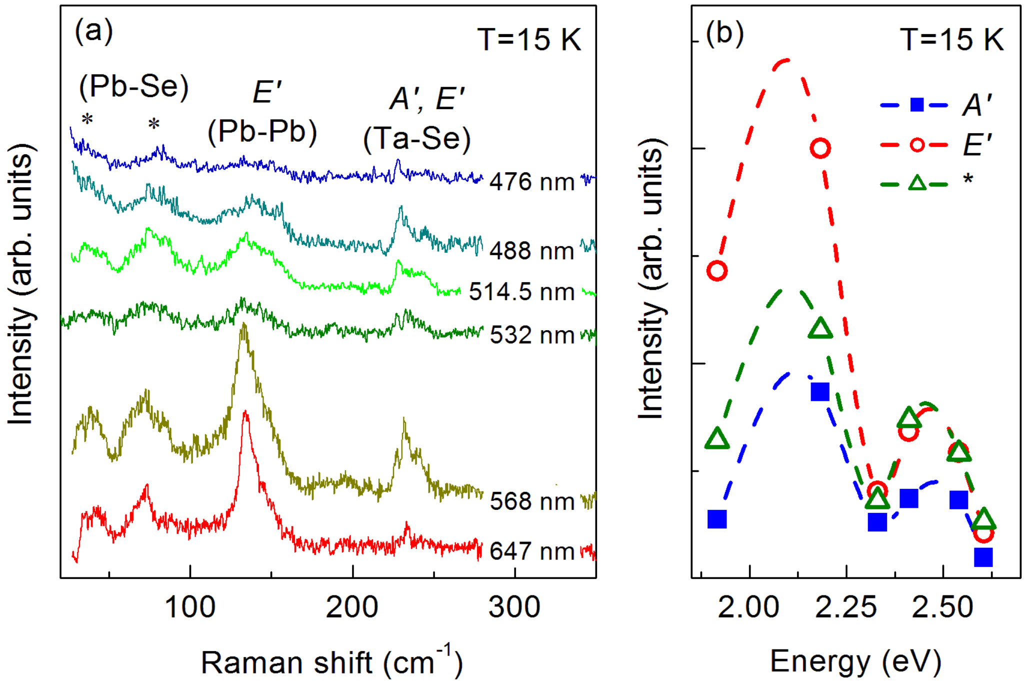

Figure 3.16: (a) Raman spectra of PbTaSe$_2$ with different incident laser excitations measured in (xx) polarization and at T = 15 K. (b) Laser wavelength dependence of the intensity of the E′, A′ and * modes. The asterisks denote phonon modes related to PbSe nanocrystals. The symbols denote experimental points and the broken curves represent B-spline fit drawn to guide the eye.

In Fig. 3.17 polarization dependent Raman spectra of PbTaSe$_2$ are shown. The A′ out-of-plane vibrational mode is suppressed in crossed (xy) polarization, while the E′ in-plane vibrational mode remains unaltered as expected from the selection rules. The broad mode at ~ 40 cm^{-1} exhibits little polarization dependence, whereas the other two broad modes around 80 and 130 cm^{-1} show sizable changes. However, we cannot identify apparent selection rules of the low-energy broad peaks. This indicates that they are related to disorders or defects induced by Pb intercalation. This effect will be described in details further below.

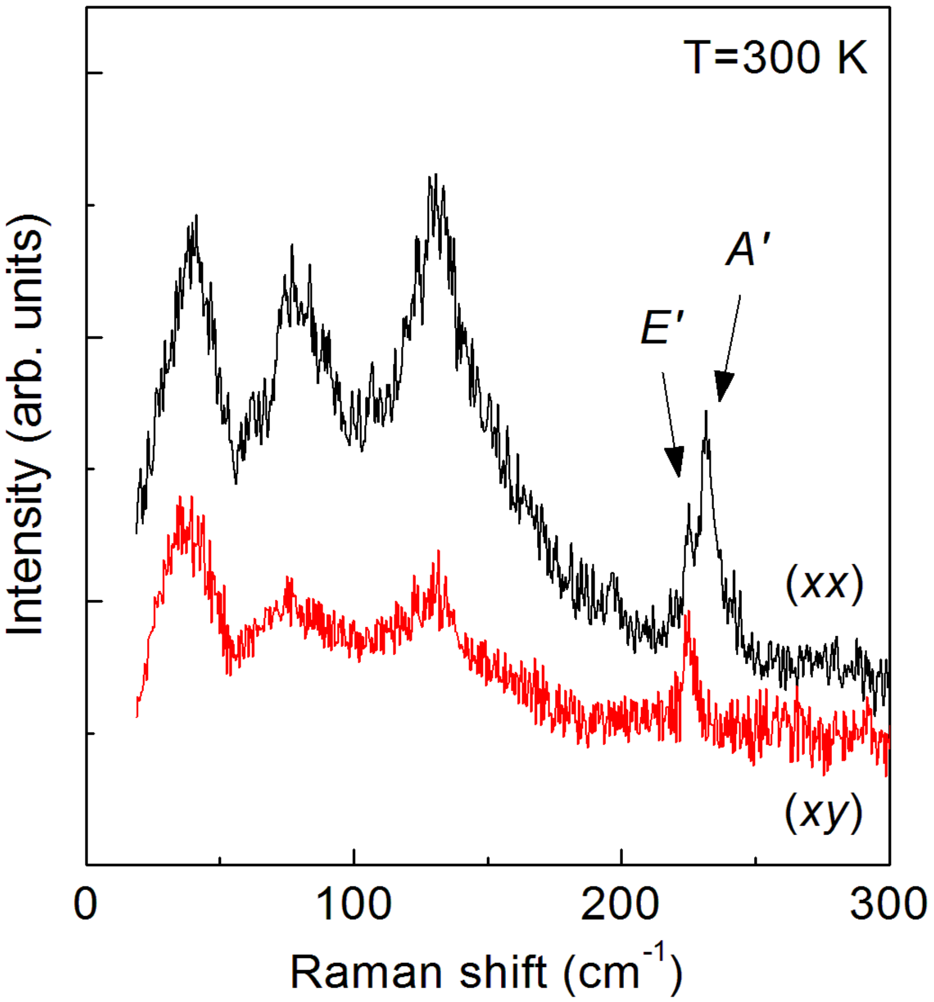

Figure 3.17: Polarization dependence of Raman spectra of $PbTaSe_2$ at T = 300 K in (xx) and (xy) polarizations.

3.1.8 Discussion

In the first part of the discussion the relation of properties such as thickness of $TaSe_2$ layered compound, Pb concentration in Pb_xTaSe_2 and the covalency of the Ta - Se bond will be considered and related to interlayer and intralayer interactions and their effect on the phonon frequencies. In the second part we consider different possible origins for the low-frequency broad modes, which appear upon Pb intercalation into $TaSe_2$. We assume that such phenomena could be related to the remnants of CDW phase in the Pb doped compounds or induced disorder and defects or the formation of PbSe nanocrystals.

For atomically thin, exfoliated layers of $TaSe_2$ and MoS_2 a 3 % hardening of the E_{2g} modes and a very weak softening of the A_{1g} have been observed with decreasing thickness. The latter corresponds to a decreasing number of unit cells [26, 35]. In a classical model of coupled harmonic oscillators, however, a hardening of phonon modes is expected only with increasing coupling. The opposite effect in the experiments points to an additional interaction which is supposed to be a long range Coulomb interaction from a charge transfer between the layers.

This apparent contradiction also exists for Pb_xTaSe_2 with an even more pronounced 10% hardening of the E_{2g} phonon with increasing Pb concentration. The geometric changes of Pb_xTaSe_2 with increasing x can be summarized as an increase of the layer distance, its thickness, the distance between Ta and Se atoms and the Se-Ta-Se angle. We assume that they reflect a change in the electronic configuration and bonding induced by Pb intercalation and, in their turn, induced charge in the layer. The formal oxidation states of Ta and Se in $TaSe_2$ is +4 and -2. With full Pb intercalation the Ta valence changes to +2. This reduction reduces ionic interactions and increases covalent bonding contributions. The Ta-Se interaction shows bigger effect, while the Se - Se mode is largely unchanged. The insensitivity of the A_{1g} mode to the Pb intercalation may be due to the fact that van der Waals (VdW) and long range Coulomb interactions are compensated by charge dynamics. It is interesting to note that such interplay of long range Coulomb interactions between chalcogen atoms and metals together with VdW forces are also discussed for GaS [36] and GaSe [37].

In the following we will focus on doped Pb_xTaSe_2 samples and broad modes at low frequencies. Firstly, we propose that after intercalation of Pb layer between Ta - Se layers, the CDW modes could remain afterwards. In Fig. 3.12 one can see that the frequencies of the two highly intense CDW modes from $TaSe_2$ are similar to the ones in Pb_xTaSe_2 (at about 40 and 80 cm^{-1}). Nevertheless, resistivity measurements [24] unveil the absence of CDW in the compound. Similar investigations were done also for copper intercalated superconductor Cu_xTiSe_2. Titanium diselenide is a CDW material with T_{cdw} = 200 K and upon Cu doping this compound becomes superconducting with T_c = 4.15 K [38]. A Raman scattering study shows that the E_g and A_{1g} CDW amplitude modes are heavily suppressed with concentration of Cu of 5 % and the CDW phase is not present anymore.

Albeit, there are cases where the phase transition temperature of a CDW state increases with certain doping. This is the case for $IrTe_{2-x}Se_x$ [39]. Also, it is worth to mention that the change of the Ta oxidation state to +2 introducing two electrons to Pb_xTaSe_2 may also lead to some sort of phase separation or charge modulation. Such a short range order assumes a partial localization of these states that are not available for transport. Further studies are needed to clarify this situation and to evaluate whether these states play a role in enhancing the superconducting transition temperature.

In this paragraph we discuss arguments against a residual CDW in the doped samples. We focus on the broad feature around 130 cm^{-1} consisting of a broad mode and superimposed sharp mode (Pb-Pb interaction [40]). Very likely, the broad mode could be assigned to a second-order Raman process since a similar peak is observed in $TaSe_2$. In accordance to Raman measurements of transition metal dichalogenides, the 2-phonon Raman mode has different temperature dependence in comparison with PbTaSe$_2$ [27]. Normally, 2-phonon Raman scattering is strongly suppressed with decreasing temperatures and the peak shifts towards lower energies. This process is distinctive for CDW-type materials, such as TaSe$_2$ and NbSe$_2$ [41]. Nevertheless, in PbTaSe$_2$ the behaviour of the broad mode is different compared to the usual 2-phonon mode in transition metal dichalcogenides. In our case, the broad mode at ~ 130 cm^{-1} in PbTaSe$_2$ is not suppressed at low temperatures. Such behaviour is incompatible with a CDW scenario.

A second possible explanation for the broad modes at 40, 80 and 135 cm^{-1} is related to a structural transition due to intercalation. Upon Pb doping, the crystal structure changes drastically. For instance, the layers of Ta and Se atoms in TaSe$_2$ form a "star" along the *c* axis and have an inversion centre (see Fig. 3.1). However, after intercalation of Pb atoms into the structure, such formation is triangular, leading to a non-centrosymmetric system having no more inversion centre. Due to this process, besides Ta - Se Raman modes, one could observe additional modes possibly from Pb - Pb or/and Pb - Se interaction.

There is another perspective related to a possible formation of Pb clusters. Spiro et al. [40] performed Raman measurements on $\mathrm{Pb_6O}(OH)_6^{4+}$ containing Pb clusters. They observed several modes related to Pb-Pb interactions. The Raman frequency of such interactions depends on the distance between Pb atoms. An intense and sharp peak at 150 cm^{-1} in $\mathrm{Pb_6O}(OH)_6^{4+}$ has been attributed to an interaction of Pb atoms at a distance of 3.44 Å, which is, in fact, anticipated distance between Pb atoms in PbTaSe$_2$. In this respect, the 130 cm^{-1} mode observed in PbTaSe$_2$ may be due to Pb-Pb clustering. As Pb atoms can have different positions in the clusters with a variation of distances, other broad modes could have the same origin. In $\mathrm{Pb_6O}(OH)_6^{4+}$ there also exist broader modes at low frequencies that superimpose sharper excitations [40].

The third reason for the appearance of these broad modes is provided by the formation of PbSe nanocrystals or Pb - Se bondings. The polarized Raman scattering experiments showed that the A′ and E′ vibrational modes follow the selection rules (Fig. 3.17). However, the additional broad modes have little difference between the (xx) and (xy) polarizations. When Pb atoms are inserted between the $TaSe_2$ layers, predominantly the Pb atoms form a Pb layer by Pb - Pb bonding. Nonetheless, it is possible that they form PbSe nanocrystals through Pb-Se bonding. Indeed, lead chalcogenides PbX (X = S, Se, or Te) are stable semiconductors and their Raman spectra are scattered between 30 and 130 cm^{-1} with second-order scattering observed at about 260 cm^{-1} [28, 29]. This accounts for the first-order peaks at 40, 80 and 135 cm^{-1} as well as the second-order peak 267 cm^{-1}, which are denoted by the asterisks in Fig. 3.10 and 3.16. Such scenario provides an explanation for their obscure polarization and temperature dependence distinctly different from the E′ (Pb - Pb) mode, E′ and A′ modes. Therefore, we conclude that doping $TaSe_2$ with Pb atoms forms a heterogeneous Pb - Se bonding in addition to the Pb layer.

3.1.9 Conclusion

To conclude, extensive Raman scattering experiments were done for Pb_xTaSe_2. The concentration dependence of Raman spectra showed a pronounced hardening of the in-plane E_{2g} mode with increasing Pb content, which is much larger than an effect observed in exfoliated crystals with different layer thickness. This can be taken as a signature of nontrivial coupling between Pb and $TaSe_2$ layers, which is responsible for structural and electronic changes. In addition, for the Pb doped compounds the temperature and polarization dependence of Raman spectra reveal three additional broad modes in the low frequency range, which behave differently from the symmetry-allowed Raman modes. Their origin is discussed in terms of PbSe nanocrystals or clusters formed at the interface between the Pb and $TaSe_2$ layers.

3.2 The 3D Dirac Semimetal Cd_3As_2

Three-dimensional topological semimetals are currently the subject of intensive studies in condensed matter physics. The unusual electronic structures which consist of relativistic bands, linear dispersion, non-trivial topologies, strong spin-orbit coupling and other prominent features make researchers eager to find new compounds possessing such properties. One of the representatives of such materials is Cd_3As_2, which is already known for many years [42, 43]. It was being studied due to its unusual transport properties, high electron mobility ($\approx 10^5$ $cm^2V^{-1}s^{-1}$) and semimetallic character (the conduction and valence bands "touch" at one specific location).

As afore said, it was well investigated but not in the context of recent findings of novel topological states. These studies show that there are two 3D Dirac nodes at two special k points along the G-Z momentum space direction [44, 45, 22]. In addition, in comparison with the well-studied 2D Dirac systems (e.g. topological insulators), the Fermi velocity of the 3D Dirac fermions is quite high ($\approx 2{\cdot}10^6$ $m{\cdot}s^{-1}$) [22]. It is thus about 3 times higher than in the topological surface states of Bi_2Se_3 [46] and 1.5 times higher than in graphene [47].

The existence of 3D Dirac fermions in Cd_3As_2 implies that it is a bulk counterpart of graphene [44]. There are also other 3D topological Dirac semimetals, such as A_3Bi (A = K, Rb, Na)[21] or β-cristobalite BiO_2 [48]. However, they are all unstable at ambient conditions. Furthermore, Cd_3As_2 also stands out due to its chemical stability.

A topological Dirac semimetal can also be driven into a Weyl semimetal phase, if there is broken time-reversal or space inversion symmetry [49]. This leads to a splitting of the Dirac points and the appearance of the special surface Fermi arcs. Furthermore, the presence or absence of the center of symmetry in Cd_3As_2 is a crucial parameter which will affect the electronic structure [11]. Therefore, experimental prove of the right crystal structure for Cd_3As_2 is very important and it might help to resolve the disputes concerning the inversion center.

3.2.1 Crystal Structure

The crystal structure of Cd_3As_2 can belong to two possible space groups $I4_1$cd and $I4_1$acd, i.e. non-centrosymmetric or centrosymmetric, respectively [22, 11]. Our task is to determine which of them is most probable and check phonon modes of our compound of interest. Resolving the ambiguity between a centrosymmetric crystal structure and a noncentrosymmetric can sometimes be difficult, and this is a well-known problem in crystallography [50, 51], so it would be good to find it out with a help of Raman scattering experiments.

The structure of Cd_3As_2 has a lot of ordered vacancies and its unit cell is quite big ($a = b = 12.633(3)$ Å, $c = 25.427(7)$ Å) [11]. Cadmium arsenide has also various though related crystal structures depending on temperature (Fig. 3.18). All of them can be attributed to defect antifluorite types of structure. Moreover, the ideal antifluorite formula would be Cd_4As_2, which in turn reveals us the Cd-deficient Cd_3As_2. In this case the compound lacks two out of eight Cd atoms variants. Furthermore, they tend to displace from the initial antifluorite positions in the direction of the empty vacancies.

Irreducible representation of allowed Raman modes for the noncentrosymmetric structure is $\Gamma = 26A_1 + 27B_1 + 27B_2 + 65E$ and for the centrosymmetric structure is $\Gamma = 14A_{1g} + 14B_{1g} + 15B_{2g} + 31E_g$.

The corresponding Raman tensors to the space group $I4_1$cd (No. 110) are [8]:

$$A_1 = \begin{pmatrix} a & 0 & 0 \\ 0 & a & 0 \\ 0 & 0 & b \end{pmatrix}, \quad B_1 = \begin{pmatrix} c & 0 & 0 \\ 0 & -c & 0 \\ 0 & 0 & 0 \end{pmatrix}, \quad B_2 = \begin{pmatrix} 0 & d & 0 \\ d & 0 & 0 \\ 0 & 0 & 0 \end{pmatrix},$$

$$E(x) = \begin{pmatrix} 0 & 0 & e \\ 0 & 0 & 0 \\ e & 0 & 0 \end{pmatrix}, \quad E(y) = \begin{pmatrix} 0 & 0 & 0 \\ 0 & 0 & e \\ 0 & e & 0 \end{pmatrix}.$$

Whereas the corresponding Raman tensors for centrosymmetric space group $I4_1$acd (No. 142) are [8]:

$$A_{1g} = \begin{pmatrix} a & 0 & 0 \\ 0 & a & 0 \\ 0 & 0 & b \end{pmatrix}, \quad B_{1g} = \begin{pmatrix} c & 0 & 0 \\ 0 & -c & 0 \\ 0 & 0 & 0 \end{pmatrix}, \quad B_{2g} = \begin{pmatrix} 0 & d & 0 \\ d & 0 & 0 \\ 0 & 0 & 0 \end{pmatrix},$$

$$E_g = \begin{pmatrix} 0 & 0 & -e \\ 0 & 0 & e \\ -e & e & 0 \end{pmatrix}.$$

The measurements of Cd_3As_2 were done on a natural cleavage plane with {112} orientation. We expect for this plane a total number of 145 (space group $I4_1$cd) or 74 (space group $I4_1$acd) modes for every polarisation configuration. We assume that there is a mixing of the symmetry assignments. It leads to interplay of intensities of the phonon modes. Furthermore, not every mode is observed in every polarisation configuration. Some intensities would be very weak and therefore we would not observe them.

3.2.2 Electronic and Magnetic Properties

Theory predicted that Cd_3As_2 has a special electronic structure, where two touching points (red crosses in Fig. 3.19a) of 3D Dirac bands along k_z direction of BZ are expected [52]. The schematic view for better visualization of such bands is given in Fig. 3.19b.

Indeed, high resolution angle-resolved photoemission spectroscopy (ARPES) allowed to discover a pair of bulk Dirac fermions near the centre of BZ [44]. The photoemission experiments revealed the band structure of Cd_3As_2 along the $\overline{M}$-$\overline{\Gamma}$-$\overline{M}$ direction with the photon polarization parallel to this direction (see Fig. 3.20a). They also yield linear dispersion of the 3D Dirac fermions

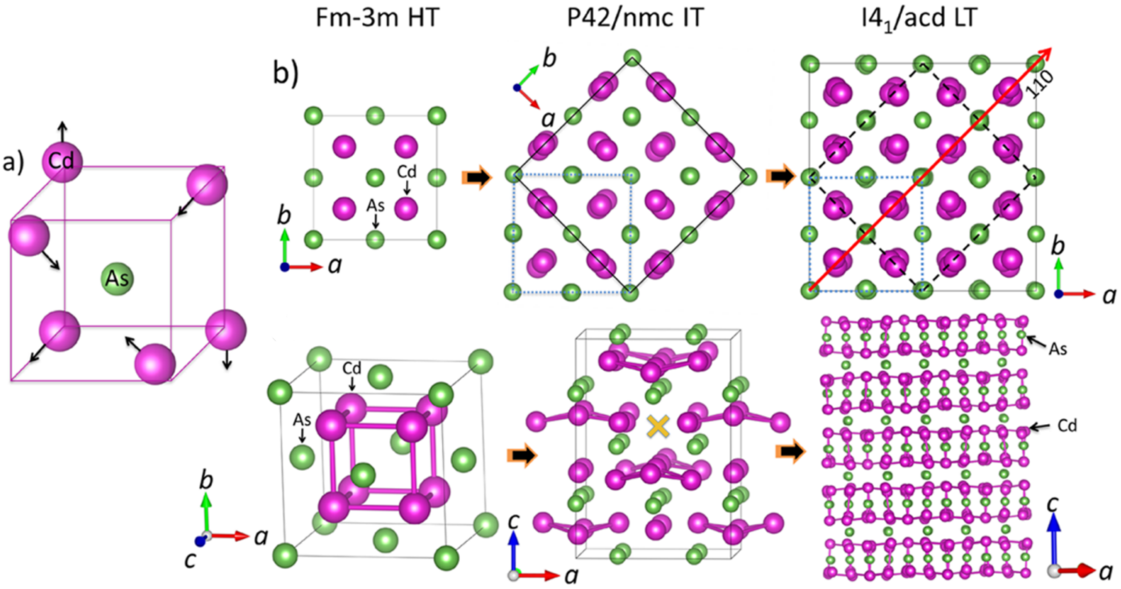

Figure 3.18: Evolution of the crystal structure of Cd_3As_2 with lowering the temperature. (a) Cd-As cube with the Cd atoms distorted in the direction of Cd vacancies. (b) Different crystal structures as a function of temperature. From left to right, the high temperature (HT) $Fm\overline{3}m$ structure, the intermediate temperature (IT) $P4_2/nmc$ structure and the low temperature (LT) $I4_1$acd structure (ref) [11].

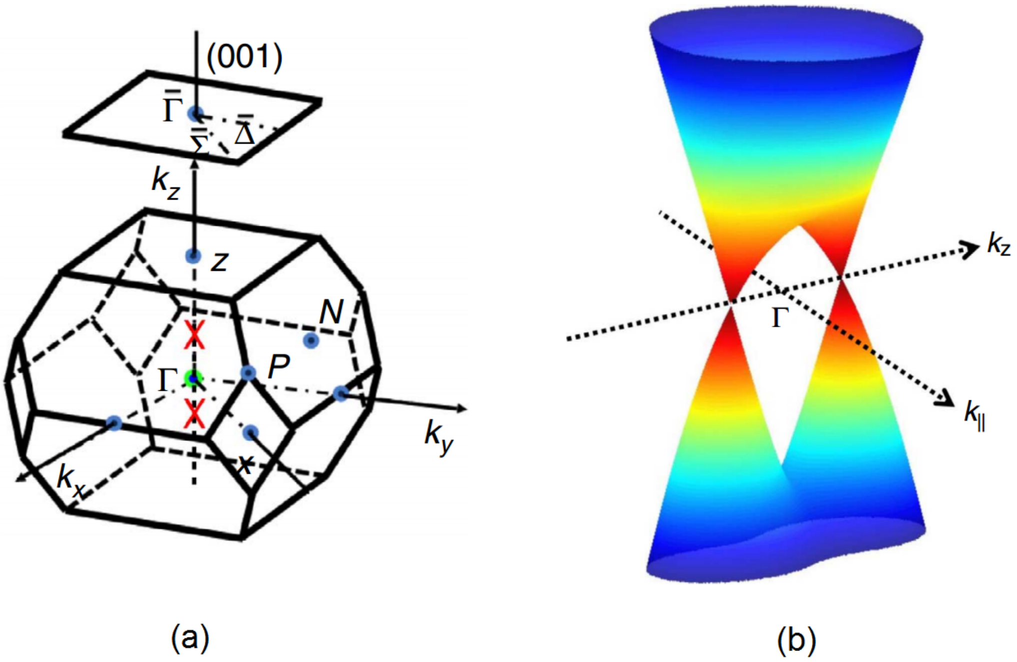

Figure 3.19: (a) The 3D BZ and the projected (001) surface of Cd_3As_2. The red crossings state for two special Dirac points along G-Z direction. (b) Schematic view of 3D Dirac linear dispersions in Cd_3As_2 [22].

and the so-called Dirac cone which is plotted using the experimental findings in Fig. 3.20b.

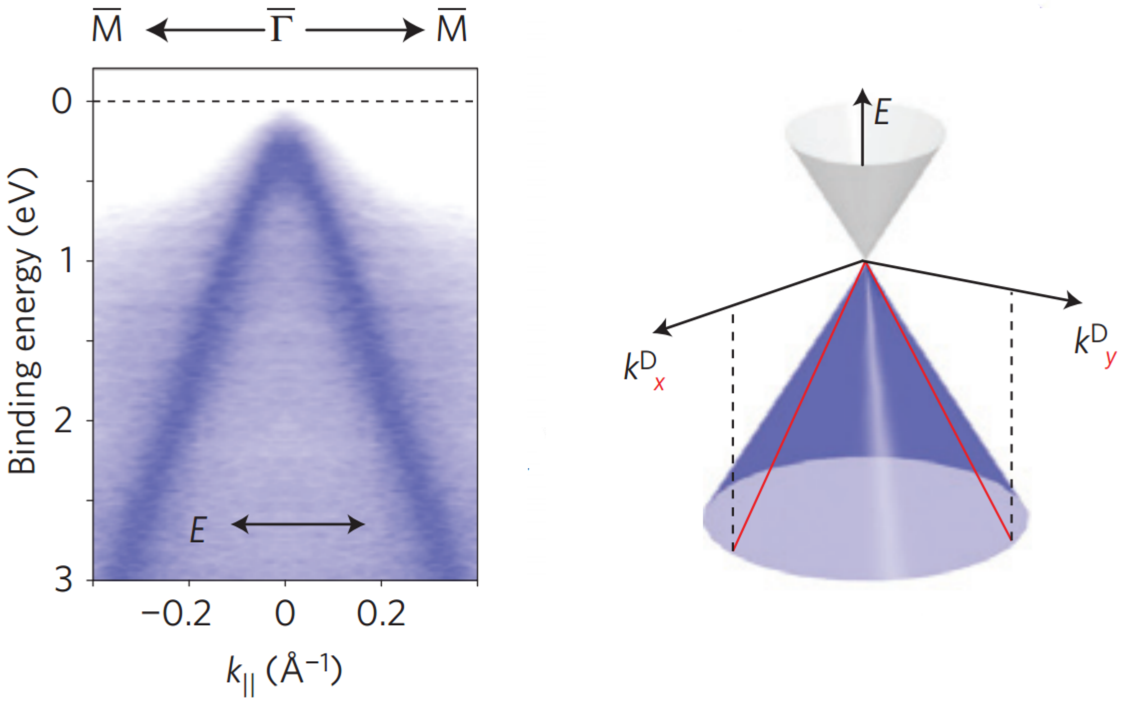

(a)

(b)

Figure 3.20: (a) Experimental data of band dispersion from ARPES measurements with photons polarized along G-M direction. (b) Dirac cone plotted out of the experimental parameters [44].

In addition to ARPES, transport measurements also allow to probe the unusual electronic structure of 3D Dirac semimetals. A characteristic linear magnetoresistance (MR) was observed in various Dirac materials, like multilayered graphene [53] and topological insulators [54, 55, 56]. Theoreticians were also expecting linear MR for Cd_3As_2, even up to room temperature [52]. The longitudinal resistivity ρ_{xx} without magnetic field was measured as a function of temperature and can be seen in Fig. 3.21a. Cd_3As_2 has a metallic character and revealed a residual resistivity $\rho_{xx0} \approx$

28.2 $\mu\Omega cm$. Further, the magnetic field dependence of the Hall resistance R_{xy} at different temperatures were obtained and it shown in Fig. 3.21b. The main charge carriers are electrons, since the slope of R_{xy} is negative and the concentration of current carriers $n_e \approx 5.3 \cdot 10^{18}$ cm^{-1}. The low concentration and high mobility of electrons are the characteristic features of Cd_3As_2 [45, 22]. At the same time, there are distinctive oscillations of R_{xy} at the lowest temperature T = 1.5 K. Moreover, in Fig. 3.21c they observe even larger Shubnikov-de Haas oscillations. The magnetoresistance is obtained by using this formula: MR = [R_{xx}(B)-R_{xx}(0 T)]/R_{xx}(0 T) $\cdot$ 100%. Amazingly, such large magnetoresistance becomes linear as room temperature is reached. Such unusual behaviour would be useful for future applications in magnetic sensors and magnetic memory devices.

Moreover, infrared measurements were recently done and they reveal interband transitions between two Dirac bands with a sublinear dispersion relation [58]. In addition, our interest in these experiments are the phonon modes (see Fig. 3.22). They will be useful in determination the right crystal structure by comparing the phonon modes in IR and Raman measurements.

3.2.3 Experimental Details

Single crystals of Cd_3As_2 with dimensions of 2 mm^3 were grown by self-selecting vapour growth (SSVG) method. The investigated shiny and black surface of the crystals had a triangle shape which corresponds to {112} plane. Raman scattering measurements were performed on single crystals of Cd_3As_2 in quasi-backscattering geometry. Light scattering polarizations are given by parallel (xx) and crossed (yx) polarizations within the crystallographic ab plane. Incident light was polarized perpendicular to the base of the triangle. Samples were cleaned with acetone and isopropanol. Afterwards, they were glued to the sample holder with a silver glue to get better conductivity in the temperature dependent measurements.

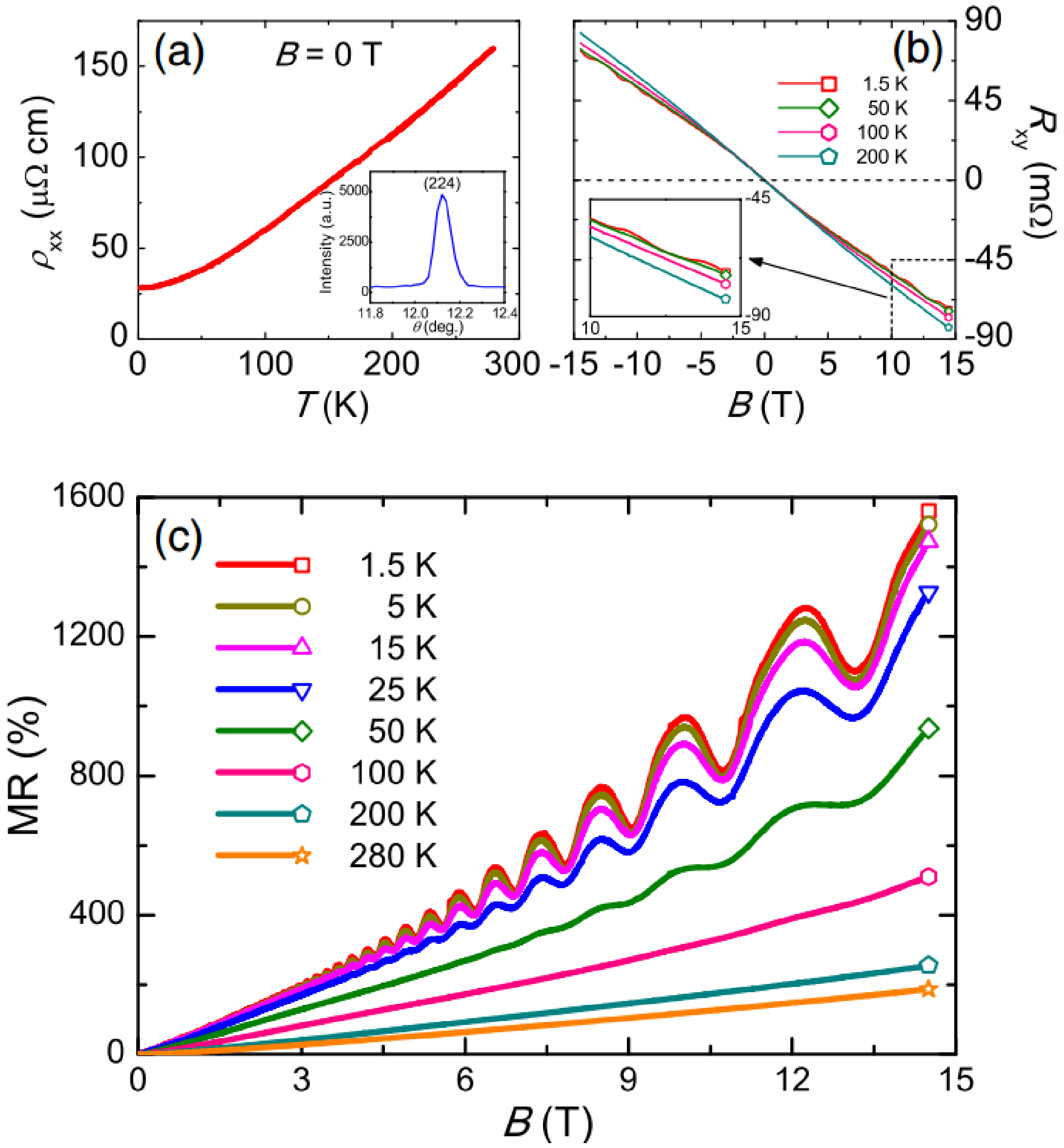

Figure 3.21: (a) The temperature dependence of longitudinal resistivity without a magnetic field. The inset shows an X-ray rocking curve of the Bragg peak, confirming the good quality of the crystal. (b) The Hall resistance at different temperatures. Inset shows the distinctive oscillations at 1.5 K. (c) The magnetic field dependence of the longitudinal resistivity at different temperatures [57].

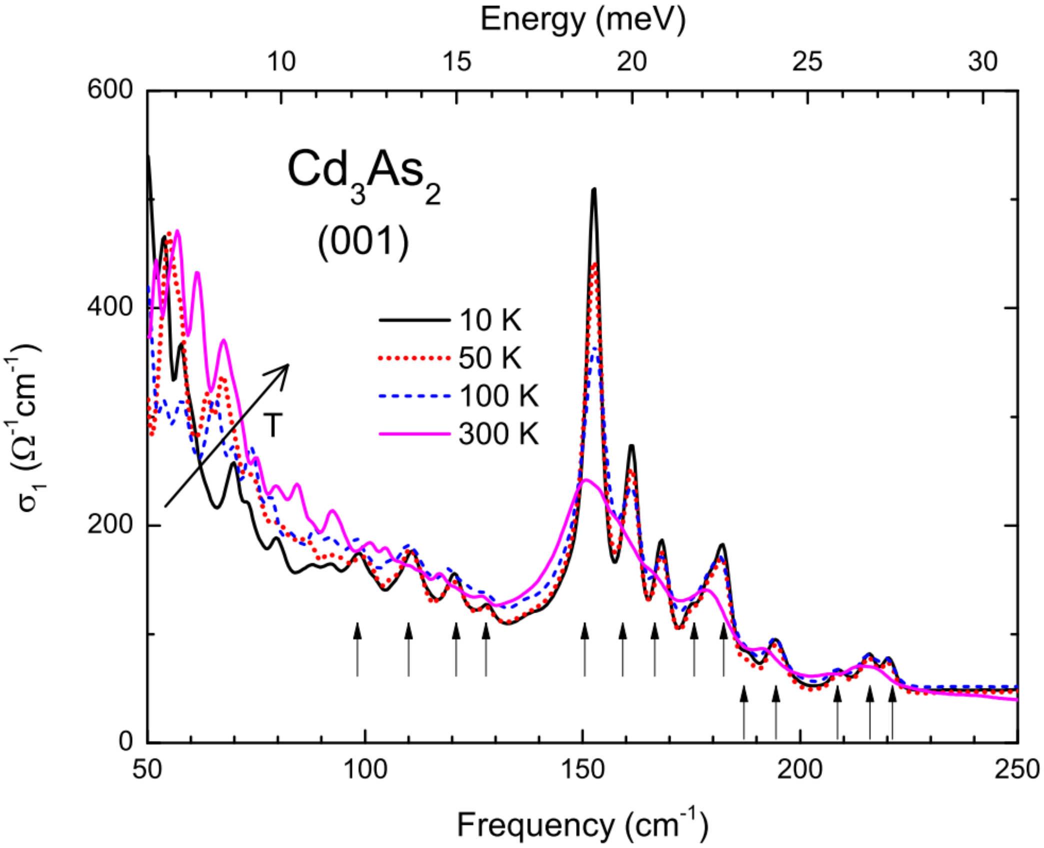

Figure 3.22: Optical conductivity of Cd_3As_2 at various temperatures. Arrows denote the phonon modes [58].

Temperature was varied from 9 K up to 300 K using a closed-cycle cryostat.
As an incident laser excitation the λ= 532 nm and 488 nm solid state lasers and an Ar-Kr-ion multiline gas laser (λ= 488 nm, 514.5 nm, 568 nm, and 647 nm) were used. The laser spot diameter is approximately 100μm. The samples of Cd_3As_2 were mounted on a sample holder and kept in vacuum. The six different laser lines allowed to probe effects of resonance Raman scattering.
The Raman spectra were collected using a triple Raman spectrometer (Dilor-XY-500) with an attached liquid-nitrogen-cooled CCD (Spectrum One CCD-3000V).

3.2.4 Properties of the Phonon Spectrum

Previous Raman scattering measurements (see Fig. 3.23) did not allow to analyse phonon modes due to strong quasielastic scattering on free charge carriers or defects [59].

In Fig. 3.24 the low temperature Raman spectra of Cd_3As_2 in different polarizations are shown. In comparison with previous Raman data [59], we observe numerous and sharp phonon lines. The spectra can be divided into two parts: first one consists of phonon modes from 20 to 90 cm^{-1} and second one from 150 to 230 cm^{-1}. They could be related to Cd-Cd and As-As interactions, respectively. Also, the spectra differ with respect to polarization configurations, besides different intensities we observe a lower number of modes in yx polarization (30 modes) in contrast to xx polarisation (40 modes).

Table 3.2: Table of the phonon modes of Cd_3As_2.

ω (cm^{-1})	XX	YX	Assignment	ω (cm^{-1})	XX	YX	Assignment
27.4	+++	+	B_{1g}	155	++	+	B_{2g}
31.2	+++	-	A_{1g}	157.21	+	+	B_{2g}
35.6	+	-	A_{1g}	160.1	+	-	A_{1g}
39.3	++	+	B_{2g}	166.4	+++	+	B_{1g}
46.7	+	++	E_g	172.2	+	-	A_{1g}
48.3	+	+	B_{2g}	174.7	+++	+	B_{1g}
53.9	++	+	B_{2g}	177.8	+	-	A_{1g}
56	+++	+	B_{1g}	181.4	+	++	E_g
59.9	-	+	E_g	187.5	+++	+	B_{1g}
61.5	+	-	A_{1g}	190.4	+++	+	B_{1g}
63.6	+	++	E_g	191.6	++	+	B_{2g}
66.8	+++	+	B_{1g}	193.6	+++	+	B_{1g}
70.8	+	-	A_{1g}	196.4	+++	+	B_{1g}
72.8	+++	+	B_{1g}	199.2	+++	+	B_{1g}
76.3	+	++	E_g	201	+++	+	B_{1g}
77.6	+	++	E_g	204.1	-	+	E_g
98.7	+	++	E_g	206.3	+++	+	B_{1g}
114.2	+	-	A_{1g}	209.6	+	-	A_{1g}
121.7	+	-	A_{1g}	218.9	+	-	A_{1g}
126.8	+	+	B_{2g}	220.2	-	+	E_g
140	+	-	A_{1g}	220.8	-	+	E_g
147.4	+	-	A_{1g}	221.8	+	-	A_{1g}

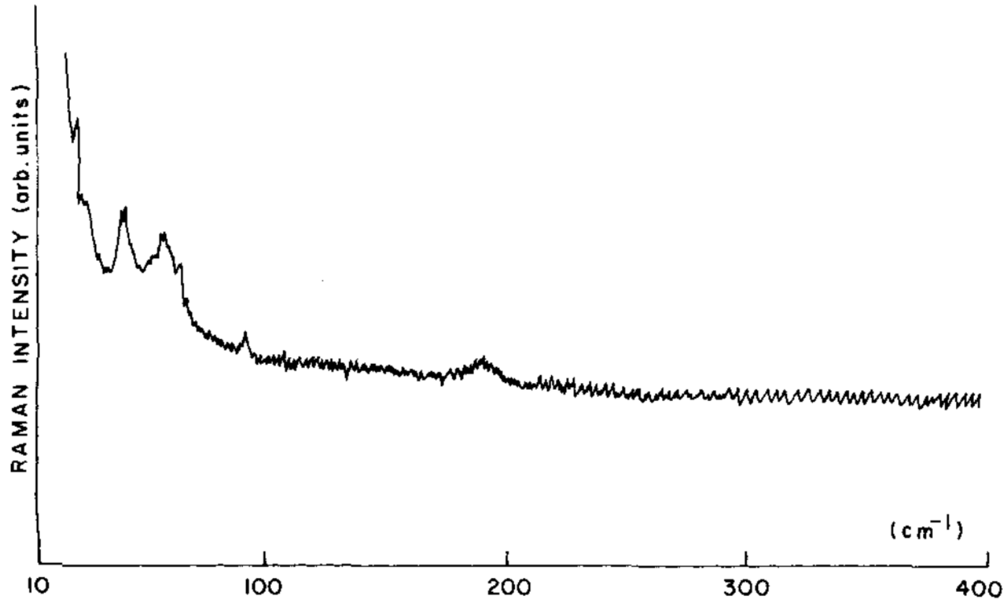

Figure 3.23: Unpolarized Raman spectrum of Cd$_3$As$_2$ at room temperature [59].

At low temperatures at 647 nm wavelength the spectra of Cd$_3$As$_2$ show narrow and intensive phonon modes. At xx polarisation we have observed 40 modes, whereas at yx we have observed only 30 modes. Such number of observed modes gives us a hint that the structure of Cd$_3$As$_2$ is centrosymmetric since for the corresponding space group ($I4_1$acd) we would have the least number of the Raman allowed phonon modes. The detailed list of the phonon modes at 647 nm and T = 9.5 K is given in Table 3.2.

3.2.5 Resonance Effects

In Fig. 3.25 we plot laser energy dependent Raman spectra of Cd$_3$As$_2$ at 9.5 K and at xx polarization. Upon increasing laser energy up to 2.5 eV (488 nm), we observe an enhancement of the quasielastic scattering (inset to Fig. 3.25, the peak was fitted by Lorentzian). In contrast, the intensity of the phonons is strongly decreasing down to 2.5 eV (488 nm).

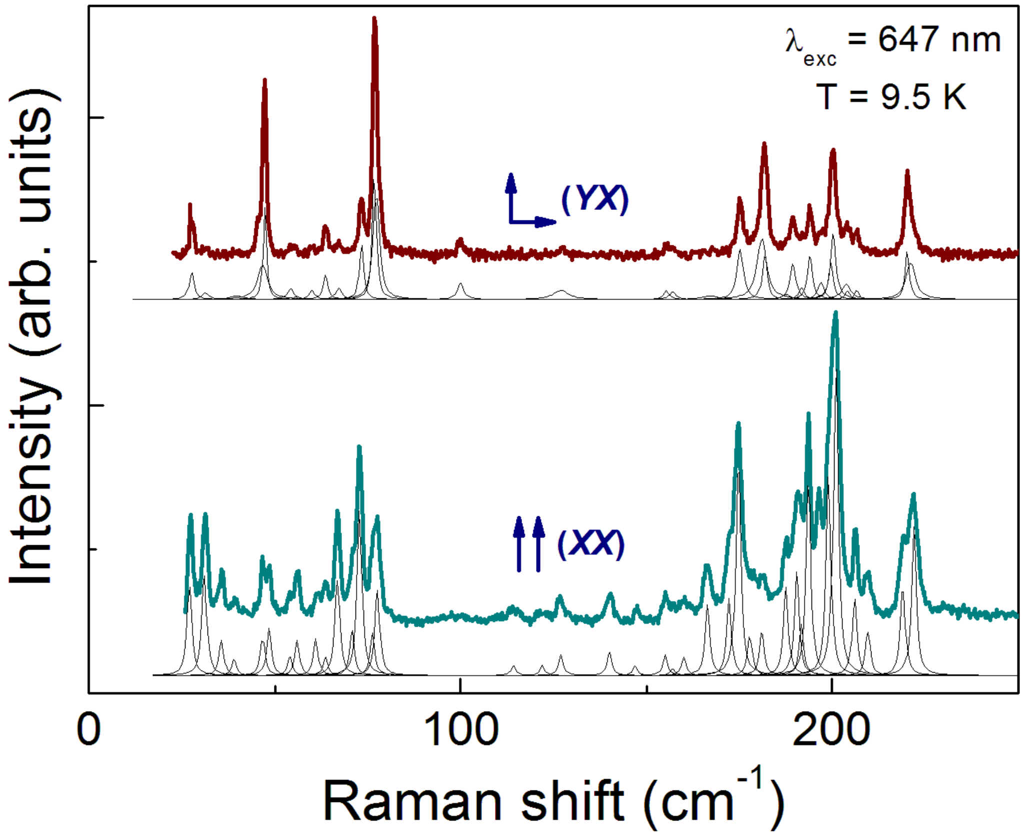

Figure 3.24: Low temperature Raman spectra of Cd_3As_2 at T = 9.5 K in (xx) and (xy) polarizations. Lorentzian peaks below the experimental curves are shown for convenience of the reader to differentiate phonon modes.

In addition, only for 647 nm and 568 nm laser lines at low temperatures we observe two-phonon scattering modes (360 - 440 cm^{-1}) from the second group of one-phonon modes (150 - 230 cm^{-1}).

In the following we will focus on experiments with 647 nm excitation as the intensity of the phonons is the largest compare to other excitation lines.

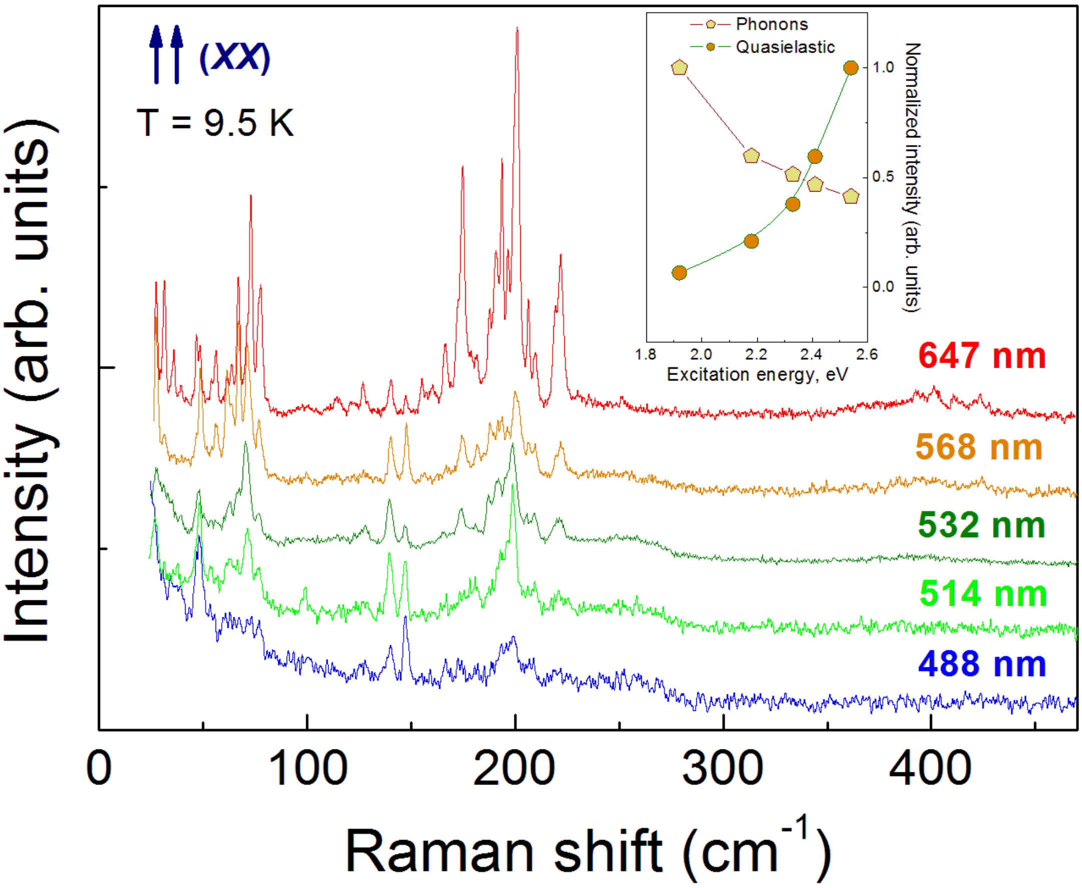

Figure 3.25: Raman spectra of Cd_3As_2 with different incident laser excitations measured in (xx) polarization and at T = 9.5 K. (inset) Laser wavelength dependence of the normalized intensity of the quasielastic scattering and phonons.

3.2.6 Temperature-induced Effects

The temperature dependent measurements for Cd_3As_2 were done in the range from 9.5 K up to room temperature and shown in Fig. 3.26. At lowest temperature the phonon modes are quite sharp and have the highest intensity in comparison with the room temperature data. Simultaneously, the intensity of the quasielastic scattering mode is decreasing with cooling. Due to such unusual behaviour we assume that there is a correlation between electron and phonon systems.

3.2.7 Discussion

The linewidth and Raman shifts of the phonon modes (46.5, 48.5, 67 and 73 cm^{-1}) for 647 nm at xx polarization are plotted in Fig. 3.27, 3.28 and they were analysed in the framework of an anharmonic model [60]:

$$\omega(T) = \omega_0 + C[1 + 2/(e^x - 1)] + D[1 + 3/(e^y - 1) + 3/(e^y - 1)^2]. \quad (3.1)$$

Here, $x = \hbar\omega_0/(2k_BT), y = \hbar\omega_0/(3k_BT)$, while C and D are constants. ω_0 is considered as the harmonic frequency of the mode at zero temperature. The linewidth was also analysed by this analogy:

$$\Gamma(T) = \Gamma_0 + A[1 + 2/(e^x - 1)] + B[1 + 3/(e^y - 1) + 3/(e^y - 1)^2]. \quad (3.2)$$

Here, Γ_0 is the linewidth at zero temperature, while A and B are constants. The red curves in Fig. 3.27 and 3.28 correspond to the results of such analysis. There is a deviation in phonon frequency and FWHM, especially for 67 and 73 cm^{-1} modes. The biggest effect of such deviation is at ~ 150 K (dashed line in Fig. 3.27 and 3.28). Such peculiarities in the phonon spectra are an evidence that

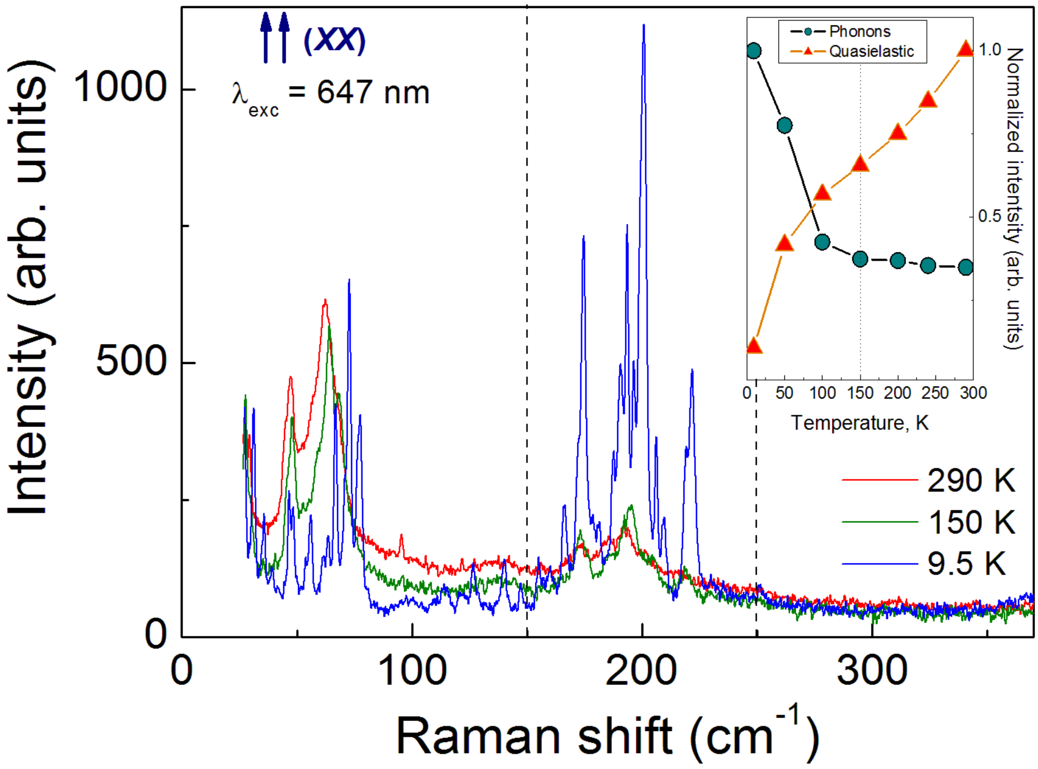

Figure 3.26: Raman spectra of Cd_3As_2 with different temperatures measured in (xx) polarization and at λ= 647 nm. (inset) Temperature dependence of the quasielastic scattering and phonon intensities (sum of the integrated intensity of the second group of phonon modes (150-250 cm^{-1}) with background correction.

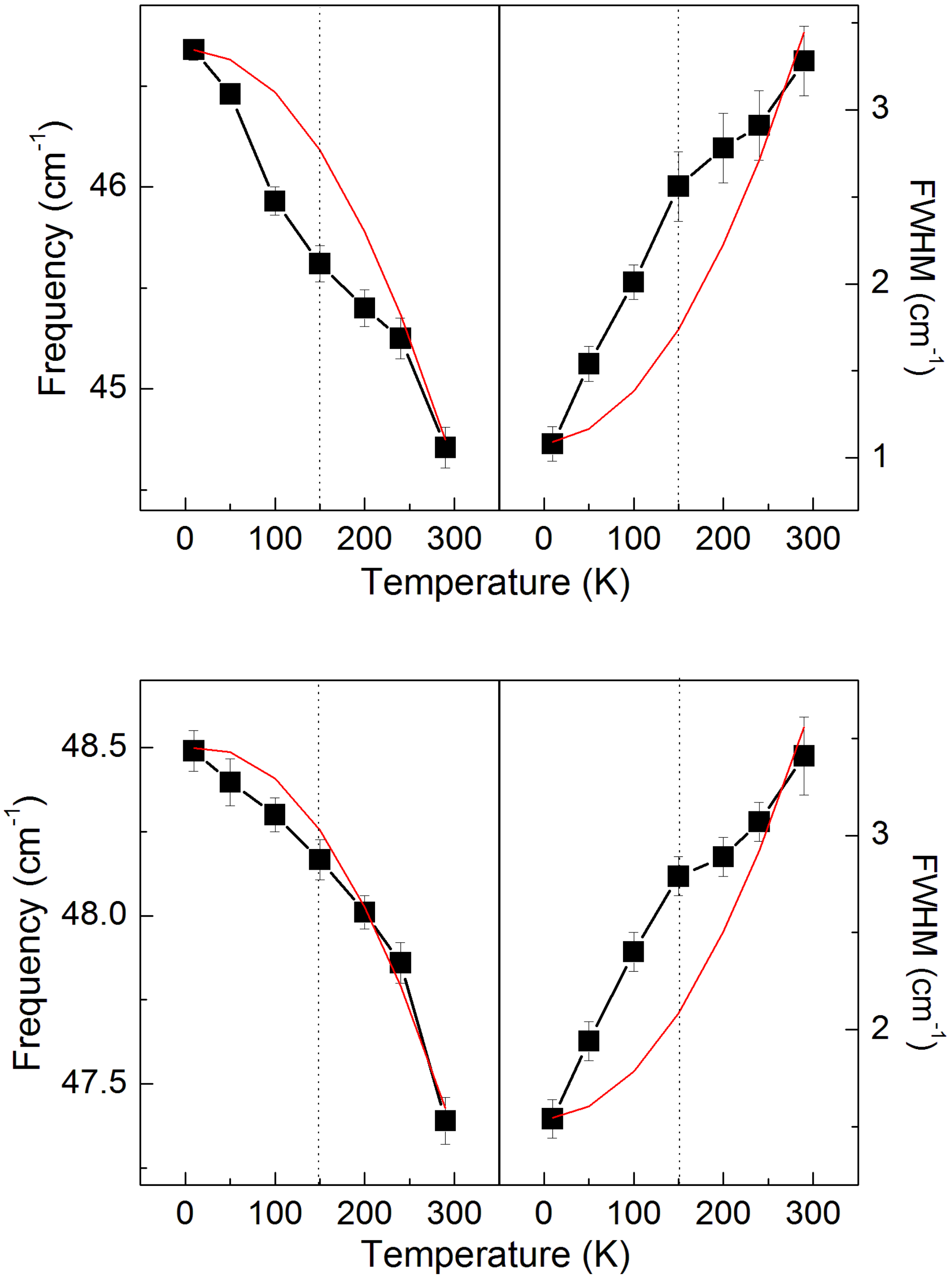

Figure 3.27: Temperature development of the phonon frequencies and linewidths for 46.5 cm^{-1} mode (upper graph) and 48.5 cm^{-1} mode (lower graph).

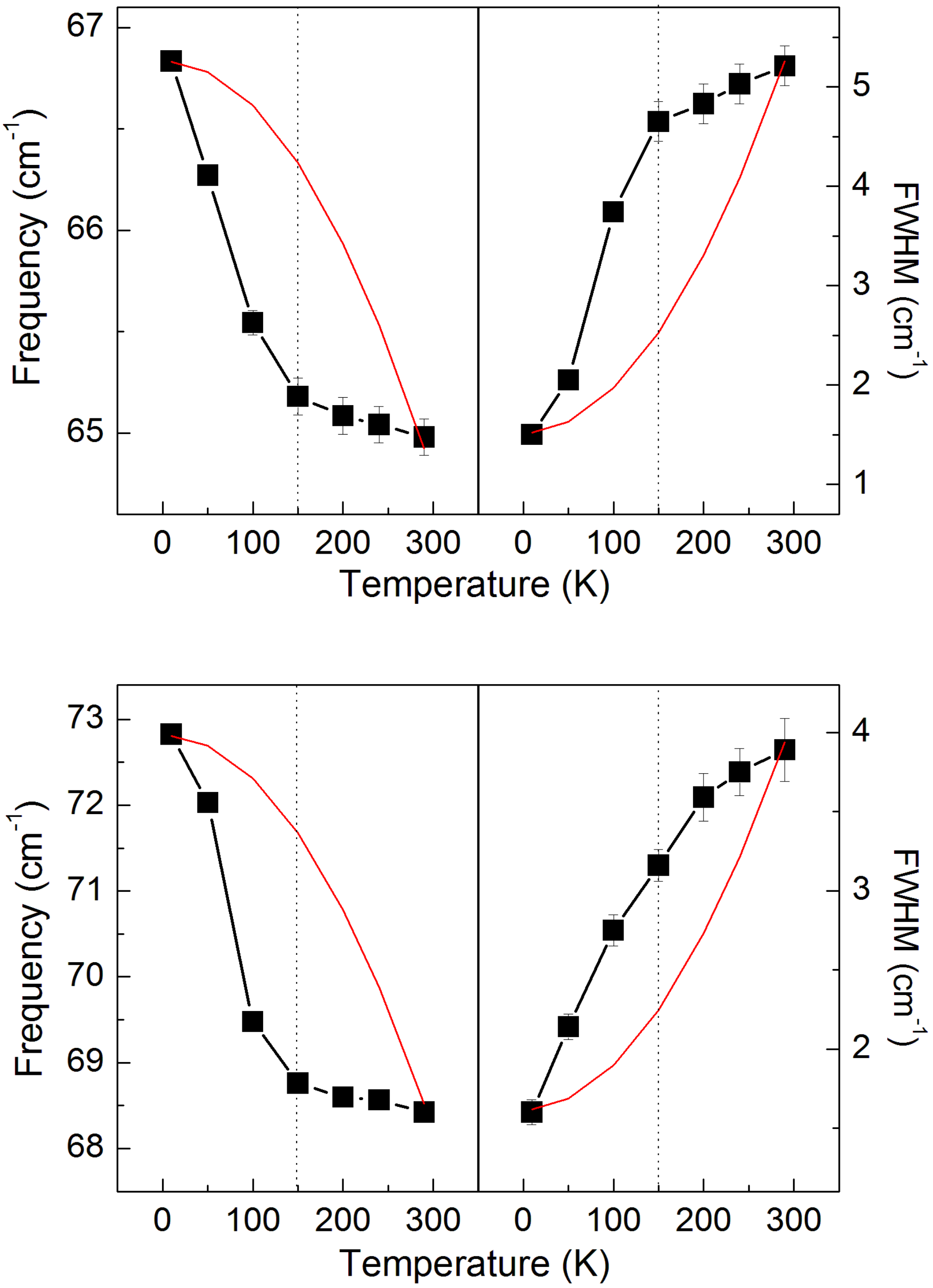

Figure 3.28: Temperature development of the phonon frequencies and linewidths for 67 cm^{-1} mode (upper graph) and 73 cm^{-1} mode (lower graph).

there is some interaction between electron and phonon systems in Cd_3As_2.

Charge carriers in semiconductors and metals play an important role in the Raman scattering process. There are several reasons which could affect electronic Raman spectra [61]. Two of them, i.e. charge density fluctuations and energy density fluctuations, will be discussed in particular for the 3D semimetal Cd_3As_2.

The electric screening of the fluctuations from current carriers is essential for Raman scattering. To differentiate one process from another, one has to consider the following aspect. If $q{\cdot}R_s \gg 1$, where q is a wave vector and R_s is screening radius, then there would be no screening of fluctuations. In order to fulfil such condition, the concentration of charged excitations should be small and the screening radius R_s should be quite large. Without screening the main process of Raman scattering is the charge density fluctuations. If $q{\cdot}R_s \ll 1$, there would be screening of charged excitations together with a long-range electric field. In this case the light scattering will change to energy density fluctuation, i.e. light scattering from collective plasmon excitations. Raman scattering for the latter process is related to nonparabolic semiconductors. It was well studied in the past for a wide range of concentrations and electronic temperatures [61]. Also, the collision frequency and its temperature dependence are important aspects in the coupling of light and energy density fluctuations [62].

We assume that in our case we have electron-electron inelastic scattering and electron-phonon inelastic scattering. The latter process originates from the transfer of energy to the phonons, i.e. inelastic scattering. In this process one has to consider the certain relaxation time t, which is changing together with temperature changes. Then the linewidth of the Lorentzian spectral line shape is $\Gamma = q^2{\cdot}x + \frac{1}{t}$ [61].

Quasielastic light scattering has a broad spectral response. Its group-symmetry analysis is complicated for the symmetry lower than cubic and requires an analysis of the fourth-rank electronic susceptibility tensor [61]. Our experiments show that the central peak is observed only in the parallel scattering geometry. This suggests that the scattering tensor for this mode has only diagonal polarisability components. Since charge density and energy density fluctuations have the same scalar symmetry, they could interfere. Their contributions to the optical spectra are not separated by the selection rules. Therefore, the analysis becomes more complicated with respect to the differentiation of these two processes. Hence, we have fitted the quasielastic scattering with Gaussian and Lorentzian spectral line shapes. Consequently, we established that Lorentzian shape for the central mode is more appropriate for our spectrum and it corresponds to the shape of energy density fluctuations. Thus, we state that the central mode of Cd_3As_2 is present due to energy density fluctuations.

3.2.8 Conclusion

Cd_3As_2 has special electronic structure, therefore anomalies were expected in the Raman scattering experiments. Indeed, there exists a competition of fluctuations between electronic structure and crystal structure. The anomalies were observed during temperature dependent measurements and revealed special temperature $\sim$ 150 K, where the behaviour deviates strongly from anharmonicity. In addition, resonance Raman scattering measurements demonstrated quasielastic scattering and strong resonance above $\sim$ 2.6 eV.

The number of the phonon modes in Cd_3As_2 leads to an assumption that its crystal structure is indeed centrosymmetric and that the compound actually belongs to the family of the Dirac semimetal systems.

Chapter 4

Light Scattering in Solar Energy Materials

4.1 Cu_2O Solar Cells: Fabrication and Characterisation

Sustainable photovoltaic devices gained a huge interest nowadays. They are expanding and increasing their part among other source materials. In order to meet the requirements of industry one should use metals which are available in our nature in large amounts [63]. In our case cuprous oxide (Cu_2O) and zinc oxide (ZnO) are good candidates due to their abundance in the Earth and consequently they are attractive candidates for photovoltaic production. Moreover, they are chemically stable, non-poisonous and can be used for cost-effective fabrication methods [64].

Theoretically, the Cu_2O absorbing layers used in solar cell devices could give power conversion efficiencies about 20 % [65, 66]. Cu_2O has a high optical absorption coefficient and it is a p-type direct bandgap semiconductor with an energy gap of around 2 eV [65, 67]. There are many different methods to produce Cu_2O thin films: molecular beam epitaxy (MBE) [68], sputtering [69, 70, 71], vapour phase epitaxy [72], metal-organic chemical vapour deposition (MOCVD) [73], sol-gel technique [74], atomic layer deposition (ALD) [75, 76] and electrochemical deposition [77, 78, 79, 80, 81]. Electrodeposition is a promising technique for thin film preparation due to its relatively low temperature chemical solutions and low cost [81, 82]. However, one of the main challenges in fabrication of Cu_2O solar cells is the problem of the n-doping process [79]. The optimization of the homojunctions by n-doping of Cu_2O eventually did not work out well due to the lack of photovoltaic applications [83]. Another opportunity has attracted attention of researchers, i.e. ZnO/Cu_2O heterojunction as well as transparent conductive oxides ZnO:Al and ZnO:Ga. It is quite a promising combination as they have a favourable alignment of the conduction band edges [79, 84].

Since Cu_2O is an active layer in the solar cell device, its properties will strongly affect the performance of such heterojunction. Furthermore, the effects of growth condition as bath temperature, pH and applied voltage were previously investigated [79, 81, 82, 85, 86]. However, the effects of the Cu_2O thin film thickness were not yet studied.

In this section we follow partly our article by Abdelfatah et al. [87].

4.1.1 Experimental Details

Cu_2O and Cu_2O/ZnO:Al thin films were grown by electrodeposition method. Raman scattering measurements were performed on thin films with different thicknesses d = 1, 2.7, 3.45, 8.74, and 11.35 μm in quasi-backscattering geometry. Light scattering polarization was parallel (xx) within the crystallographic ab plane. Sample surfaces were washed with acetone and isopropanol. Cleaned samples were measured at room temperature, ambient pressure and in the air.

As an incident Laser excitation a λ = 532 nm solid state laser was employed. The laser power was set to P = 3 mW with a spot diameter of approximately 3 μm to avoid heating effects and deterioration of the samples.

Experiments were performed using a micro-Raman setup (Horiba Labram) with liquid-nitrogen-cooled CCD (Horiba Jobin-Yvon, Spectrum One CCD-3000V).

4.1.2 Properties of the Phonon Spectrum

Raman spectra of Cu_2O solar cell device before and after ZnO:Al sputtering are provided in Fig. 4.1 and 4.2, respectively. The characteristic modes of Cu_2O and their frequencies are denoted with arrows (↓). We observe mostly these modes due to the large thickness of Cu_2O thin film itself in comparison to AZO layer. It was possible to detect only one ZnO A_1 (LO) phonon mode at around 579 cm^{-1} [88]. Since the investigated materials are semiconductors, the penetration depth of Raman scattering will be large enough, therefore during our experiments we probe the whole solar cell including the interface of the glass substrate. In the case of metal, for instance, one would have low penetration depth and screening of the laser signal. The different ratio of phonon intensities is ascribed to the surface imperfections. Frequency dependent offset in the spectra from the background scattering did not reveal any dependence on the film thickness. The reason of that arises from the other parts of the solar cell which remained identical, like the interfaces and the glass substrate.

The spectra we obtained are pretty well consistent with the symmetry analysis given in [89]. The most intensive peak of copper oxide is the second-order Raman allowed phonon $2E_u$ mode at 220 cm^{-1}. Phonon modes with lower intensity and large linewidth at about 308 and 515 cm^{-1} are attributed to the second order overtone A_{2u} mode and the Raman-allowed T_{2g} mode, respectively. Another broad peak at around 416 cm^{-1} corresponds to the four-phonon mode $3E_u$+T_{2u}. In addition, we have observed infrared-active modes at 628 and 645 cm^{-1} [89, 90]. Besides Cu_2O phonon

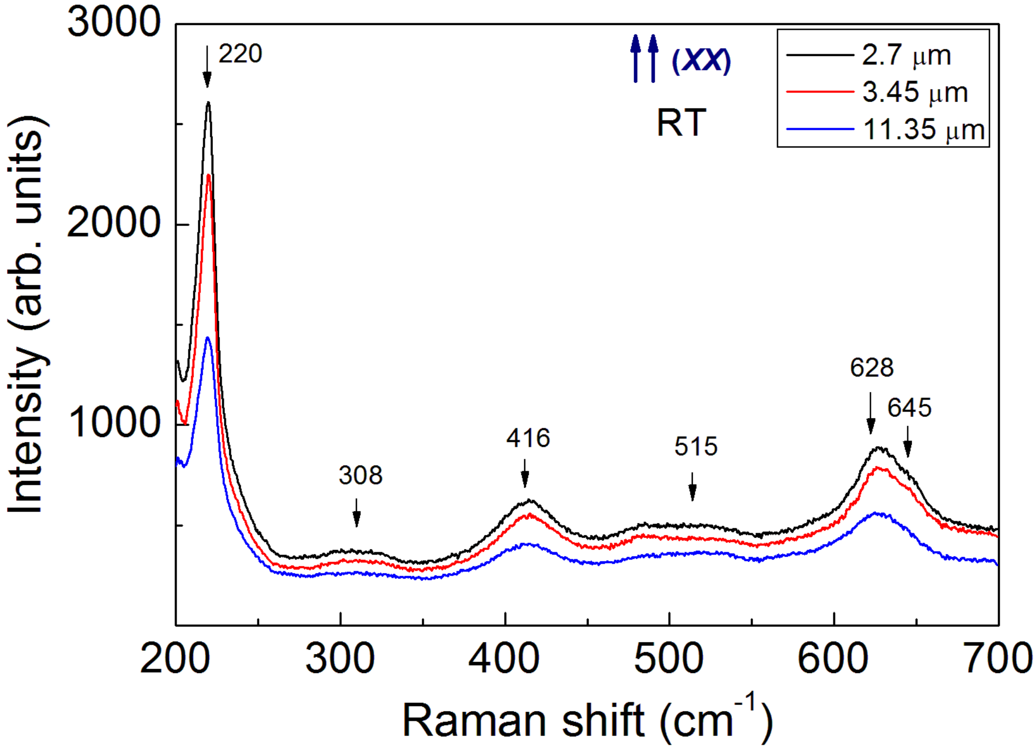

Figure 4.1: Polarized Raman spectra (xx) of Cu$_2$O thin films (d = 2.7, 3.45 and 11.35 μm) before AZO layer sputtering measured at room temperature using λ = 532 nm. Arrows denote characteristic modes of Cu$_2$O [87].

modes, the very weak mode (∗) at around 274 cm^{-1} appeared in spectra and it is attributed to CuO phase [91]. Our Raman data proves that by using electrodeposition method one can obtain the crystalline Cu_2O phase. Moreover, this small Raman peak of CuO phase is found only after sputtering of the AZO layer on top of Cu_2O thin film and thus it is attributed to a second phase formation during sputtering process.

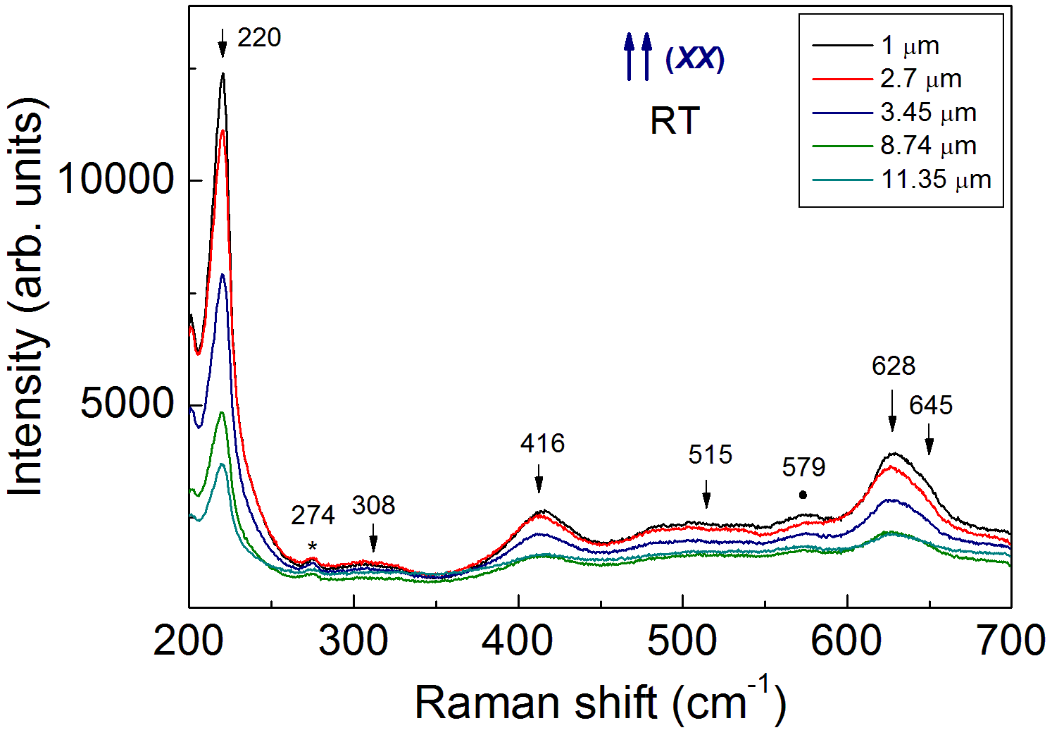

Figure 4.2: Polarized Raman spectra (xx) of AZO/Cu_2O solar cells ($d(Cu_2O)$ = 1, 2.7, 3.45, 8.74 and 11.35 μm) measured at room temperature using λ = 532 nm. Spectra contains Cu_2O (↓), CuO (∗) and ZnO (•) related modes [87].

4.1.3 Properties of the Solar Cell Device

In order to understand the AZO/Cu$_2$O heterojunction behaviour depending on the thin film thickness the experiments of electron beam induced current (EBIC), current-voltage characteristic (J-V), capacitance-voltage characteristic (C-V), reflectivity and external quantum efficiency (EQE) were carried out.

Side view SE image of a cleaved AZO/Cu$_2$O solar cell and schematic view of the device are presented in Fig. 4.3a and 4.3b, respectively. The thickness derived from Fig. 4.3a of the p-Cu$_2$O thin film is around 2.45 μm and ZnO:Al layer is about 0.25 μm. One should note that there are various voids close to the substrate and in Cu$_2$O thin film itself.

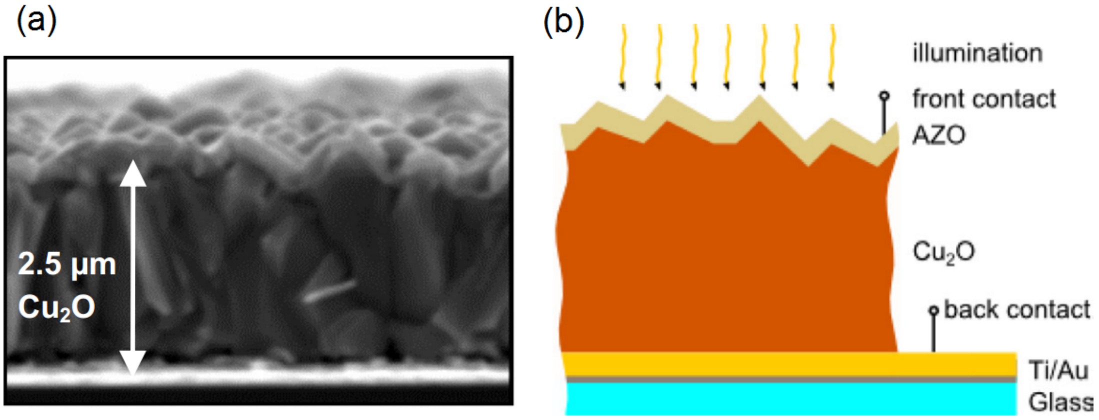

Figure 4.3: SE image (side view) of AZO/Cu$_2$O solar cell and its schematic diagram [87].

The J-V characteristics under dark conditions and at room temperature of the heterojunction properties of AZO/Cu$_2$O solar cells were done to estimate the effect of the Cu$_2$O layer thickness and shown in Fig. 4.4. Rectifying behaviour of the p-n junction was approved by these measurements. Thin films with larger thicknesses showed lower rectification, while thinner films in contrast provided higher rectification. The forward bias threshold voltage of the investigated solar cells depends on the thicknesses and lies in a range from 0.18 to 0.36 V, whilst the maximum has a thin film with thickness of around 3.5 μm. Such results correspond to the previous reports on Cu_2O/ZnO heterojunctions fabricated by electrochemical deposition and rf-magnetron sputtering [92]. Our thin films had the same conditions of the preparation by utilizing constant potential and therefore constant Cu^{2+} concentration giving the same composition of Cu_2O thin films. Thus, the various thin film thicknesses give different forward bias threshold voltages. In the case of the reverse direction of the junction it can be seen that the lowest leakage current provides the Cu_2O thin film with a thickness of around 3.5 μm. Furthermore, the solar cells with thinner Cu_2O layer have much higher value of the leakage current in comparison with the thicker layers. We attribute such behaviour with the voids between Cu_2O grains, which in turn give a short circuit (shunt) between upper and lower contacts during the layer deposition. In the case of the Cu_2O layer with a thickness of 3.5 μm, all Cu_2O grains stick tight to each other and they close nearly all voids from the top. Consequently, the leakage current generated by the shunt current almost vanishes. Further, the leakage current for the thicker Cu_2O layers is assigned to a large interface recombination current. In this case, the roughness of thicker layers is higher and more voids are created in-between Cu_2O grains due to bigger upper grains which formed on top of previous ones. In addition, it leads also to an incomplete coverage of the Cu_2O surfaces by the AZO layer.

The basic AZO/Cu_2O solar cell device basic parameters depending on Cu_2O thin film thickness, such as open circuit voltage V_{oc}, short circuit current density J_{sc}, fill factor FF and efficiency η, can be seen in Fig. 4.5 and 4.6. The values of these parameters were reproducible, every solar cell was measured 10 times under 1-sun (AM1.5G) illumination at room temperature. To make such plots the average values were utilized for each device. The open circuit voltage V_{oc} versus Cu_2O thin film thickness can be fitted with a Gaussian with the following parameters: an offset of 238 mV, a

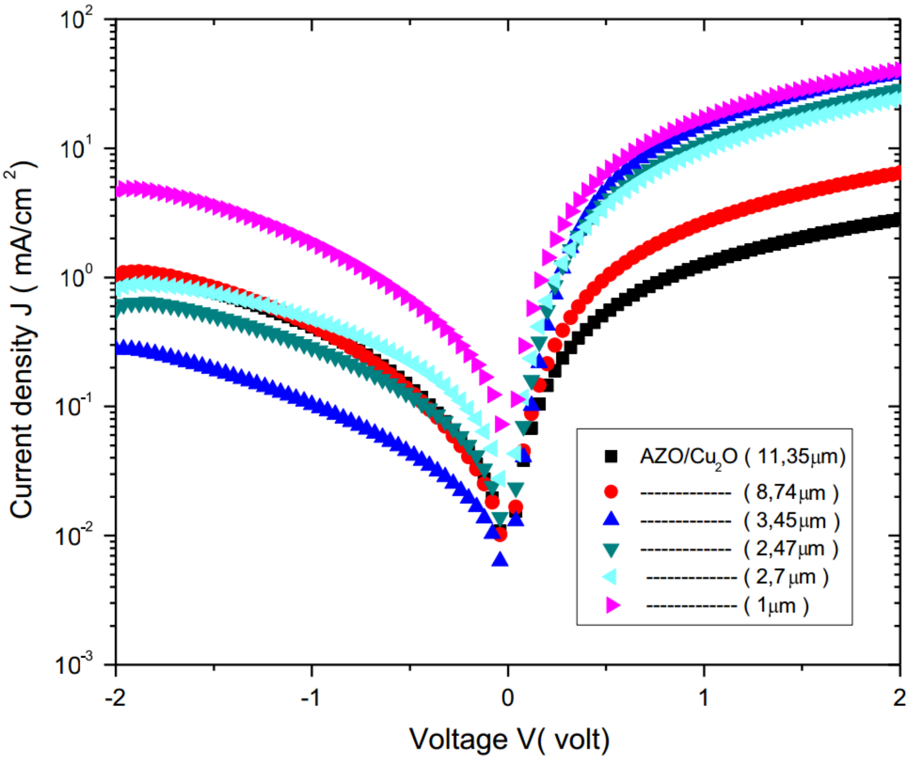

Figure 4.4: AZO/Cu$_2$O solar cell current-voltage characteristics measured under dark conditions [87].

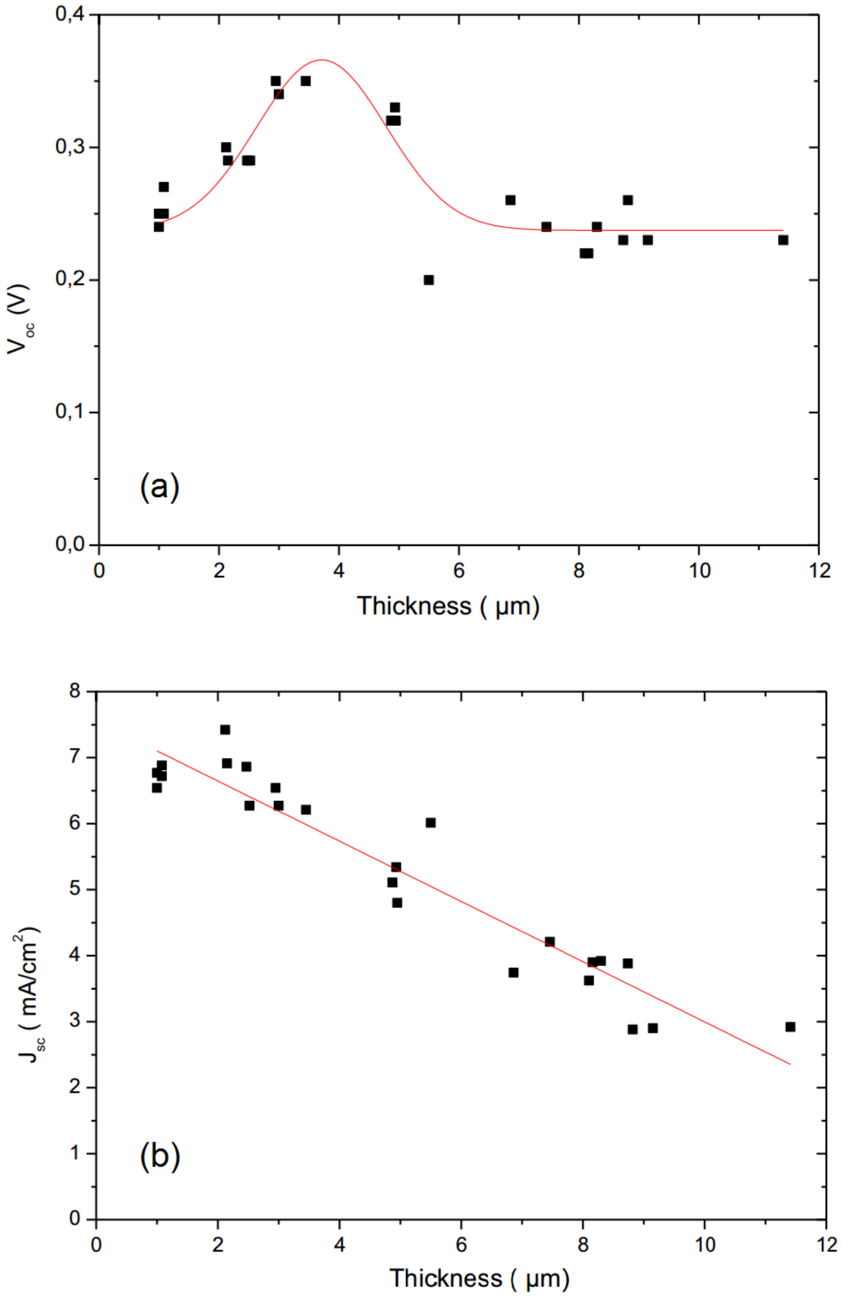

Figure 4.5: (a) Open circuit voltage (V_{oc}) and (b) short circuit current density (J_{sc}) of AZO/Cu_2O solar cells under 1-sun (AM 1.5G) illumination each including a Gaussian fit or linear fit. The standard deviation of the measurements of the same cell is very small, being around 0.005 and 0.004, for V_{oc} and J_{sc}, respectively [87].

maximum of $V_{oc,max}$ = 366 mV at a thickness around 3.7 μm and a linewidth of about 2.6 μm. The electron diffusion from the n-AZO layer to the p-Cu$_2$O thin film triggers the built-in potential of the depletion region and sets the limit for the V_{oc} of the solar cell device which is in turn diminished by leakage current. It was also found that the depletion region thickness from 2.3 to 3.0 μm yields a built-in potential in the range of 0.4 - 0.7 V for ZnO/Cu$_2$O heterojunction [93] which corresponds to the local rate of light absorption together with local collection efficiency. The overall generation rate of the light in AZO/Cu$_2$O solar cells consists of two parts: one is reflected light at the back contact and second one is reflected at the front surface. With respect to the spectral absorption coefficient and collection range, i.e diffusion to the junction, the highest efficiency can be achieved at a certain Cu$_2$O layer thickness. In our case, 3.4 μm provides the highest open circuit voltage and 3 μm gives the highest efficiency. Thus, in the thinner Cu$_2$O layers the light is reflected out of the device and in turn reduces V_{oc} and the generation rate, whereas in thicker Cu$_2$O layers the light absorbed far below the junction is not contributing to the photoeffect. These findings are consistent with earlier results presented for ZnO/Cu$_2$O heterojunctions [76, 93].

Second basic parameter of the solar cell which was measured is the short circuit current density J_{sc} and the results are presented in Fig 4.5b. Solar cells with Cu$_2$O layers with thicknesses below 4 μm showed 6 mA cm^{-2} short circuit current density which was expected from theoretical calculations [94]. Moreover, the obtained value is larger than for previously investigated ZnO/Cu$_2$O heterojunctions [76, 93]. From Fig. 4.5b we observe that J_{sc} is increasing with decreasing of Cu$_2$O layer thickness. We assume that the collection length of the minority carriers is lower than 1 μm which corresponds to the charge collection length of minority carriers in Cu$_2$O layer [93]. Thus, the electrons will recombine before collecting at distances larger than the collection length.

The fill factor (FF) of the solar cell device also depends on Cu$_2$O

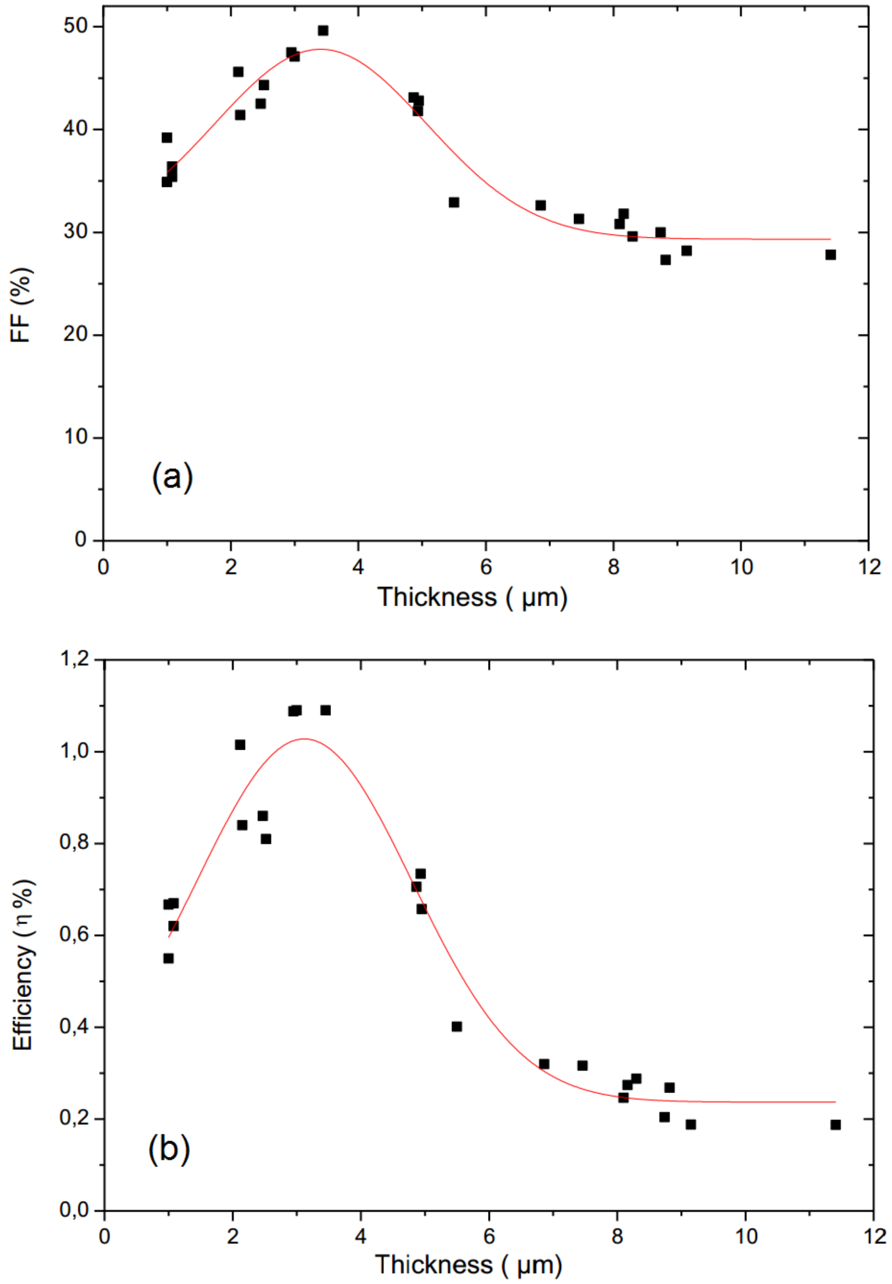

Figure 4.6: (a) Fill factor (FF) and (b) efficiency (η) of AZO/Cu_2O solar cells under 1-sun (AM 1.5G) illumination each including a Gaussian fit. The standard deviation of the measurements of the same cell is very small, being around 0.007 and 0.04 for FF and η, respectively [87].

thin film thickness and shown in Fig. 4.6a. The FF dependence can be fitted also with a Gaussian, similar to V_{oc}, with an offset of 29.3 %, a maximum of FF_{max} = 47.8 % at a thickness of around 3.4 μm and a FWHM of about 3.9 μm. The fill factor is an essential measure of quality of solar cell device and it is estimated by comparing the maximum power to theoretical power which is the product of the open circuit voltage and short circuit current. It also depends on the parallel to series resistances ratio in the device. By increasing of the film thickness, the series resistance will get larger, whereas the voids in-between Cu_2O layers will give a rise to shunt resistance. Therefore, such resistances will be lower for thinner films.

Another important characteristic of the solar cell is its efficiency (η). It is also dependent on Cu_2O absorber layer thickness and its dependence is shown in Fig. 4.6b. Similar to the open circuit voltage and the fill factor, the efficiency can be fitted with a Gaussian with an offset of 0.24 %, a maximum of η_{max} = 1.03 % at a thickness of around 3.1 μm and a FWHM of around 4 μm. The solar cells with Cu_2O thin films with 3.0 and 3.45 μm thicknesses give the highest efficiency of around 1.09 %. These efficiencies are higher than the values obtained for ZnO/Cu_2O solar cells [76, 93]. According to the Gaussian fits we have determined that the best parameters would have solar cells with Cu_2O thin films with thickness of about 3 μm. The efficiency dependence on the Cu_2O thin film thickness is in a good agreement with other dependencies, like the open circuit voltage and the fill factor due to the fact that η is proportional to these values. One of the effects which cause deterioration of the photovoltaic properties of the Cu_2O thin film solar cell is the possible formation of the CuO layer which has smaller band gap ($E_g \approx$ 1.4 eV) and which can be avoided by using atomic layer deposition technique [95, 96].

The external quantum efficiency (EQE) reflects the dependence of the short circuit current density J_{sc} for various Cu_2O thin films thicknesses. EQE dependence on different wavelengths is shown in Fig. 4.7. The absorption coefficient of Cu_2O decreases with in-

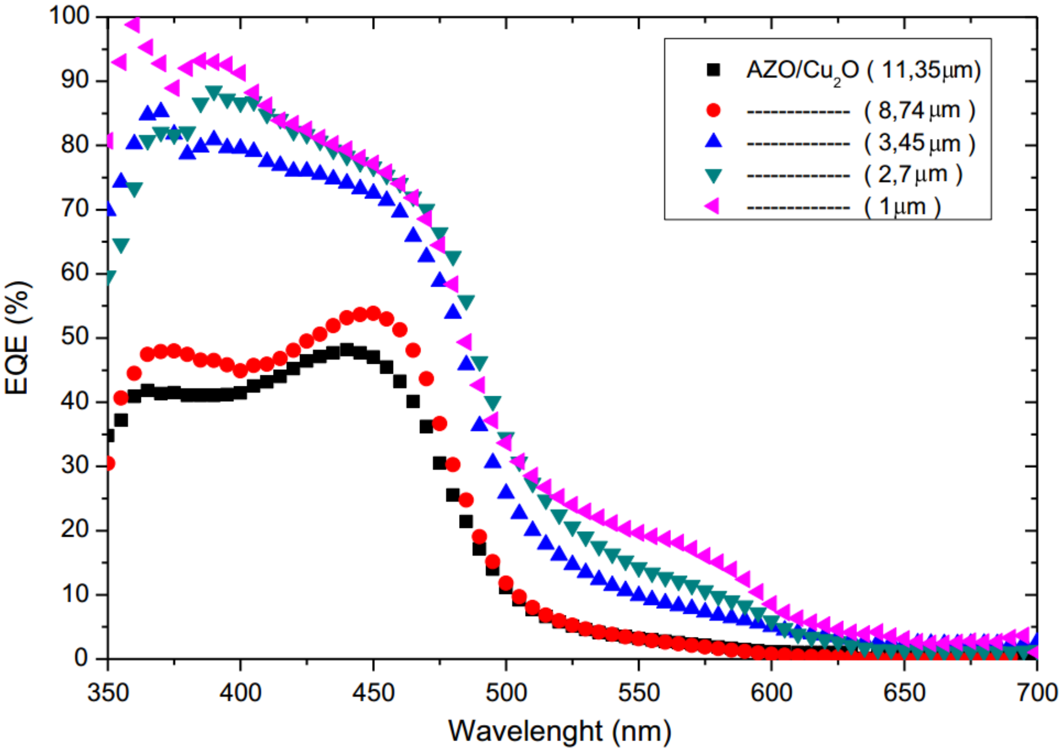

Figure 4.7: External quantum efficiency (EQE) of the investigated AZO/Cu$_2$O solar cell devices at room temperature [87].

creasing the incident light wavelength from 350 up to 500 nm and the photocurrent is generated mainly in this wavelength range [94]. For the wavelengths below 460 nm the optical depth of Cu$_2$O is less than 150 nm, thus photogenerated current carriers at the AZO-Cu$_2$O interface will be readily collected. For the wavelengths above 460 nm the optical depth reaches the micrometer scale and the minority charge carriers, i.e. electrons, generated by such photons will be at the large distance from p-n junction interface to be collected [94, 97]. In turn, with increasing of the Cu$_2$O thin film thickness the EQE is getting higher. In addition, the photon absorption is influenced by surface morphology and the light-reflection at the golden back contact of the device. Consequently, the short circuit current density J_{sc} increases, as well as the area under the EQE curve, with decreasing of the Cu$_2$O thin film thickness.

To estimate the acceptor concentration and built-in potential of the AZO/Cu$_2$O heterojunction, C-V experiments were performed using low frequency and at room temperature. They can be evaluated using the following formulas:

$$\frac{1}{C^2} = \frac{2}{\varepsilon\varepsilon_0 q N_A A^2}(V_b - V) \tag{4.1}$$

$$N_A = \frac{2}{\varepsilon\varepsilon_0 q A^2(\frac{d}{dV}(\frac{1}{C^2}))} \tag{4.2}$$

where N_A is an acceptor concentration (doping density) (1/cm^3), V$_b$ is the built-in potential, q is the charge of electron (1.60219×10^{-19} C), ε_0 is the permittivity of the free space (8.85×10^{-14} F/cm), ε is the relative permittivity of the Cu$_2$O layer (7.6), A is the area of the solar cell (0.0707 cm^2), V is the applied voltage and C is the measured capacitance. The extrapolation of the $1/C^2$ intercept along the V-axis gives the value of the built-in potential shown in Fig. 4.8. The linearity and increase of the capacitance are assigned to the charge trapping by impurity states or the intrinsic states of the bulk material [98]. Interestingly, the value of the highest open

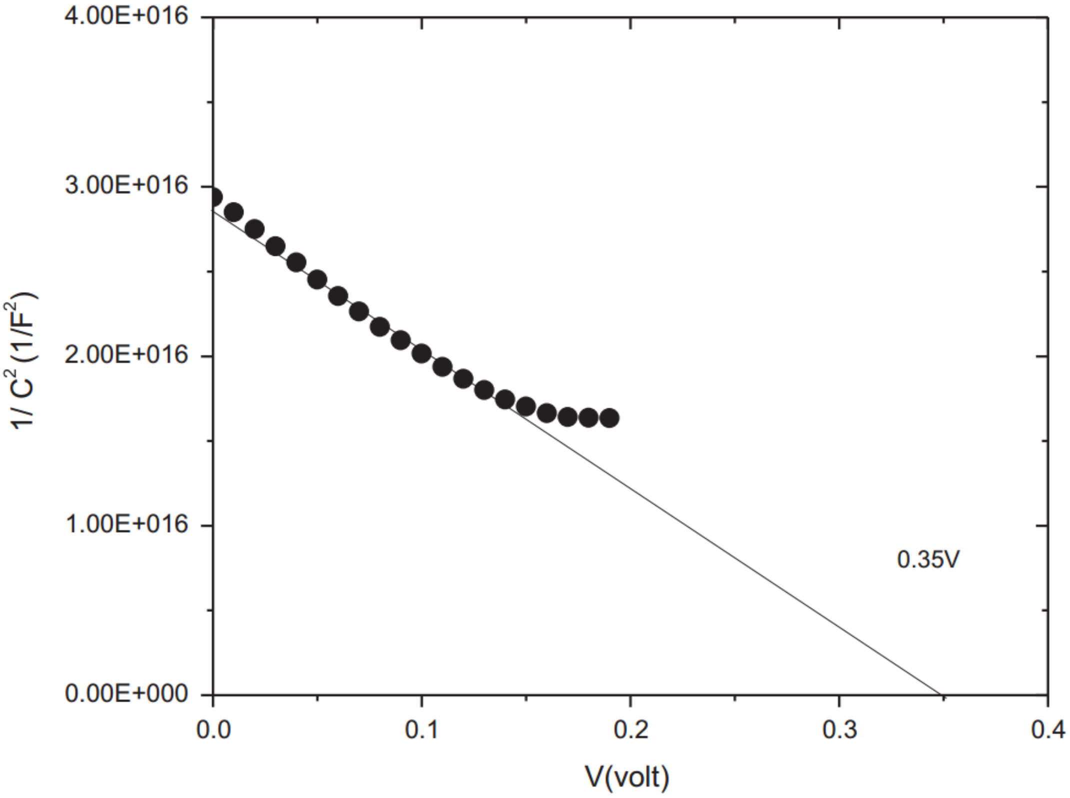

Figure 4.8: Capacitance-voltage characteristics of the AZO/Cu_2O solar cell with Cu_2O layer of 3.5 μm thickness measured at room temperature and under dark conditions [87].

circuit voltage V_{oc} for the AZO/Cu_2O solar cell device with the highest efficiency matches with the value of the built-in potential, i.e. 0.35 V. Therefore, we assume that V_b limits the open circuit voltage of the solar cell device and improvement of this value will help to obtain higher efficient solar cells in the future. One of the possibilities to maximise the built-in potential is an implementation of a thin buffer layer between AZO and Cu_2O. From Fig. 4.8 using the slope of the linear part of the curve and the Eg. 4.2 we have calculated the value of the acceptor concentration N_A, which is around 4.375×10^{16} cm^{-3}. Such N_A is two orders of magnitude larger than the value of previously investigated electrodeposited Cu_2O thin films [93]. The difference in acceptor concentrations lies in the preparation methods. The latter Cu_2O thin films were fabricated by using galvanostatic electrodeposition mode, while in our case we used the potentiostatic electrodeposition mode which makes available to make lower thin film resistivity. Thus, this mode provides higher acceptor concentration. In addition, the depletion layer thickness is assumed to be lower. Also, one can see that the basic solar cell parameters of the devices prepared by potentiostatic electrodeposition are higher than for galvanostatic mode [76, 93]. Therefore, we propose that the acceptor concentration N_A also limits the efficiency of the solar cell device.

4.1.4 Conclusion

The solar cell devices made with earth abundant materials, like Cu_2O and ZnO, are very promising candidates for the photovoltaic industry. In this work the effect of the thickness of the Cu_2O layer on the solar cell parameters was investigated. The thin films were prepared by cost-effective potentiostatic electrodeposition method. The highest efficiency of 1.09 % for the AZO/Cu_2O solar cell device was obtained for 0.35 V open circuit voltage (V_{oc}), 6.21 mA cm^{-2} short circuit current density (J_{sc}) and 50 % fill factor (FF). The thickness of about 3 μm of Cu_2O thin film as the absorber layer is supposed to be optimal value for the preparation of solar cells according to the Gaussian fit of our data. The AZO/Cu_2O solar cell device with the highest efficiency has the built-in potential (V_b) with 0.35 V and the acceptor concentration (N_A) with 4.375×10^{16} cm^{-3}. They are also assumed to be the limitation to the efficiency of the solar cells. Moreover, we discovered some other additional limitations. The minority carrier collection length of Cu_2O is lower than 1 μm and the electrons which are produced at distances much bigger than the charge collection length will recombine before getting the collection region. Furthermore, thicker layers might have a large interface recombination current which causes a raise of the leakage current, while thinner layers may have voids which also lead to the leakage current. Realization of a thin buffer layer at the AZO/Cu_2O interface might help to overcome such limitations.

4.2 Flexible Cu_2O Thin Film Solar Cells on Plastic Substrate

Thin film flexible solar cells are the prominent candidates for the space and aerospace industry, integrated photovoltaics and portable electronic devices [99]. This technology can help to fabricate lightweight solar cells and at the same time diminish the manufacturing and assembly costs of the solar energy materials [100]. The great number of flexible solar cells made from silicon or CIGS (copper-indium-gallium-selenide) which utilize relatively high temperatures for recrystallization or deposition, like 620 ^{o}C for polycrystalline Si or 600 ^{o}C for CIGS [99, 101]. However, the flexible plastic substrates have much lower melting temperature, for instance polyethylene terephthalate, which is commonly used as a plastic substrate, has a melting temperature just around 250 ^{o}C [99]. At the moment, one of the major issues is the search for the suitable materials and the cost-effective techniques to produce such solar cells.

Cu_2O/ZnO heterojunction-based solar cells fabricated by electrodeposition method are favourable option for the flexible photovoltaic devices. Many attempts have been done in order to enhance the conversion efficiency [102, 103]. The highest efficiency for polycrystalline n-ZnO/p-Cu_2O heterojunctions made by electrodeposition of both Cu_2O and ZnO layers is about 1.28 % [104]. Implementation of the gallium oxide Ga_2O_3 as a buffer layer into electrodeposited Cu_2O layer made possible to have an efficiency around 3.97 % [105].

In this chapter Raman scattering experiments, J-V, C-V characteristics and EQE will be presented for the electrodeposited flexible solar cell based on Cu_2O thin films on plastic foils.

In this section we follow partly our article by Abdelfatah et al. [106].

4.2.1 Properties of the Solar Cell Device

The Raman spectrum for the AZO/ZnO/Cu_2O solar cell device is presented in Fig. 4.9 and it is comparable to the results obtained for Cu_2O thin film solar cells discussed in chapter 4.1.

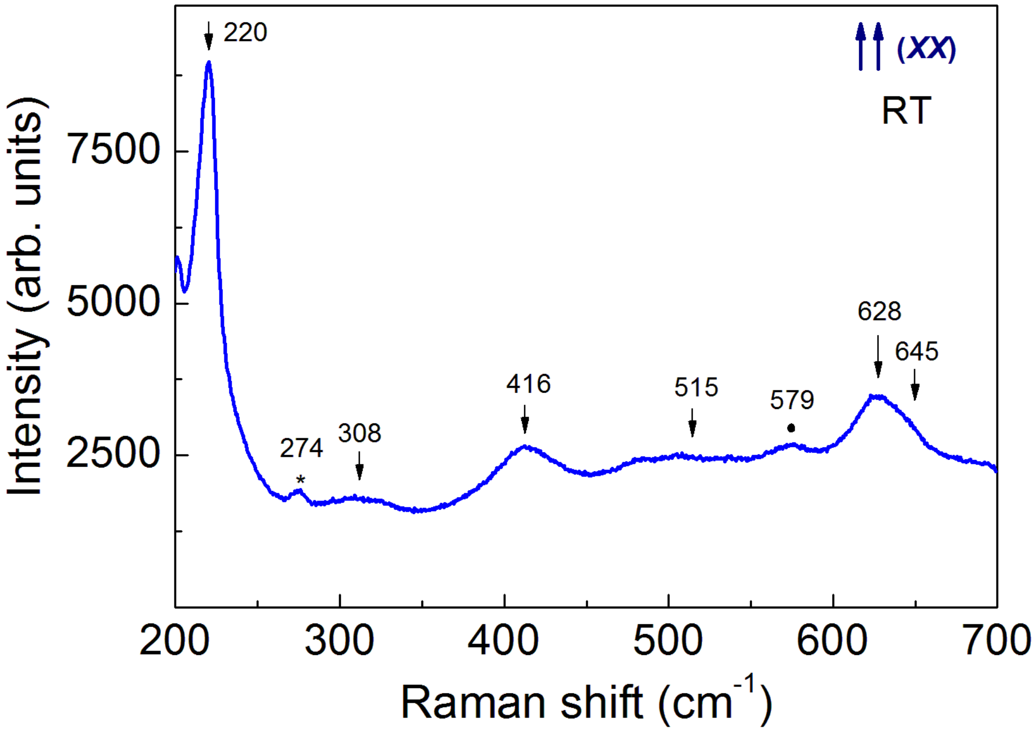

Figure 4.9: Polarized Raman spectra (xx) of AZO/ZnO/Cu_2O solar cell on a plastic substrate measured at room temperature using λ = 532 nm. Spectra contains Cu_2O (↓), CuO (∗) and ZnO (•) related modes [106].

The round and flexible AZO/ZnO/Cu_2O solar cells on top of the gold electrode on plastic foil are presented in Fig. 4.10a. The SE image of the surface of AZO/ZnO/Cu_2O heterojunction is shown in Fig. 4.10b. The device contains pyramid-like grains of cuprous oxide which are beneficial in terms of the optical reflection [64, 107].

Side view SE image of a cleaved AZO/ZnO/Cu$_2$O solar cell device is presented in Fig. 4.10c. The thickness of the AZO layer and p-Cu$_2$O layer are around 0.25 μm and 3.4 μm, respectively. The schematic view of the solar cell is presented in Fig. 4.10d to illustrate the structure of the device.

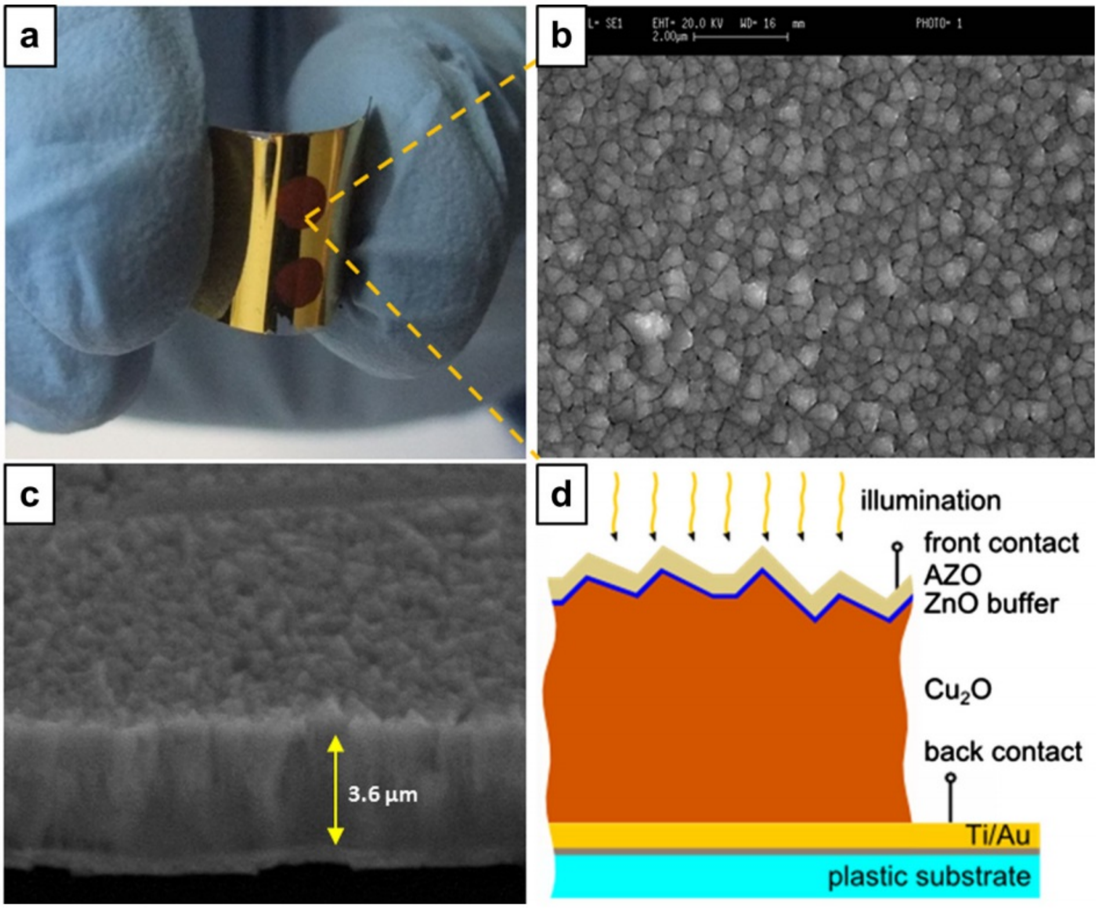

Figure 4.10: (a) Photo image of the solar cell. (b) SEM surface view. (c) SEM side view. (d) The schematic view of AZO/ZnO/Cu$_2$O solar cell on a plastic substrate [106].

The analysis of the device of interest showed a usual rectifying behaviour of the J-V curve investigated under dark conditions, 1-sun (AM1.5G) illumination and at room temperature. The basic device parameters obtained for the solar cell: an open circuit voltage (V_{oc}) is about 300 mV, a short circuit current density (J_{sc})

is 6.819 ± 0.048 mA cm^{-2}, fill factor (FF) is 0.439 ± 0.006 and the power conversion efficiency (η) is 0.897 ± 0.005 % [106]. The values were reproducible for the whole set of 10 measurements.

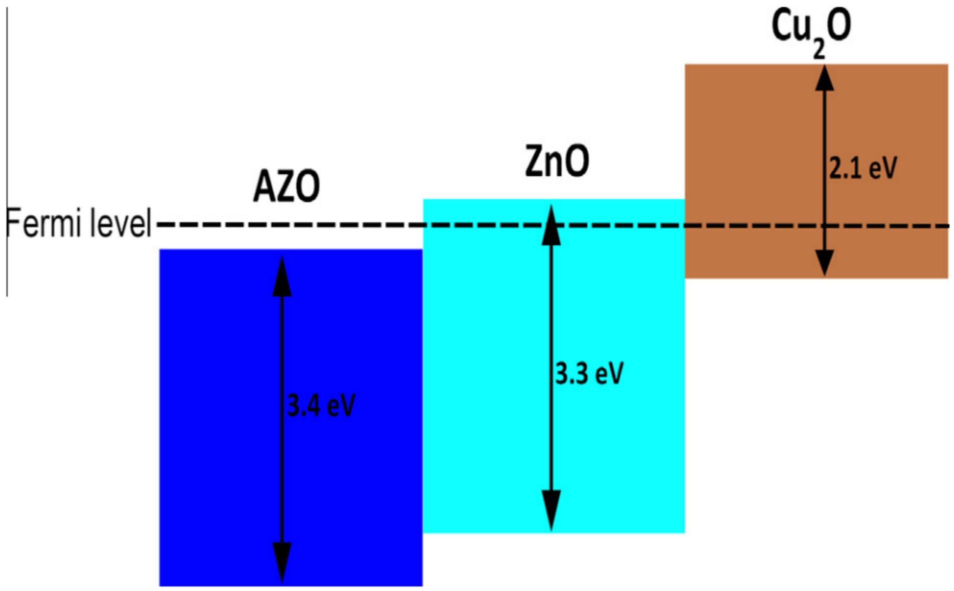

Figure 4.11: The schematic energy band diagram of AZO/ZnO/Cu_2O solar cell [106].

The schematic energy diagram for the AZO/ZnO/Cu_2O flexible solar cell is presented in Fig. 4.11. Implementation of 5 nm of ZnO as a thin buffer layer allowed to improve the efficiency of the solar cell in comparison with the AZO/Cu_2O heterojunctions where Cu_2O was also electrodeposited [85, 108]. The photovoltaic properties of the heterojunction are affected by the conduction band discontinuity height, resulting from the difference in electron affinity between the n-semiconductor buffer layer and the Cu_2O film in the heterojunction [109]. Moreover, we assume that the conduction band discontinuity of an AZO/p-Cu_2O heterojunction might be higher than of an n-ZnO/Cu_2O heterojunction. In addition, by introducing ZnO buffer layer the increase of the efficiency of the solar cell could be affected due to the metallorganic source material (DEZn) on the Cu_2O surface through the first stages of the ALD process.

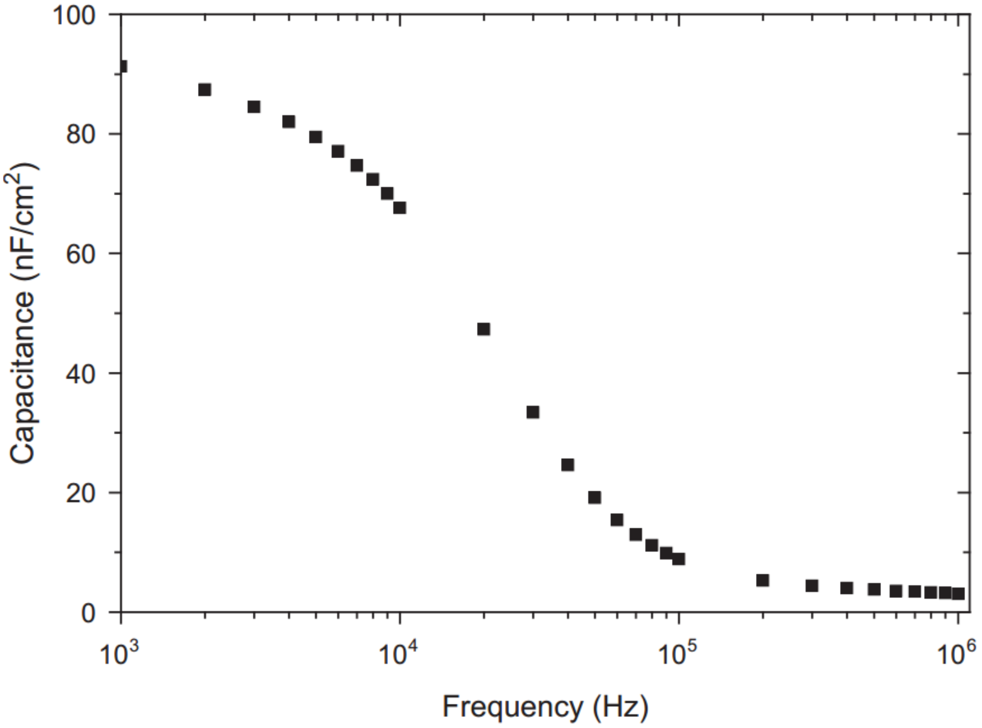

Figure 4.12: Capacitance-frequency characteristics of the AZO/ZnO/Cu_2O solar cell device measured with 0 V (DC) bias under dark conditions and at room temperature [106].

To define the properties of the AZO/ZnO/Cu_2O solar cell device, the C-*f* and C-V experiments were done utilizing various frequencies at room temperature. The capacitance dependence on different frequencies is shown in Fig. 4.12. The capacitance of the AZO/ZnO/Cu_2O heterojunction plateaus to a depletion capacitance (C_d) at low frequencies and has a value of around 91 nF/cm^2. This value of C_d is affected mostly by the intrinsic and extrinsic doping concentrations of the materials which in turn will modify the width of the depletion region. The capacitance diminishes and attains the value from 2 to 5 nF/cm^2 at higher frequencies and reaches the point, where the heterojunction becomes insulating due to the dielectric freeze-out in the Cu_2O. It originates in a geometric capacitance (C_g) between AZO and the back contact [64].

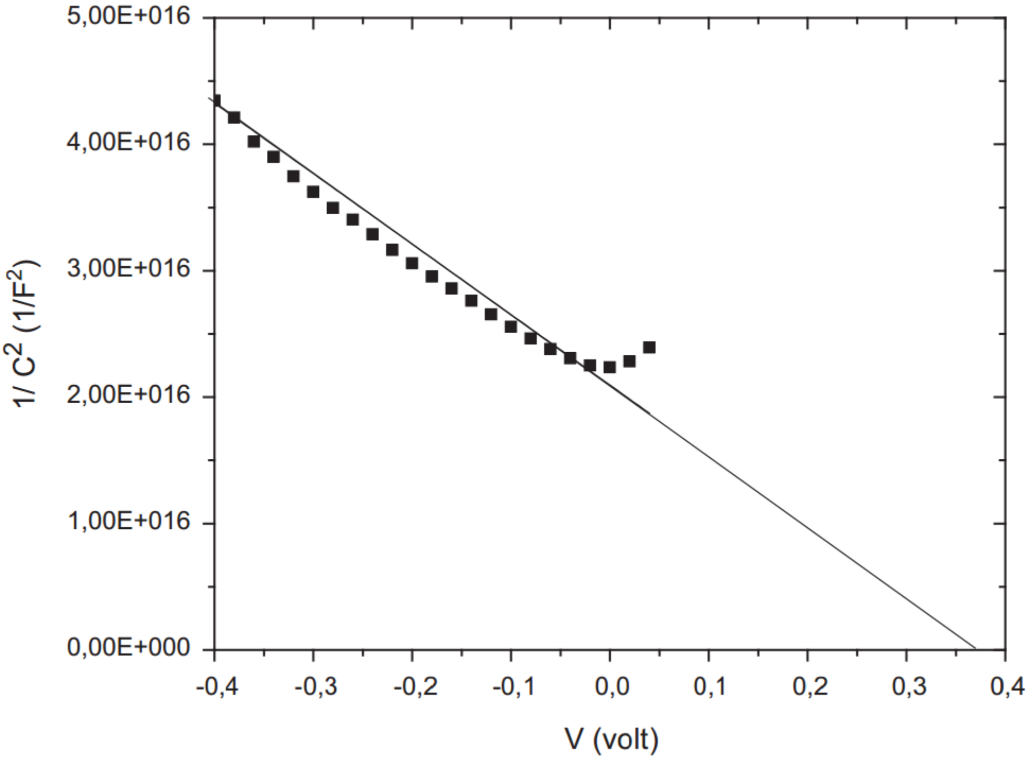

Figure 4.13: Capacitance-voltage characteristics of the AZO/ZnO/Cu_2O solar cell device measured under dark conditions and at room temperature [106].

The C-V measurements were carried out and are presented in Fig. 4.13. The values of the built-n potential (V_b) and the acceptor concentration (N_a) were calculated by using eq. 4.1 and 4.2. The obtained values are around 0.37 V and 6.67×10^{16} cm^{-3}, respectively. These results are slightly higher than for the solar cells electrodeposited on the glass substrate we have reported earlier [87].

The width of the depletion region w_d was determined by the following formula [98]:

$$w_d = \sqrt{\frac{2\varepsilon\varepsilon_0 V_b}{qN_A}} \tag{4.3}$$

and it is around 67 nm, whereas the Cu$_2$O thin film thickness, in contrast, is much larger. Thus, the overall thickness which contributes to the photocurrent will be in a range of around micrometer.

4.2.2 Conclusion

Heterojunction flexible solar cells with electrodeposited Cu$_2$O thin film on a plastic substrate were successfully prepared. To enhance the junction confinement, a thin buffer layer of ZnO with a thickness of 5 nm was implemented by using ALD. The highest achieved values for the AZO/ZnO/Cu$_2$O flexible solar cell for the open circuit voltage (V_{oc}), the short circuit current (J_{sc}), the fill factor (FF) and the efficiency (η) were 300 mV, 6.77 mA cm^{-2}, 44 % and 0.904 %, respectively. The reverse biased C-V experiments allowed to define the built-in potential (V_b) of 0.37 V, the acceptor concentration (N_a) of 6.67 × 10^{16} cm^{-3} and the depletion region width (w_d) of 67 nm. This approach to produce lightweight and even flexible solar cells along with its low preparation and installation costs is promising candidate for the photovoltaic industry.

Chapter 5

Summary

This thesis reports on experimental findings of inelastic light scattering from the compounds with strong SOC, such as Pb_xTaSe_2 and Cd_3As_2. In addition, the solar energy materials, as Cu_2O and CuO, were investigated by means of Raman spectroscopy technique.

In the first part of the thesis, the electronic and crystal structure of $PbTaSe_2$ are discussed. Pb intercalation, besides crystal structure, changes significantly the electronic band structure, revealing Dirac points in the k space and also newly found topological nodal-line states (TNLS). The parental compound $TaSe_2$ is a layered material, which consists of CDW phase below T_{CDW} = 90 K and superconducting phase below 150 mK. Upon Pb intercalation, the T_c increases drastically and superconducting phase in $PbTaSe_2$ appears at 3.8 K. It was also found that there is a distinct effect of Pb doping on the E_{2g} phonon mode, i.e. it is hardened much more (about 10 %) than in the case of increasing number of layers in $TaSe_2$ [26]. This fact indicates that there is a non-trivial interaction between Pb and TaSe layers. Temperature and resonance Raman scattering experiments also unveil new modes which have low energies and broad linewidths. They are, in fact, not the symmetry-allowed Raman modes but attributed to either a PbSe phase or other defects which may appear after the Pb intercalation process.

The second part of the thesis is dedicated to the topological Dirac semimetal Cd_3As_2. It was already investigated earlier due to its impressive transport properties, but only recently researchers discovered its exotic electronic structure. It has semimetallic character, i.e. valence and conduction bands "touch" at one specific point. It is quite similar to graphene and the surface of topological insulators, however, Cd_3As_2 possess Dirac fermions in the bulk, i.e. it is considered as 3D analogue of graphene. The presence or absence of the inversion symmetry in such materials is important for the electronic structure, for instance, absence of it would drive such a system into the Weyl semimetal phase. Therefore, the determination of the crystal structure is essential. With the help of Raman scattering experiments we assume that the crystal structure is centrosymmetric and Cd_3As_2 is indeed a Dirac semimetal. Moreover, the temperature dependent Raman spectra showed that phonon modes have higher intensity at low temperatures, whereas the quasielastic mode has the highest intensity at room temperature. Therefore, we state that there is a special electron-phonon interaction, which also leads to related phonon anomalies. The temperature dependence of the phonon modes deviates from anharmonicity and has the highest effect at T = 150 K. The origin of such anomalies are yet to be investigated deeply in the future.

In the last part of the thesis but not least, solar cell devices based on Cu_2O were studied. Here, the effects of the growth conditions of Cu_2O, such as temperature, pH level and applied voltage were considered. The thickness of the active Cu_2O layer plays an important role, as it affects the basic parameters of the final device. The optimal value of the Cu_2O thickness is about 3 μm. With this thickness the highest possible efficiency of AZO/Cu_2O solar cell device of 1.09 % was achieved. In addition, it was possible to make flexible solar cells based on Cu_2O and plastic substrate, instead of glass, with the maximal efficiency of 0.904 %. Raman scattering spectroscopy is an important tool in this project, since it can be used for crystal structure and composition determination, for instance, the experiments made possible very quickly and easily distinguish Cu_2O and undesired CuO, since they have phonon modes at very different frequencies.

Bibliography

[1] A. Smekal, "Zur Quantentheorie der Dispersion," *Die Naturwissenschaften*, vol. 11, pp. 873–875, oct 1923.

[2] H. A. Kramers and W. Heisenberg, "Über die Streuung von Strahlung durch Atome," *Zeitschrift für Physik*, vol. 31, pp. 681–708, feb 1925.

[3] P. Lemmens and K. Y. Choi, "Scattering: Inelastic Scattering Technique - Raman," in *Encyclopaedia of Condensed Matter Physics* (G. Bassani, G. Liedl, and P. Wyder, eds.), Elsevier, 2005.

[4] G. E. Jellison, D. H. Lowndes, and R. F. Wood, "Importance of temperature-dependent optical properties for Raman-temperature measurements for silicon," *Physical Review B*, vol. 28, pp. 3272–3276, sep 1983.

[5] B. N. Narozhny, "Spin diffusion in one-dimensional antiferromagnets," *Physical Review B*, vol. 54, pp. 3311–3321, aug 1996.

[6] J. W. Halley, "Light Scattering as a Probe of Dynamical Critical Properties of Antiferromagnets," *Physical Review Letters*, vol. 41, pp. 1605–1608, dec 1978.

[7] E. Merzbacher, *Quantum mechanics*. Wiley, 1998.

[8] Bilbao Crystallographic Server. The crystallographic site at the condensed matter physics dept. of the university of the basque country, "http://www.cryst.ehu.es/," 2016.

[9] M. Xu, T. Liang, M. Shi, and H. Chen, "Graphene-like two-dimensional materials.," *Chemical reviews*, vol. 113, pp. 3766–98, may 2013.

[10] J. A. Wilson and A. D. Yoffe, "The transition metal dichalcogenides discussion and interpretation of the observed optical, electrical and structural properties," *Adv. Phys.*, vol. 18, no. 73, pp. 193–335, 1969.

[11] M. N. Ali, Q. Gibson, S. Jeon, B. B. Zhou, A. Yazdani, and R. J. Cava, "The crystal and electronic structures of Cd_3As_2, the three-dimensional electronic analogue of graphene.," *Inorganic chemistry*, vol. 53, pp. 4062–7, apr 2014.

[12] K. Ishizaka, M. S. Bahramy, H. Murakawa, M. Sakano, T. Shimojima, T. Sonobe, K. Koizumi, S. Shin, H. Miyahara, A. Kimura, K. Miyamoto, T. Okuda, H. Namatame, M. Taniguchi, R. Arita, N. Nagaosa, K. Kobayashi, Y. Murakami, R. Kumai, Y. Kaneko, Y. Onose, and Y. Tokura, "Giant Rashba-type spin splitting in bulk BiTeI," *Nature Materials*, vol. 10, no. 7, pp. 521–526, 2011.

[13] W. Zhao, Z. Ghorannevis, K. K. Amara, J. R. Pang, M. Toh, X. Zhang, C. Kloc, P. H. Tan, and G. Eda, "Lattice dynamics in mono- and few-layer sheets of WS_2 and WSe_2.," *Nanoscale*, vol. 5, pp. 9677–83, oct 2013.

[14] E. Z. Kuchinskii, I. A. Nekrasov, and M. V. Sadovskii, "Electronic structure of two-dimensional hexagonal diselenides: Charge density waves and pseudogap behavior," *Journal of Experimental and Theoretical Physics*, vol. 114, no. 4, pp. 671–680, 2012.

[15] R. Eppinga and G. Wiegers, "A generalized scheme for niobium and tantalum dichalcogenides intercalated with post-transition elements," *Physica B+C*, vol. 99, pp. 121–127, jan 1980.

[16] R. Sankar, G. N. Rao, I. P. Muthuselvam, G. Bian, H. Zheng, G. P.-J. Chen, T.-R. Chang, S. Xu, G. S. Murgan, C.-H. Lin, W.-L. Lee, H.-T. Jeng, M. Z. Hasan, and F.-C. Chou, "Single crystal growth and physical property characterization of $PbTaSe_2$ as a noncentrosymmetric type-II superconductor," p. 24, nov 2015.

[17] E. Bauer and M. Sigrist, eds., *Non-Centrosymmetric Superconductors*, vol. 847 of *Lecture Notes in Physics*. Berlin, Heidelberg: Springer Berlin Heidelberg, 2012.

[18] M. S. Bahramy, R. Arita, and N. Nagaosa, "Origin of giant bulk Rashba splitting: Application to BiTeI," *Physical Review B*, vol. 84, p. 041202, jul 2011.

[19] M. Z. Hasan and C. L. Kane, "Colloquium: Topological insulators," *Reviews of Modern Physics*, vol. 82, pp. 3045–3067, nov 2010.

[20] T. Liang, Q. Gibson, J. Xiong, M. Hirschberger, S. P. Koduvayur, R. J. Cava, and N. P. Ong, "Evidence for massive bulk Dirac fermions in Pb_xSn_xSe from Nernst and thermopower experiments.," *Nature communications*, vol. 4, p. 2696, jan 2013.

[21] Z. K. Liu, B. Zhou, Y. Zhang, Z. J. Wang, H. M. Weng, D. Prabhakaran, S.-K. Mo, Z. X. Shen, Z. Fang, X. Dai, Z. Hussain, and Y. L. Chen, "Discovery of a three-dimensional topological Dirac semimetal, Na_3Bi.," *Science (New York, N.Y.)*, vol. 343, pp. 864–7, feb 2014.

[22] M. Neupane, S.-Y. Xu, R. Sankar, N. Alidoust, G. Bian, C. Liu, I. Belopolski, T.-R. Chang, H.-T. Jeng, H. Lin, A. Bansil, F. Chou, and M. Z. Hasan, "Observation of a three-dimensional topological Dirac semimetal phase in high-mobility Cd_3As_2.," *Nature communications*, vol. 5, p. 3786, jan 2014.

[23] G. Bian, T.-R. Chang, R. Sankar, S.-Y. Xu, H. Zheng, T. Neupert, C.-K. Chiu, S.-M. Huang, G. Chang, I. Belopolski, D. S. Sanchez, M. Neupane, N. Alidoust, C. Liu, B. Wang, C.-C. Lee, H.-T. Jeng, C. Zhang, Z. Yuan, S. Jia, A. Bansil, F. Chou, H. Lin, and M. Z. Hasan, "Topological nodal-line fermions in spin-orbit metal $PbTaSe_2$.," *Nature communications*, vol. 7, p. 10556, jan 2016.

[24] M. N. Ali, Q. D. Gibson, T. Klimczuk, and R. J. Cava, "Noncentrosymmetric superconductor with a bulk three-dimensional Dirac cone gapped by strong spin-orbit coupling," *Physical Review B*, vol. 89, p. 20505, jan 2014.

[25] J. Laverock, D. Newby, E. Abreu, R. Averitt, K. E. Smith, R. P. Singh, G. Balakrishnan, J. Adell, and T. Balasubramanian, "k -resolved susceptibility function of 2H-$TaSe_2$ from angle-resolved photoemission," *Physical Review B*, vol. 88, p. 035108, jul 2013.

[26] P. Hajiyev, C. Cong, C. Qiu, and T. Yu, "Contrast and Raman spectroscopy study of single- and few-layered charge density wave material: 2H-$TaSe_2$," *Scientific reports*, vol. 3, p. 2593, 2013.

[27] S. Sugai, K. Murase, S. Uchida, and S. Tanaka, "Comparison of the soft modes in tantalum dichalcogenides," *Physica B+C*, vol. 105, pp. 405–409, may 1981.

[28] J. Habinshuti, O. Kilian, O. Cristini-Robbe, A. Sashchiuk, A. Addad, S. Turrell, E. Lifshitz, B. Grandidier, and L. Wirtz,

"Anomalous quantum confinement of the longitudinal optical phonon mode in PbSe quantum dots," *Physical Review B*, vol. 88, p. 115313, sep 2013.

[29] C. Gayner and K. K. Kar, "Inherent room temperature ferromagnetism and dopant dependent Raman studies of PbSe, Pb(1-x)Cu$_x$Se, and Pb(1-x)Ni$_x$Se," *Journal of Applied Physics*, vol. 117, no. 10, p. 103906, 2015.

[30] A. Donkov, M. M. Korshunov, I. Eremin, P. Lemmens, V. Gnezdilov, F. C. Chou, and C. T. Lin, "Electron-phonon interaction in the lamellar cobaltate Na$_x$CoO$_2$," *Physical Review B*, vol. 77, p. 100504, mar 2008.

[31] T. Wu, K. Liu, H. Chen, G. Wu, Q. L. Luo, J. J. Ying, and X. H. Chen, "Rearrangement of sodium ordering and its effect on physical properties in the Na$_x$CoO$_2$ system," *Physical Review B*, vol. 78, p. 115122, sep 2008.

[32] E. F. Steigmeier, G. Harbeke, H. Auderset, and F. J. DiSalvo, "Softening of charge density wave excitations at the superstructure transition in 2H-TaSe$_2$," *Solid State Communications*, vol. 20, no. 7, pp. 667–671, 1976.

[33] S. Sahoo, A. P. S. Gaur, M. Ahmadi, M. J.-F. Guinel, and R. S. Katiyar, "Temperature-Dependent Raman Studies and Thermal Conductivity of Few-Layer MoS$_2$," *The Journal of Physical Chemistry C*, vol. 117, pp. 9042–9047, may 2013.

[34] A. A. Reijnders, Y. Tian, L. J. Sandilands, G. Pohl, I. D. Kivlichan, S. Y. F. Zhao, S. Jia, M. E. Charles, R. J. Cava, N. Alidoust, S. Xu, M. Neupane, M. Z. Hasan, X. Wang, S. W. Cheong, and K. S. Burch, "Optical evidence of surface state suppression in Bi-based topological insulators," *Physical Review B - Condensed Matter and Materials Physics*, vol. 89, no. 7, p. 075138, 2014.

[35] C. Lee, H. Yan, L. E. Brus, T. F. Heinz, J. Hone, and S. Ryu, "Anomalous lattice vibrations of single- and few-layer MoS_2.," *ACS nano*, vol. 4, pp. 2695–700, may 2010.

[36] N. Kuroda and Y. Nishina, "Davydov splitting of degenerate lattice modes in the layer compound GaS," *Physical Review B*, vol. 19, pp. 1312–1315, jan 1979.

[37] T. J. Wieting and J. L. Verble, "Interlayer Bonding and the Lattice Vibrations of beta-GaSe," *Physical Review B*, vol. 5, pp. 1473–1479, feb 1972.

[38] H. Barath, M. Kim, J. F. Karpus, S. L. Cooper, P. Abbamonte, E. Fradkin, E. Morosan, and R. J. Cava, "Quantum and classical mode softening near the charge-density-wave- superconductor transition of Cu_xTiSe_2," *Physical Review Letters*, vol. 100, no. 10, p. 106402, 2008.

[39] A. G. Cheong, K.-Y. Choi, P. Lemmens, J. J. Yang, and S-W, "Proximity to a commensurate charge modulation in IrTe(2-x)Se_x (x = 0 and 0.45) revealed by Raman spectroscopy," *New Journal of Physics*, vol. 16, no. 9, p. 93061, 2014.

[40] T. G. Spiro, V. A. Maroni, and C. O. Quicksall, "Revised "cluster" Raman frequencies for $Pb_6O(OH)_6$4+," *Inorganic Chemistry*, vol. 8, pp. 2524–2526, nov 1969.

[41] Y. Wu, M. An, R. Xiong, J. Shi, and Q. M. Zhang, "Raman scattering spectra in the normal phase of 2H-$NbSe_2$," *Journal of Physics D: Applied Physics*, vol. 41, no. 17, p. 175408, 2008.

[42] A. J. Rosenberg and T. C. Harman, "Cd_3As_2 - A Noncubic Semiconductor with Unusually High Electron Mobility," *J. Appl. Phys.*, vol. 30, no. 10, pp. 1621–1622, 1959.

[43] P. J. Lin-Chung, "Energy-Band Structures of Cd_3As_2 and Zn_3As_2," *Physical Review*, vol. 188, pp. 1272–1280, dec 1969.

[44] Z. K. Liu, J. Jiang, B. Zhou, Z. J. Wang, Y. Zhang, H. M. Weng, D. Prabhakaran, S.-K. Mo, H. Peng, P. Dudin, T. Kim, M. Hoesch, Z. Fang, X. Dai, Z. X. Shen, D. L. Feng, Z. Hussain, and Y. L. Chen, "A stable three-dimensional topological Dirac semimetal Cd_3As_2.," *Nature materials*, vol. 13, pp. 677–81, jul 2014.

[45] S. Borisenko, Q. Gibson, D. Evtushinsky, V. Zabolotnyy, B. Büchner, and R. J. Cava, "Experimental Realization of a Three-Dimensional Dirac Semimetal," *Physical Review Letters*, vol. 113, p. 027603, jul 2014.

[46] Y. Xia, D. Qian, D. Hsieh, L. Wray, A. Pal, H. Lin, A. Bansil, D. Grauer, Y. S. Hor, R. J. Cava, and M. Z. Hasan, "Observation of a large-gap topological-insulator class with a single Dirac cone on the surface," *Nature Physics*, vol. 5, pp. 398–402, may 2009.

[47] A. Bostwick, T. Ohta, T. Seyller, K. Horn, and E. Rotenberg, "Quasiparticle dynamics in graphene," *Nature Physics*, vol. 3, pp. 36–40, dec 2006.

[48] S. M. Young, S. Zaheer, J. C. Y. Teo, C. L. Kane, E. J. Mele, and A. M. Rappe, "Dirac semimetal in three dimensions.," *Physical review letters*, vol. 108, p. 140405, apr 2012.

[49] X. Wan, A. M. Turner, A. Vishwanath, and S. Y. Savrasov, "Topological semimetal and Fermi-arc surface states in the electronic structure of pyrochlore iridates," *Physical Review B*, vol. 83, p. 205101, may 2011.

[50] O. Ermer and J. D. Dunitz, "Least-squares refinement of centrosymmetric trial structures in non-centrosymmetric space groups.," *Acta Crystallographica Section A*, vol. 26, pp. 163–163, jan 1970.

[51] R. E. Marsh, "Centrosymmetric or noncentrosymmetric?," *Acta Crystallographica Section B Structural Science*, vol. 42, pp. 193–198, apr 1986.

[52] Z. Wang, H. Weng, Q. Wu, X. Dai, and Z. Fang, "Three-dimensional Dirac semimetal and quantum transport in Cd_3As_2," *Physical Review B*, vol. 88, p. 125427, sep 2013.

[53] A. L. Friedman, J. L. Tedesco, P. M. Campbell, J. C. Culbertson, E. Aifer, F. K. Perkins, R. L. Myers-Ward, J. K. Hite, C. R. Eddy, G. G. Jernigan, and D. K. Gaskill, "Quantum linear magnetoresistance in multilayer epitaxial graphene.," *Nano letters*, vol. 10, pp. 3962–5, oct 2010.

[54] H. Tang, D. Liang, R. L. J. Qiu, and X. P. A. Gao, "Two-dimensional transport-induced linear magneto-resistance in topological insulator Bi_2Se_3 nanoribbons.," *ACS nano*, vol. 5, pp. 7510–6, sep 2011.

[55] H. He, B. Li, H. Liu, X. Guo, Z. Wang, M. Xie, and J. Wang, "High-field linear magneto-resistance in topological insulator Bi_2Se_3 thin films," *Applied Physics Letters*, vol. 100, p. 032105, jan 2012.

[56] X. Wang, Y. Du, S. Dou, and C. Zhang, "Room temperature giant and linear magnetoresistance in topological insulator Bi_2Te_3 nanosheets.," *Physical review letters*, vol. 108, p. 266806, jun 2012.

[57] L. P. He, X. C. Hong, J. K. Dong, J. Pan, Z. Zhang, J. Zhang, and S. Y. Li, "Quantum transport evidence for the three-dimensional Dirac semimetal phase in Cd_3As_2.," *Physical review letters*, vol. 113, p. 246402, dec 2014.

[58] D. Neubauer, J. P. Carbotte, A. A. Nateprov, A. Löhle, M. Dressel, and A. V. Pronin, "Interband optical conduc-

tivity of [001]-oriented Dirac semimetal Cd_3As_2," p. 6, jan 2016.

[59] S. Jandl, S. Desgreniers, C. Carlone, and M. J. Aubin, "The Raman Spectrum of Cd_3As_2," *Journal of Raman Spectroscopy*, vol. 15, pp. 137–138, apr 1984.

[60] A. Glamazda, K.-Y. Choi, P. Lemmens, W. S. Choi, H. Jeen, T. L. Meyer, and H. N. Lee, "Structural instability of the CoO_4 tetrahedral chain in $SrCoO_3$-δ thin films," *Journal of Applied Physics*, vol. 118, p. 085313, aug 2015.

[61] B. H. Bairamov, I. P. Ipatova, and V. A. Voitenko, "Raman scattering from current carriers in solids," 1993.

[62] A. Compaan, G. Contreras, M. Cardona, and A. Axmann, "Phonon Spftening in Ultra Heavily Doped Si and Ge," *Le Journal de Physique Colloques*, vol. 44, pp. C5–197–C5–201, oct 1983.

[63] G. Kavlak, J. McNerney, R. L. Jaffe, and J. E. Trancik, "Growth in metals production for rapid photovoltaics deployment," in *2014 IEEE 40th Photovoltaic Specialist Conference, PVSC 2014*, pp. 1442–1447, 2014.

[64] Y. S. Lee, J. Heo, S. C. Siah, J. P. Mailoa, R. E. Brandt, S. B. Kim, R. G. Gordon, and T. Buonassisi, "Ultrathin amorphous zinc-tin-oxide buffer layer for enhancing heterojunction interface quality in metal-oxide solar cells," *Energy & Environmental Science*, vol. 6, p. 2112, jun 2013.

[65] L. C. Olsen, R. C. Bohara, and M. W. Urie, "Explanation for low-efficiency Cu_2O Schottky-barrier solar cells," *Applied Physics Letters*, vol. 34, p. 47, aug 1979.

[66] B. K. Meyer, A. Polity, D. Reppin, M. Becker, P. Hering, P. J. Klar, T. Sander, C. Reindl, J. Benz, M. Eickhoff, C. Heiliger,

M. Heinemann, J. Bläsing, A. Krost, S. Shokovets, C. Müller, and C. Ronning, "Binary copper oxide semiconductors: From materials towards devices," *physica status solidi (b)*, vol. 249, pp. 1487–1509, aug 2012.

[67] K. Akimoto, S. Ishizuka, M. Yanagita, Y. Nawa, G. K. Paul, and T. Sakurai, "Thin film deposition of Cu_2O and application for solar cells," *Solar Energy*, vol. 80, pp. 715–722, jun 2006.

[68] T. Oshima, M. Nohara, T. Hoshina, H. Takeda, and T. Tsurumi, "Characterization of Cu_2O Thin Film Grown by Molecular Beam Epitaxy," *Key Engineering Materials*, vol. 582, pp. 157–160, sep 2013.

[69] V. Drobny and L. Pulfrey, "Properties of reactively-sputtered copper oxide thin films," *Thin Solid Films*, vol. 61, pp. 89–98, jul 1979.

[70] S. Ishizuka, T. Maruyama, and K. Akimoto, "Thin-film deposition of Cu_2O by reactive radio-frequency magnetron sputtering," *Japanese Journal of Applied Physics, Part 2: Letters*, vol. 39, no. 8 A, 2000.

[71] J. Deuermeier, J. Gassmann, J. BroÌĹtz, and A. Klein, "Reactive magnetron sputtering of Cu_2O: Dependence on oxygen pressure and interface formation with indium tin oxide," *Journal of Applied Physics*, vol. 109, p. 113704, jun 2011.

[72] A. Wagner, H. Scherg-Kurmes, A. Waag, and A. Bakin, "Vapour phase epitaxy of Cu_2O on a-plane Al_2O_3," *physica status solidi (c)*, vol. 10, pp. 1284–1287, aug 2013.

[73] S. Jeong and E. S. Aydil, "Heteroepitaxial growth of Cu2O thin film on ZnO by metal organic chemical vapor deposition," *Journal of Crystal Growth*, vol. 311, pp. 4188–4192, aug 2009.

[74] S. Y. Kim, C. H. Ahn, J. H. Lee, Y. H. Kwon, S. Hwang, J. Y. Lee, and H. K. Cho, “p-Channel oxide thin film transistors using solution-processed copper oxide.,” *ACS applied materials & interfaces*, vol. 5, pp. 2417–21, apr 2013.

[75] T. Waechtler, S. Oswald, N. Roth, A. Jakob, H. Lang, R. Ecke, S. E. Schulz, T. Gessner, A. Moskvinova, S. Schulze, and M. Hietschold, “Copper Oxide Films Grown by Atomic Layer Deposition from Bis(tri-n-butylphosphane)copper(I)acetylacetonate on Ta, TaN, Ru, and SiO_2,” *Journal of The Electrochemical Society*, vol. 156, p. H453, jun 2009.

[76] A. T. Marin, D. Muñoz-Rojas, D. C. Iza, T. Gershon, K. P. Musselman, and J. L. MacManus-Driscoll, “Novel Atmospheric Growth Technique to Improve Both Light Absorption and Charge Collection in ZnO/Cu_2O Thin Film Solar Cells,” *Advanced Functional Materials*, vol. 23, pp. 3413–3419, jul 2013.

[77] A. Mukhopadhyay, A. Chakraborty, A. Chatterjee, and S. Lahiri, “Galvanostatic deposition and electrical characterization of cuprous oxide thin films,” *Thin Solid Films*, vol. 209, pp. 92–96, mar 1992.

[78] P. E. de Jongh, D. Vanmaekelbergh, and J. J. Kelly, “Cu_2O: Electrodeposition and Characterization,” *Chemistry of Materials*, vol. 11, pp. 3512–3517, dec 1999.

[79] S. Jeong, A. Mittiga, E. Salza, A. Masci, and S. Passerini, “Electrodeposited ZnO/Cu_2O heterojunction solar cells,” *Electrochimica Acta*, vol. 53, pp. 2226–2231, jan 2008.

[80] K. P. Musselman, A. Marin, A. Wisnet, C. Scheu, J. L. MacManus-Driscoll, and L. Schmidt-Mende, “A Novel Buffering Technique for Aqueous Processing of Zinc Oxide Nanostructures and Interfaces, and Corresponding Im-

provement of Electrodeposited ZnO-Cu_2O Photovoltaics," *Advanced Functional Materials*, vol. 21, pp. 573–582, feb 2011.

[81] A. El-Shaer and A. Abdelwahed, "Potentiostatic Deposition and Characterization of Cuprous Oxide Thin Films," *ISRN Nanotechnology*, vol. 2013, pp. 1–5, 2013.

[82] S. K. Baek, K. R. Lee, and H. K. Cho, "Oxide p-n heterojunction of Cu_2O/ZnO nanowires and their photovoltaic performance," *Journal of Nanomaterials*, vol. 2013, 2013.

[83] L. Wang and M. Tao, "Fabrication and Characterization of p-n Homojunctions in Cuprous Oxide by Electrochemical Deposition," *Electrochemical and Solid-State Letters*, vol. 10, p. H248, sep 2007.

[84] M. Willander, O. Nur, Q. X. Zhao, L. L. Yang, M. Lorenz, B. Q. Cao, J. Zúñiga Pérez, C. Czekalla, G. Zimmermann, M. Grundmann, A. Bakin, A. Behrends, M. Al-Suleiman, A. El-Shaer, A. Che Mofor, B. Postels, A. Waag, N. Boukos, A. Travlos, H. S. Kwack, J. Guinard, and D. Le Si Dang, "Zinc oxide nanorod based photonic devices: recent progress in growth, light emitting diodes and lasers.," *Nanotechnology*, vol. 20, p. 332001, aug 2009.

[85] W. Septina, S. Ikeda, M. A. Khan, T. Hirai, T. Harada, M. Matsumura, and L. M. Peter, "Potentiostatic electrodeposition of cuprous oxide thin films for photovoltaic applications," *Electrochimica Acta*, vol. 56, pp. 4882–4888, may 2011.

[86] Y. S. Jeong, H. Kim, and H. S. Lee, "Growth and characterization of p-Cu_2O/n-ZnO nanorod heterojunctions prepared by a two-step potentiostatic method," *Journal of Alloys and Compounds*, vol. 573, pp. 163–169, oct 2013.

[87] M. Abdelfatah, J. Ledig, A. El-Shaer, A. Wagner, V. Marin-Borras, A. Sharafeev, P. Lemmens, M. M. Mosaad, A. Waag,

and A. Bakin, "Fabrication and characterization of low cost Cu_2O/ZnO:Al solar cells for sustainable photovoltaics with earth abundant materials," *Solar Energy Materials and Solar Cells*, vol. 145, pp. 454–461, feb 2016.

[88] M. Koyano, P. QuocBao, L. thi ThanhBinh, L. HongHa, N. NgocLong, and S. Katayama, "Photoluminescence and Raman Spectra of ZnO Thin Films by Charged Liquid Cluster Beam Technique," *physica status solidi (a)*, vol. 193, pp. 125–131, sep 2002.

[89] H. Solache-Carranco, G. Juarez-Diaz, M. Galvan-Arellano, J. Martinez-Juarez, G. Romero-Paredes, and R. Pena-Sierra, "Raman Scattering and Photoluminescence Studies on Cu_2O," in *5th International Conference on Electrical Engineering, Computing Science and Automatic Control (CCE 2008)*, no. Cce, pp. 421–424, 2008.

[90] Y.-K. Hsu, C.-H. Yu, Y.-C. Chen, and Y.-G. Lin, "Fabrication of coral-like Cu_2O nanoelectrode for solar hydrogen generation," *Journal of Power Sources*, vol. 242, pp. 541–547, nov 2013.

[91] A. Bello, D. Dodoo-Arhin, K. Makgopa, M. Fabiane, and N. Manyala, "Surfactant Assisted Synthesis of Copper Oxide (CuO) Leaf-like Nanostructures for Electrochemical Applications," 2014.

[92] S. Hussain, C. Cao, G. Nabi, W. S. Khan, Z. Usman, and T. Mahmood, "Effect of electrodeposition and annealing of ZnO on optical and photovoltaic properties of the p-Cu_2O/n-ZnO solar cells," *Electrochimica Acta*, vol. 56, pp. 8342–8346, oct 2011.

[93] K. P. Musselman, A. Marin, L. Schmidt-Mende, and J. L. MacManus-Driscoll, "Incompatible Length Scales in Nanos-

tructured Cu_2O Solar Cells," *Advanced Functional Materials*, vol. 22, pp. 2202–2208, may 2012.

[94] K. P. Musselman, A. Wisnet, D. C. Iza, H. C. Hesse, C. Scheu, J. L. MacManus-Driscoll, and L. Schmidt-Mende, "Strong efficiency improvements in ultra-low-cost inorganic nanowire solar cells.," *Advanced materials (Deerfield Beach, Fla.)*, vol. 22, pp. E254–8, sep 2010.

[95] Y. Ievskaya, R. Hoye, A. Sadhanala, K. Musselman, and J. MacManus-Driscoll, "Fabrication of ZnO/Cu_2O heterojunctions in atmospheric conditions: Improved interface quality and solar cell performance," *Solar Energy Materials and Solar Cells*, vol. 135, pp. 43–48, apr 2015.

[96] R. L. Z. Hoye, R. E. Brandt, Y. Ievskaya, S. Heffernan, K. P. Musselman, T. Buonassisi, and J. L. MacManus-Driscoll, "Perspective: Maintaining surface-phase purity is key to efficient open air fabricated cuprous oxide solar cells," *APL Materials*, vol. 3, p. 020901, feb 2015.

[97] Y. Liu, H. K. Turley, J. R. Tumbleston, E. T. Samulski, and R. Lopez, "Minority carrier transport length of electrodeposited Cu_2O in ZnO/Cu_2O heterojunction solar cells.," *Applied Physics Letters*, vol. 98, no. 16, p. 162105, 2011.

[98] S. Hussain, C. Cao, Z. Usman, Z. Chen, G. Nabi, W. S. Khan, Z. Ali, F. K. Butt, and T. Mahmood, "Fabrication and photovoltaic characteristics of Cu_2O/TiO_2 thin film heterojunction solar cell," *Thin Solid Films*, vol. 522, pp. 430–434, nov 2012.

[99] C. H. Lee, D. R. Kim, and X. Zheng, "Transfer printing methods for flexible thin film solar cells: Basic concepts and working principles," *ACS Nano*, vol. 8, no. 9, pp. 8746–8756, 2014.

[100] T. R. Cook, D. K. Dogutan, S. Y. Reece, Y. Surendranath, T. S. Teets, and D. G. Nocera, "Solar energy supply and storage for

the legacy and nonlegacy worlds," *Chemical Reviews*, vol. 110, no. 11, pp. 6474–6502, 2010.

[101] H. Sun, J. Wei, Y. Jia, X. Cui, K. Wang, and D. Wu, "Flexible carbon nanotube/mono-crystalline Si thin-film solar cells.," *Nanoscale research letters*, vol. 9, p. 514, jan 2014.

[102] J. Xie, C. Guo, and C. M. Li, "Ga doping to significantly improve the performance of all-electrochemically fabricated Cu_2O-ZnO nanowire solar cells.," *Physical chemistry chemical physics : PCCP*, vol. 15, pp. 15905–11, oct 2013.

[103] J. Xie, C. Guo, and C. M. Li, "Interface functionalization with polymer self-assembly to boost photovoltage of Cu_2O/ZnO nanowires solar cells," *International Journal of Hydrogen Energy*, vol. 39, pp. 16227–16233, sep 2014.

[104] M. Izaki, T. Shinagawa, K.-T. Mizuno, Y. Ida, M. Inaba, and A. Tasaka, "Electrochemically constructed p-Cu_2O/n-ZnO heterojunction diode for photovoltaic device," *Journal of Physics D: Applied Physics*, vol. 40, pp. 3326–3329, jun 2007.

[105] Y. S. Lee, D. Chua, R. E. Brandt, S. C. Siah, J. V. Li, J. P. Mailoa, S. W. Lee, R. G. Gordon, and T. Buonassisi, "Atomic layer deposited gallium oxide buffer layer enables 1.2 V open-circuit voltage in cuprous oxide solar cells.," *Advanced materials (Deerfield Beach, Fla.)*, vol. 26, pp. 4704–10, jul 2014.

[106] M. Abdelfatah, J. Ledig, A. El-Shaer, A. Wagner, A. Sharafeev, P. Lemmens, M. M. Mosaad, A. Waag, and A. Bakin, "Fabrication and characterization of flexible solar cell from electrodeposited Cu_2O thin film on plastic substrate," *Solar Energy*, vol. 122, pp. 1193–1198, dec 2015.

[107] T. Mahalingam, J. S. P. Chitra, J. P. Chu, H. Moon, H. J. Kwon, and Y. D. Kim, "Photoelectrochemical solar cell studies on

electroplated cuprous oxide thin films," *Journal of Materials Science: Materials in Electronics*, vol. 17, pp. 519–523, jul 2006.

[108] T. Minami, T. Miyata, K. Ihara, Y. Minamino, and S. Tsukada, "Effect of ZnO film deposition methods on the photovoltaic properties of ZnO-Cu_2O heterojunction devices," *Thin Solid Films*, vol. 494, pp. 47–52, jan 2006.

[109] T. Minami, T. Miyata, and Y. Nishi, "Cu_2O-based heterojunction solar cells with an Al-doped ZnO/oxide semiconductor/thermally oxidized Cu_2O sheet structure," *Solar Energy*, vol. 105, pp. 206–217, jul 2014.

Lebenslauf

Persönliche Daten:

Name: Azat Sharafeev
Geburtsdatum: 23.11.1989
Geburtsort: Potsdam
Telefon: +4917676183005
E-mail: a.sharafeev@tu-bs.de

Ausbildung:

10.2013 - 03.2017	*Doktorand* Institut für Physik der Kondensierten Materie, TU Braunschweig (Deutschland).
08.2012 - 08.2013	*Master of Science (Technology)* Fakultät für Technische Physik, Technische Universität Lappeenranta (Finnland).
09.2011 - 07.2012	*Master of Engineering* Fakultät für Elektronik, Sankt Petersburg Staatliche Elektrotechnische Universität (Russland).
09.2007 - 07.2011	*Bachelor of electronics and microelectronics*. Fakultät für Elektronik, Sankt Petersburg Staatliche Elektrotechnische Universität (Russland).

Praktische Erfahrung:

01.2012 - 07.2012	*Hochfrequenz Ingenieur* Forschung und Entwicklung an der Sankt Petersburg Fabrik "Magneton".

Sprachen:

Deutsch	sehr gute Kenntnisse
Englisch	sehr gute Kenntnisse
Russisch	Muttersprache

Sonstiges:

- Mitglied der International Graduate School of Metrology (IGSM) in Braunschweig mit PTB Kollaboration (seit 2013).

- "Physik für Maschninenbau" und "Festkörperphysik" Unterrichtung bei TU Braunschweig. Nominierung für "Beste grundständige Lehre 2015".

- Student Union Koordinator an der Sankt Petersburg Elektrotechnische Universität (2007-2012).